

This is to certify that the

dissertation entitled

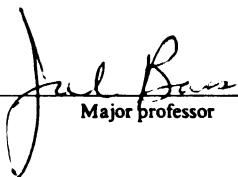
*Characterization and Electron Energy Loss  
Spectroscopy on NiV and NiMo Superlattices*

presented by

*Sami Husein Mahmood*

has been accepted towards fulfillment  
of the requirements for

Ph.D. degree in Physics

  
Major professor

Date September 9, 1986



**RETURNING MATERIALS:**  
Place in book drop to  
remove this checkout from  
your record. FINES will  
be charged if book is  
returned after the date  
stamped below.

--	--	--

CHARACTERIZATION AND ELECTRON ENERGY LOSS SPECTROSCOPY ON  
NiV AND NiMo SUPERLATTICES

By

Sami Husein Mahmood

A DISSERTATION

Submitted to  
Michigan State University  
in partial fulfillment of the requirements  
for the degree of

DOCTOR OF PHILOSOPHY

Department of Physics and Astronomy

1986

30  
st  
(E  
El  
sy  
tr  
tr  
in  
reg  
to  
Lab  
cha  
obs  
Niv  
exc  
att  
sam  
the  
A i  
not  
pres

## ABSTRACT

### CHARACTERIZATION AND ELECTRON ENERGY LOSS SPECTROSCOPY ON NiV AND NiMo SUPERLATTICES

By

Sami Husein Mahmood

NiV superlattices with periods ( $\Lambda$ ) ranging from 15 to 80Å, and NiMo superlattices with  $\Lambda$  from 14 to 110Å were studied using X-Ray Diffraction (XRD), Electron Diffraction (ED), Energy-Dispersive X-Ray (EDX) microanalysis, and Electron Energy Loss Spectroscopy (EELS). Both of these systems have sharp superlattice-to-"amorphous" (S-A) transitions at about  $\Lambda=17\text{Å}$ . Superlattices with  $\Lambda$  around the S-A boundary were found to have large local variations in the in-plane grain sizes. Except for a few isolated regions, the chemical composition of the samples were found to be uniform. In samples prepared at Argonne National Laboratory (ANL), most places studied with EELS showed changes in the EELS spectrum with decreasing  $\Lambda$ . An observed growth in a plasmon peak at  $\sim 10\text{eV}$  in both NiV and NiMo as  $\Lambda$  decreased down to 19Å is attributed to excitation of interface plasmons. Consistent with this attribution, the peak height shrank in the "amorphous" samples. The width of this peak is consistent with the theory. The shift in this peak down to 9eV with decreasing  $\Lambda$  in NiMo is not understood. Three other effects are also not well understood, but appear to be related to the presence of sharp interfaces in the samples: (a) the

Sami Husein Mahmood

dominant peak at  $\sim 24\text{eV}$  remained fixed in energy, independent of  $\Lambda$ , for NiMo superlattices, but shifted upward from  $21\text{eV}$  to  $24\text{eV}$  in NiV; charge transfer was ruled out as a possible explanation for this shift; (b) the sharp V  $2p \rightarrow 3d$  "white lines" grew in intensity with decreasing  $\Lambda$  down to  $19\text{\AA}$ , and then shrank again in the "amorphous" samples; (c) the Ni "white lines" remained constant in intensity independent of  $\Lambda$ . Samples prepared at Michigan State University (MSU) did not show similar changes in EELS spectra with  $\Lambda$ . Their difference in behavior is attributed to their different growth conditions, which apparently produced much less perfect interfaces than for the ANL samples.

To my wife, Lisa, and to my family.

## ACKNOWLEDGMENTS

I would like to thank my advisor, Professor Jack Bass, for his continuous guidance and support. I am thankful to Professors G. Bertsch, C. Foiles, S.D. Mahanti, and S. Solin for many helpful discussions, comments, and suggestions. The technical assistance of V. Shull in maintaining the FE-STEM was invaluable. Thanks are also due to Dr. I.K. Schuller and J. Slaughter for providing us with the samples. I am indebted to many of my colleagues, especially X.W. Qian for his help in x-ray studies and computer-related problems, and N. Kedarnath for continuously being a helpful friend. I wish to acknowledge the financial support of the National Science Foundation in this work. Finally, I would like to express my gratitude to Yarmouk University for providing me with a full scholarship which helped me complete my studies and made this work possible.

## TABLE OF CONTENTS

	<u>Page</u>
LIST OF TABLES.....	viii
LIST OF FIGURES.....	ix
CHAPTER ONE INTRODUCTION.....	1
1.1 Previous Work.....	2
1.1.1 Previous Work on Struc- tural Properties of NiV and NiMo Superlattices.....	3
1.1.2 Previous Work on Optical Studies and EELS.....	5
1.1.2.A Plasmon Structure in Simple Metals.....	5
1.1.2.B Plasmon and Core Excitations in Transition Metals.....	7
1.2 The Present Thesis.....	10
1.2.1 Characterization of the Samples.....	10
1.2.2 Electron Energy Loss Spectroscopy (EELS).....	12
CHAPTER TWO THEORY.....	14
2.1 Collective Excitations of a Metal Foil.....	14
2.2 Interface Plasmons at Bi- metallic Junctions.....	19
2.3 Collective Excitations in Metallic Superlattices.....	25
2.3.1 Collective and Surface Excitations in the Local Limit..	25
2.3.1.A Collective Excitations..	25
2.3.1.B Surface Excitations.....	29
2.3.2 Collective Excitations in the Non-local Limit.....	32
CHAPTER THREE SAMPLE PREPARATION AND CHARACTERIZATION...	35
3.1 Sample Preparation.....	35

3.2	Structural Properties of Super-	
	lattices.....	37
3.2.1	$\theta/2\theta$ X-Ray Diffraction	
	(XRD).....	37
3.2.1.A	One-Dimensional	
	Diffraction Theory	
	of Superlattices.....	37
3.2.1.B	Experimental Results	
	and Analysis.....	42
3.2.2	Electron Diffraction (ED).....	50
3.2.2.A	The Electron Diffrac-	
	tion Camera and	
	Bragg Reflection.....	51
3.2.2.B	Selected Area Diffrac-	
	tion (SAD) and Micro-	
	diffraction (MD).....	53
3.3	Energy-Dispersive X-Ray (EDX)	
	Microanalysis.....	66
3.3.1	Theoretical Background.....	69
CHAPTER FOUR	EXPERIMENTAL RESULTS AND ANALYSIS.....	80
4.1	Introduction.....	80
4.2	EELS of Pure Metals and Oxides.....	81
4.3	EELS of NiV Superlattices.....	92
4.3.1	The Energy Range <100ev.....	92
4.3.2	The Energy Range >500ev.....	106
4.3.2.A	V Core Edge at 513ev...110	
4.3.2.B	Ni Core Edge at ~850ev.117	
4.4	EELS of NiMo Superlattices in	
	the Energy Range <100ev.....	120
CHAPTER FIVE	SUMMARY AND CONCLUSION.....	128
APPENDIX A	The FE-STEM.....	133
LIST OF REFERENCES.....		145

Table

3.1

3.2

3.3

4.1

LIST OF TABLES

<u>Table</u>	<u>Page</u>
3.1 Fitting Parameters for Structure Factor Calculations of the Superlattices.....	42
3.2 The d-Spacing and the Miller Indices of the Ni Planes Responsible for the Observed Reflections.....	55
3.3 The Experimental d-Spacings of the NiV Superlattice with $\Lambda=19\text{\AA}$ , Along with the Indices and Calculated d-Spacings of NiV Lattice Planes that are Within 2% of the Observed Ones.....	59
4.1 NiV Samples Prepared at ANL.....	93

## LIST OF FIGURES

<u>Figure</u>	<u>Page</u>
2.1	Cross-Sectional View of the Field Lines of the (a) Symmetric and (b) Anti-symmetric Surface Plasmon Modes in a Metallic Film.....17
2.2	Dispersion of the Symmetric ( $w_+$ ) and Anti- symmetric ( $w_-$ ) Surface Plasmons.....18
2.3	Dispersion of the Interface Plasmon at a Bi-Mg Junction.....23
2.4	Schematic Diagram of an Infinite Superlattice.....26
2.5	Dispersion of Interface and Surface Plas- mons in a NiV Superlattice.....30
2.6	Dispersion Relation of Bulk Plasmons in Metallic Superlattices.....33
3.1	XRD Spectra and Structure Factor of ANL NiMo Superlattices.....43
3.2	XRD Spectra and Structure Factor of ANL NiV Superlattices.....44
3.3	XRD Spectra in Two Different Pieces of the ANL 19Å NiMo Superlattice.....46
3.4	The Behavior of the Average d-spacing in NiMo Superlattices.....47
3.5	The Behavior of the Average d-spacing in NiV Superlattices.....48
3.6	SAD of (a) Crystalline Ni, and (b) Amorphous FeZr Films.....54
3.7	MD of a Crystalline Ni Film.....56
3.8	SAD of ANL 19Å NiV Superlattice.....58
3.9	SAD in Three Different Regions of ANL 19Å NiV Superlattice.....61



3.10	SAD in Three Different Regions of ANL 60Å NiV Superlattice.....	62
3.11	SAD in Three different Regions of MSU 27Å NiV Superlattice.....	64
3.12	SAD and MD in Two Different Regions of MSU 15Å NiV Sample.....	65
3.13	EDX Spectrum in a Region of MSU 15Å NiV Sample.....	68
3.14	Ni-to-V Thickness Ratio in ANL 19Å NiV Superlattice.....	73
3.15	Topology of a Measured Piece (B9) of ANL 19Å NiV Superlattice.....	74
3.16	Ni-to-V Thickness Ratio in MSU 27Å NiV Superlattice.....	76
3.17	Mo-to-Ni Thickness Ratio in MSU 22Å NiMo Superlattice.....	78
4.1	Dielectric Function, Loss Function, and EELS of Al.....	82
4.2	Dielectric Function, Loss Function, and EELS of Mo.....	85
4.3	Loss Function and EELS of V.....	87
4.4	Contaminated and Uncontaminated V EELS Spectra....	90
4.5	Loss Function and EELS of Ni.....	91
4.6	EELS of ANL 19Å NiV Superlattice and NiV pseudo-alloy.....	95
4.7	EELS of ANL NiV Samples.....	97
4.8	BF Image of a Nonuniform Region of MSU 27Å NiV Superlattice.....	103
4.9	EELS of MSU NiV Samples.....	105
4.10	Schematic Diagram of L <sub>2,3</sub> Core Excitations in a Transition Metal.....	109
4.11	L <sub>2,3</sub> Excitations of V.....	113
4.12	Intensities of the V WLS in NiV Samples.....	114

4.13	L <sub>2,3</sub> Excitations of Ni.....	119
4.14	EELS of ANL NiMo Samples.....	121
A.1	The Principle of the FE-STEM.....	134
A.2	Schematic Diagram of the Electron Optical Column in the FE-STEM.....	135

su

Ev

pr

Ep

se

use

mea

sup

ing

x-r

inte

empn

Ru g

e las

ties

our

Spec

Opti

absor

radia

## CHAPTER ONE

### INTRODUCTION

The production and perfection of artificial metallic superlattices has recently been of great interest. Evaporation [1] and sputtering [2] have been used to prepare metallic superlattices. Although Molecular Beam Epitaxy (MBE) was previously used primarily to prepare semiconductor superlattices [3], it has also recently been used to prepare single crystal metallic superlattices [4].

The interest in metallic superlattices stems in large measure from the fact that it is possible to produce superlattices with novel magnetic [4,5,6] and superconducting [7] properties. The possibility of applying them as x-ray [8,9] and neutron [10] mirrors is another potentially interesting application of these structures.

Recent experimental work on metallic multilayers, with emphasis on superconducting systems, was reviewed by S. Ruggiero [11]. Several physical properties, such as elastic, magnetic, superconducting, and transport properties were reviewed by I.K. Schuller and C. Falco [2]. To our knowledge, there are no published Electron Energy Loss Spectroscopy (EELS) studies of metallic superlattices. Optical studies [12], x-ray photoemission (XPS), x-ray absorption (XAS) [13,14], EELS [15,16], and synchrotron radiation [17] were employed to obtain information about

the electronic structure of pure metals and alloys.

The Vacuum Generators (VG) model HB-501 Field Emission Scanning Transmission Electron Microscope (FE-STEM)<sup>†</sup> permits the measurement of energy losses from 0 to 2Kev in a single spectrum, with resolution <1ev. An electron beam energy up to 100Kev can be used, making it possible to measure transition metal samples that are ~400Å-thick without the need to correct for multiple scattering. The beam size can be as small as 5Å, permitting measurements of small particles. Energy Dispersive X-Ray (EDX) analysis and electron diffraction facilities allow the characterization of the small regions under investigation [18]. A cold stage is available to minimize the migration of surface contamination to the region under investigation.

In this thesis, we will present local EELS measurements on NiV and NiMo superlattices in the energy range <100ev and >500ev. We also present  $\theta/2\theta$  x-ray diffraction (XRD), electron diffraction (ED), and energy-dispersive x-ray (EDX) measurements.

### 1.1 Previous Work

In this section we discuss previous work in the experimental areas related to the subject of this thesis. Structural analysis for NiV and NiMo superlattices is

---

<sup>†</sup>A more detailed description of the FE-STEM system is given in Appendix A.

summ

revis

prev

work

tices

avail

tory

grou

coner

inter

have

diffe

the s

discu

elast

prepa

X-ray

these

BCC M

respec

F

the (1

summarized. Optical and energy loss measurements are reviewed for some pure metals and alloys. We also review previous work on interface plasmons.

We focus on NiV and NiMo superlattices in the present work for three reasons: First, samples of both superlattices with a wide range of periods ( $\Lambda$ ) were kindly made available by Dr. I.K. Schuller of Argonne National Laboratory (ANL); second, they were characterized by Schuller's group using x-rays and found to have both long range coherence perpendicular to the layers and fairly sharp interfaces; third, the fact that these two superlattices have a common element, Ni, allowed us to test the effect of different electronegativities of the second constituent of the superlattice (Mo or V) on the EELS data, as will be discussed in conjunction with the experimental results.

#### 1.1.1 Previous Work on Structural Properties of NiV and NiMo Superlattices

In 1982, Khan et al. [19] studied the structural, elastic, and transport properties of NiMo superlattices prepared by sputtering on Mica and Sapphire substrates. X-ray diffraction (XRD) in reflection geometry showed that these superlattices are composed of layers of FCC Ni and BCC Mo, oriented along the [111] and [110] directions, respectively.

For  $\Lambda > 200\text{\AA}$ , two lines were observed, corresponding to the (110) plane of Mo ( $d_{\text{Mo}} = 2.22\text{\AA}$ ) and the (111) plane of Ni

(dy:  
obse  
supe  
x-ra  
stru  
the  
was

to t  
indi  
dieu  
cent  
back  
lar  
expa  
str  
uni  
the  
ano  
bas  
exp  
tiv

som  
Geo  
Pol

( $d_{Ni} = 2.03 \text{ \AA}$ ). For  $\Lambda < 16.6 \text{ \AA}$ , only one broad peak was observed, reminiscent of an amorphous structure. For superlattice periods in the range  $130 \text{ \AA} \geq \Lambda \geq 16.6 \text{ \AA}$ , sharp x-ray peaks were observed with satellites consistent with a structure having well-defined layers. From the widths of the x-ray lines, the coherence perpendicular to the layers was estimated to be  $\sim 100 \text{ \AA}$ .

As the superlattice period was varied from  $> 100 \text{ \AA}$  down to  $16.6 \text{ \AA}$ , changes in the positions of the central lines indicated a 2% expansion in the average d-spacing perpendicular to the layers. For samples with  $\Lambda < 16.6 \text{ \AA}$ , the center of the broad "amorphous" peak showed a contraction back to the average d-spacing corresponding to samples with large  $\Lambda$ . In an attempt to find the source of this expansion, two simple models were used to calculate the structure factor of the lattice. In the first model, a uniform expansion throughout the lattice was assumed. In the second, the expansion was assumed to be due to a single anomalous spacing at the interface. The intensity analysis based on both models was found to be consistent with the experimental intensities; hence, XRD spectra were insensitive to the nature of expansion assumed in the models.

Khan et al. also analyzed the in-plane structure of some equilayer thickness samples using XRD in transmission geometry. They found that the samples were laterally polycrystalline. Moreover, they found a slight (0.6%)

expansion in the Ni d-spacing, and a (0.5%) contraction in the Mo d-spacing parallel to the layers. They also performed reflection XRD in the small angle scattering region and observed only odd order diffraction peaks, from which they concluded that the composition modulation was close to a square wave (i.e., equal layer thickness of the two constituents with sharp interfaces).

In 1985, Homma et al. [20] studied the structural properties of NiV superlattices, using x-ray and neutron diffraction. The high-angle reflection peaks (around the central peak) exhibited structural characteristics similar to those of the NiMo system. From rocking curve measurements around the first order (small angle) Bragg reflection peak, they deduced a columnar structure for the growth of the samples, with a coherence length  $\sim 740\text{\AA}$  perpendicular to the layers, and  $50\text{\AA}$  in the plane. The in-plane grain size of  $50\text{\AA}$  estimated from transmission  $\theta/2\theta$  scans near the V (110) peak was consistent with the size estimated from the rocking curve measurements.

### 1.1.2 Previous Work on Optical Studies and EELS

#### 1.1.2.A Plasmon Structure in Simple Metals

Since the work of Pines and Bohm [21,22] in the early 1950s, electron energy losses experienced by fast electrons passing through material foils have received great interest, both from the theoretical [23-25] and experimental



[26] points of view. The interpretation by Pines and Bohm [22] that some of the energy losses are due to plasma oscillations or "plasmons" was strengthened by the observation of plasmon excitations in simple metals such as Al [26], Na and K [27] and in semiconductors and semimetals [28]. The plasmon energies of the above mentioned materials were found to be in excellent agreement with the classical free electron plasma energy [29]:

$$\omega_p = \left( \frac{4\pi n e^2}{m} \right)^{1/2} \quad (1.1)$$

where  $n$  is the density of the free electrons,  $e$  is the electronic charge, and  $m$  is the electronic mass.

Stern and Ferrell [30] predicted the existence of an interface plasmon localized at the interface between two materials A and B.

This plasmon energy is given by:

$$\omega_I = \left( \frac{\omega_A^2 + \omega_B^2}{2} \right)^{1/2} \quad (1.2)$$

where  $\omega_A$  and  $\omega_B$  are the energies of the plasmons of the two materials.

This interface plasmon mode was first observed in Bi-Mg bilayer films by Miller and Axelrod in 1965 [31]. They failed, however, to observe such a plasmon mode in Al-Mg bilayer films, which they attributed to blurring of the interface between Al and Mg. Their calculations showed a negligible diffusion between Bi and Mg, and a  $24\text{\AA}$  diffusion length between Al and Mg during the measuring

[26]

[22]

oscil

tion

[26]

[28]

mate

clas

when

elect

inter

mater

This

where

mater

Bi-Mg

They

Al-Mg

the in

a neg

diffus

[26] points of view. The interpretation by Pines and Bohm [22] that some of the energy losses are due to plasma oscillations or "plasmons" was strengthened by the observation of plasmon excitations in simple metals such as Al [26], Na and K [27] and in semiconductors and semimetals [28]. The plasmon energies of the above mentioned materials were found to be in excellent agreement with the classical free electron plasma energy [29]:

$$\omega_p = \left( \frac{4\pi n e^2}{m} \right)^{1/2} \quad (1.1)$$

where  $n$  is the density of the free electrons,  $e$  is the electronic charge, and  $m$  is the electronic mass.

Stern and Ferrell [30] predicted the existence of an interface plasmon localized at the interface between two materials A and B.

This plasmon energy is given by:

$$\omega_I = \left( \frac{\omega_A^2 + \omega_B^2}{2} \right)^{1/2} \quad (1.2)$$

where  $\omega_A$  and  $\omega_B$  are the energies of the plasmons of the two materials.

This interface plasmon mode was first observed in Bi-Mg bilayer films by Miller and Axelrod in 1965 [31]. They failed, however, to observe such a plasmon mode in Al-Mg bilayer films, which they attributed to blurring of the interface between Al and Mg. Their calculations showed a negligible diffusion between Bi and Mg, and a  $24\text{\AA}$  diffusion length between Al and Mg during the measuring

tim

the

obs

Al-

plas

cha

plas

supe

than

comp

no s

inte

meta

shed

Opti

used

spect

serie

Thus,

menta

meta

time of 50 seconds. These calculations seem to support their interpretation. Interface plasmons were later observed in several other systems, such as Ag-Mg [32], Al-Cd and Al-CdS [33], and Al-Ag [34].

The properties [35] and the dispersion [36] of these plasmons have been studied theoretically. In the theory chapter, we discuss in greater detail the interface plasmons at metallic bilayer junctions, as well as in superlattices.

#### 1.1.2.B Plasmon and Core Excitations in Transition Metals

Transition metal energy loss spectra are more complex than the previously discussed simple metals, due to the complexity of their electronic structures. Since there was no single theory until the late 1970s that described and interpreted the various peaks that occur in transition metal spectra, experimental work was the only source to shed light upon the dielectric properties of these metals. Optical [37,38] as well as EELS [39,40] techniques were used extensively to study these metals.

In the beginning of the transition metal series, the spectra are relatively simpler than those at the end of the series, where the number of peaks in the spectra increases. Thus, while there is agreement between the various experimental groups on the assignment of peaks in the EELS of metals in the beginning of the transition metal series,

such

assi

meta

assign

coll

second

two

assign

elect

Most

20ev

inter

optic

optical

the d

than

assign

not ju

A

Ksendz

loss s

two pr

volume

T

such as Ti, V, and Mo, there is some disagreement on the assignment of some peaks in the more complex spectra of metals as Fe, Ni, and Cu.

The peaks in the V spectra at  $\sim 11$  and 22ev were assigned to volume plasmons [41-43], the first due to the collective excitation of the 4s electrons [44], and the second due to the excitation of all (4s+3d) electrons. The two peaks in Mo spectra at  $\sim 10.5$  and 24.5ev were also assigned to volume plasmons [37,40,45], the first due to 5s electrons and the second due to (5s+4d) electrons.

The Ni spectrum is more complex, with several peaks. Most investigators [38,41,46] assigned the peaks at  $\sim 8$  and  $\sim 20$ ev to volume plasmons. The  $\sim 27$ ev peak was assigned to interband transitions [41]. Others [46] calculated the optical constants from their EELS and found that the optical absorption coefficient  $\mu$ , and the imaginary part of the dielectric constant,  $\epsilon_2$ , are weaker for the 27ev peak than for the 20ev peak, from which they concluded that the assignment of the 27ev peak to an interband transition is not justified.

As will be discussed in conjunction with the data, Ksendzov [47] suggested a model for interpreting the energy loss spectra in which all three peaks in Ni, as well as the two previously discussed peaks in V and Mo, are due to volume plasmons.

The peaks in the energy range 35-70ev were assigned to

s

a

s

e

t

d

p

s

i

r

w

e

t

i

d

w

t

o

t

(

o

a

single particle transitions from the 3p shell ( $M_{2,3}$ ) in Ni and V, and to transitions from the 4p shell ( $N_{2,3}$ ) in Mo spectra. These assignments are consistent with atomic energy level calculations [48].

Excitations of core-level electrons, as in the  $2p \rightarrow 3d$  transitions, provide information about the unoccupied density of states (DOS) in the conduction bands of solids, particularly the d-bands [49].

More than a decade ago, a superposition model [50] was suggested to describe the DOS of binary alloys. This model is based on charge transfer between the two constituents. The model was found to describe the experimental DOS in Ni-Rh alloys [51]. Good agreement between the theory and experiment was obtained by assuming charge transfer from Ni to Rh. On the other hand, XAS studies of Ni-Cu alloys indicated no change in the number of Ni d-holes despite the decline in the saturation magnetic moment of the samples with increasing Cu concentration [52].

Recently, high-resolution EELS data involving the 2p to 3d transitions were reported [53]. Strong deviations from the single-particle transition probability calculations were found. Such discrepancies include [54]:

- 1) The deviation of the intensity ratio of the  $P_{3/2}$  ( $L_3$ ) and  $P_{1/2}$  ( $L_2$ ) transitions from the statistical ratio of 2:1 [55]. This deviation was also found by Leapman et al. [49].

fo

su

it

(in

fro

met

pie

the

iate

ment

d-bar

excha

the t

elect

inter

1.2

sample

prepar

import

sample)

2) The deviation of the line shape from that expected for the DOS above the Fermi level, in that the intensity is suppressed near the threshold and enhanced further above it.

3) The deviation of the apparent spin-orbit splitting (inferred from the separation of the  $L_2$  and  $L_3$  peak maxima) from that observed in 2p core-line photoemission.

A theory for XAS of the beginning of the transition metal series (below Cr) was presented [54]. First principles band structure and atomic data were used as input for the theory, and the spectra for Ca, Ti, and V were calculated and found to be in good agreement with the experimental data. This theory is applicable to metals with d-band widths much larger than the d-d electron Coulomb and exchange interactions. For the three metals considered, the typical band width ( $\sim 6\text{eV}$ ) is much larger than the d-d electron interactions ( $\sim 1\text{eV}$ ) [54]; hence, the d-d electron interactions can be ignored.

## 1.2 The Present Thesis

### 1.2.1 Characterization of the Samples

This project started when we received a few NiV samples from I.K. Schuller of ANL. Since the samples were prepared several months before we received them, it was important to check the structural characteristics of these samples. Three different techniques were used:

1) XRD: As mentioned in Section 1.1.1, Khan et al. studied the structural properties of NiMo superlattices, and found a 2% expansion in the average d-spacing perpendicular to the layers as  $\Lambda$  decreased down to  $\sim 17\text{\AA}$ , and a contraction back to approximately the bulk value as  $\Lambda$  decreased down to  $\sim 15\text{\AA}$ . We studied the structural characteristics of NiMo and NiV samples to investigate any structural changes of the samples with time.

2) EDX microanalysis: Since XRD studies do not provide information about the local composition of the samples, EDX microanalysis was carried out to check the uniformity in the composition of the samples. The EDX analysis is important to separate effects of contamination, or changes in the relative concentrations of the two constituents, from possible superlattice or interfacial effects.

3) Electron Diffraction: Selected Area Diffraction (SAD) and microdiffraction (MD) studies of the samples using a 100-Kev electron beam provide information about the in-plane structure of the samples. We studied the electron diffraction patterns of the superlattices and the pure metals; we estimated the crystallite sizes (i.e., the in-plane coherence) from the widths of the diffraction peaks, and we made qualitative conclusions about the in-plane structure.

### 1.2.2 Electron Energy Loss Spectroscopy (EELS)

In this thesis, we focus on three major effects:

1) The interfaces: As discussed above, energy loss spectra of bimetallic junctions show new resonances attributable to interface plasmons. NiV and NiMo superlattices with a range of periods that cross the superlattice-"amorphous" border provide a useful system for studying interface plasmons. The usefulness of these systems stems from two reasons:

a) the availability of superlattices with different periods provides samples with different numbers of interfaces per unit volume; thus, we would expect to observe interface resonances with intensities that scale with the number of interfaces per unit volume (i.e., with  $\Lambda$ ).

b) The availability of samples that cross the crystalline (layered)-"amorphous" (nonlayered) border provide an internal check for the interpretation of these resonances being due to interfaces, since, as we go from layered to nonlayered structures across the border, we would expect a sudden drop in the intensity of resonances attributed to interfaces.

2) The effect of layering: The additional periodicity in the z direction (perpendicular to the layers) introduces bands of collective excitations of the superlattice due to coupling of the interface plasmons, as will be discussed in Chapter 2. If splitting of the plasmon bands is larger

than the instrumental resolution, it should be possible to see several interface excitations in the EELS spectra. The effect of layer thickness on these bands can also be investigated.

3) Charge transfer: When two metallic slabs are brought into contact, charge is transferred from the metal with the lower to that with the higher Pauling electronegativity [56]. Since charge transfer occurs in the vicinity of the interface between the two metals ( $\sim 10\text{\AA}$ ) [57] we would expect to see a large effect in superlattices with small periods. Thus, the positions of the plasmon peaks in EELS spectra possibly reveals information about the charge transfer between the two metals. In addition, charge transfer from one metal to another in a superlattice consisting of two transition metals (e.g., from V to Ni in NiV superlattices) leaves more d-holes in one (the V) and fewer holes in the other (Ni). Thus, EELS in the  $L_{2,3}$  energy range ( $>500\text{eV}$ ) provide information about charge transfer between the two metals. To check for charge transfer, we measured: (a) Two systems in the energy range  $<100\text{eV}$ ; NiV, in which the two constituents have different Pauling electronegativities (1.8 for Ni and 1.6 for V), and NiMo where the two constituents have essentially equal electronegativities; (b) The V and Ni  $L_{2,3}$  WLs.

## CHAPTER TWO

### THEORY

In this chapter, we first review the theory of bulk and surface plasmons in a metal foil. Second, we review the theory of interface plasmons at bimetallic junctions. Third, we review the theory of bulk and interface plasmon bands in metallic superlattices, and we discuss the effect of terminating the superlattice, and calculate the surface plasmon dispersion relation. We also apply the appropriate dispersion relations to NiV and NiMo superlattices and calculate the plasmon bands and the surface plasmons.

#### 2.1 Collective Excitations of a Metal Foil [15,58,59]

The dielectric function [15] of a free electron gas, assumed real for simplicity, is given by:

$$\epsilon(\omega, \vec{k}) = 1 - \frac{\omega_p^2}{\omega^2} \frac{1}{1 - \frac{3}{5} (\vec{k} \cdot \vec{v}_F / \omega)^2} \quad (2.1.a)$$

The bulk plasmon frequency is determined by the condition  $\epsilon=0$ . Hence, the dispersion relation of bulk plasmons in simple metals is given by:

$$\omega_b^2 = \omega_p^2 + B^2 k^2 \quad (2.2.a)$$

where in a free electron gas:

$$B^2 = \frac{3}{5} v_F^2 \quad (2.2.b)$$

Here  $\omega_p$  is the bulk plasmon frequency given by equation 1.1

an

is

2.

whi

men

igno

elec

pote

Lapl.

and t

where

two s

para

excit

then

where

for co

elemen

and  $\vec{v}_F$  is the Fermi velocity. In a simple local theory,  $B$  is set equal to zero. The dielectric constant in equation 2.1.a then becomes:

$$\epsilon(\omega) = 1 - \frac{\omega_p^2}{\omega^2} \quad (2.1.b)$$

which will be assumed for all metals, unless otherwise mentioned.

In the long wavelength limit (retardation effects are ignored), the collective excitations produce a macroscopic electric field which can be derived from an electrostatic potential  $f(\vec{x}, t)$ . The electrostatic potential satisfies Laplace's equation everywhere outside the metal:

$$\nabla^2 f(\vec{x}, t) = 0 \quad (2.3.a)$$

and the following relation inside the film:

$$\epsilon(\omega) \nabla^2 f(\vec{x}, t) = 0 \quad (2.3.b)$$

where only one Fourier component of  $f(\vec{x}, t)$  is considered.

Because of translational invariance parallel to the two surfaces of the film, the two-dimensional wave vector  $\vec{k}$  parallel to the surfaces is a good quantum number of the excitations. The electrostatic potential everywhere can then be written as:

$$f(\vec{x}, t) = f(z) \exp(ikx - i\omega t) \quad (2.4)$$

where the wave vector  $\vec{k}$  is assumed parallel to the x-axis for convenience.

For a metal film with thickness  $d$ , two types of elementary excitations which generate a macroscopic field

e

me

su

[3

br

sup

fre

This

conc

equ

orig

loca

surfa

antis

dispe

from

This

exist. One type consists of the symmetric and antisymmetric superposition of the surface plasmons at the two surfaces, as illustrated in Figure 2.1 (from reference [30]). The second consists of bulk plasmons. Now we briefly discuss each type of excitation.

(i) Surface plasmons: A metal-vacuum interface supports a surface plasmon with a wave vector independent frequency  $\omega_s$  given by:

$$\epsilon(\omega_s) = -1 \quad (2.5)$$

This relation can be readily obtained from the boundary conditions at the metal-vacuum interface ( $z=0$ ). Combining equations 2.1.b and 2.5, we obtain  $\omega_s = \omega_p/2^{1/2}$ , as originally derived by Ritchie [59]. These excitations are localized at the surface, and take the form:

$$f(z) \sim e^{-kz} \quad (2.6)$$

For a metal film with a finite thickness  $d$ , the two surface modes couple to produce the symmetric ( $\omega_+$ ) and antisymmetric ( $\omega_-$ ) modes illustrated in Figure 2.1. The dispersion relation for these modes satisfies the relations

$$\epsilon(\omega_-) = -\coth\left(\frac{kd}{2}\right) \quad (2.7.a)$$

$$\epsilon(\omega_+) = -\tanh\left(\frac{kd}{2}\right) \quad (2.7.b)$$

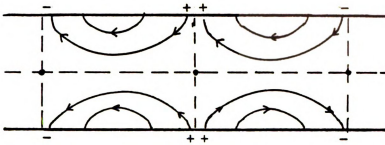
from which we obtain:

$$\omega_{\pm} = \omega_p \left( \frac{1 \pm e^{-kd}}{2} \right)^{1/2} \quad (2.8)$$

This dispersion relation is plotted in Figure 2.2. The two

Figure  
(a) S  
in a v

a) Symmetric mode.



b) Antisymmetric mode.

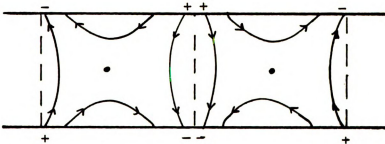


Figure 2.1 Cross-Sectional View of the Field Lines of the (a) Symmetric and (b) Anti-symmetric Surface Plasmon Modes in a Metallic Film

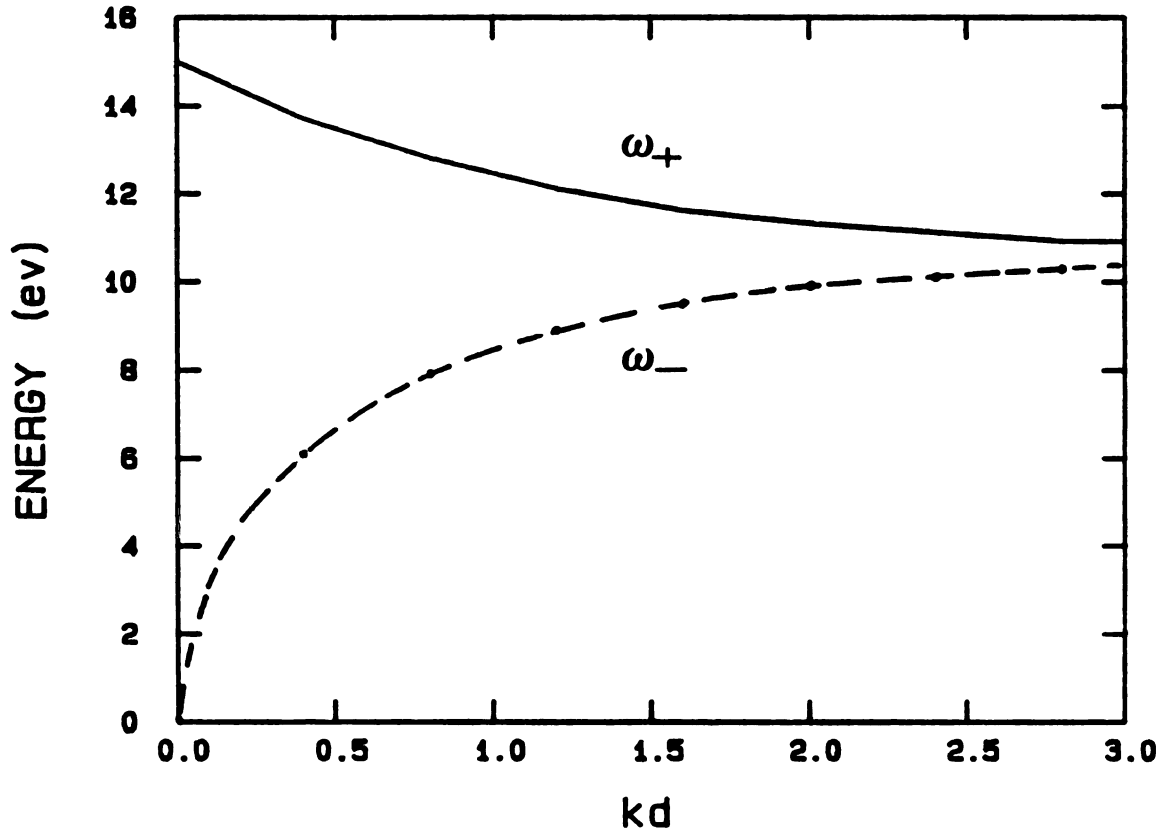


Figure 2.2 Dispersion of the Symmetric ( $\omega_+$ ) and Anti-symmetric ( $\omega_-$ ) Surface Plasmons

branches approach  $\omega_s$  for large  $kd$ , since in this limit the plasmon wavelengths are sufficiently small that the two surface modes decouple [30].

(ii) Bulk plasmons: A metal film also supports bulk plasmons of longitudinal character with frequencies for which  $\epsilon(\omega)=0$ . In such a case, Laplace's equation does not hold in the film. The boundary conditions require that the electrostatic potential vanishes identically outside the film, so that the excitations do not produce a macroscopic field outside the film. Thus, the electrostatic potential inside the film has the form:

$$f(z) \sim \sin\left(\frac{n\pi z}{d}\right) \quad (2.9)$$

and one has standing wave resonances inside the film, the frequencies of which are identical to those for an infinite dielectric.

## 2.2 Interface Plasmons at Bimetallic Junctions [30,60,35,36]

Using an argument similar to that followed in the preceding section, Stern and Ferrell [30] predicted the existence of interface plasmons localized at a metal-metal or metal-dielectric interface. The eigenfrequencies of such modes are given by the relation:

$$\epsilon_1(\omega) + \epsilon_2(\omega) = 0 \quad (2.10)$$

This equation is the generalized form of equation 2.5, and gives the constant interface frequency:

when

and

bul.

calc

foli

refe

when

elect

defin

give

vecto

defin

In th

relat

where

$$w_{1-2}^2 = \frac{w_1^2 + w_2^2}{2} \quad (2.11)$$

where  $w_1$  and  $w_2$  are the bulk plasmon frequencies of metal 1 and 2, respectively.

The hydrodynamic model, including dispersion of the bulk plasmon given by equation 2.2 was later used to calculate the dispersion relation of these modes. The following analysis will closely follow the analysis of references [35,36]:

$$\left(\frac{d^2}{dt^2}\right)\vec{u} - B^2\vec{\nabla}(\vec{\nabla}\cdot\vec{u}) - \left(\frac{e}{m}\right)\vec{\nabla}f = 0 \quad (2.12)$$

where  $B$  is given by equation 2.2.b,  $\vec{u}$  is the macroscopic electron displacement vector from equilibrium, and  $\vec{u} = -\vec{\nabla}g$  defines the displacement potential  $g$ .

The bulk plasmon frequency is assumed to have the form given in equation 2.2 (the dispersion for small wave vectors), and for later convenience, we adopt the following definitions:

$$B^2p^2 = w_p^2 + B^2k^2 - w^2 \quad w^2 < w_b^2 \quad (2.13.a)$$

$$B^2q^2 = w^2 - w_p^2 - B^2k^2 \quad w^2 > w_b^2 \quad (2.13.b)$$

In these two energy regions, both  $g$  and  $f$  satisfy the relation:

$$\left(\frac{d^2}{dz^2} - k^2\right)\left(\frac{d^2}{dz^2} - j^2\right)g(z) = 0 \quad (2.14)$$

where 
$$j^2 = \begin{cases} p^2 & \text{for } w^2 < w_b^2 \\ -q^2 & \text{for } w^2 > w_b^2 \end{cases}$$

2 a

the  
ref  
ene  
equa

The  
from  
cond  
eige

where

and

The c  
that  
expon  
in ze

f and g are related by:

$$f(z) = \frac{m}{e} \left( B^2 \frac{d^2}{dz^2} - B^2 k^2 + w^2 \right) g(z) \quad (2.15)$$

In the following discussion, we let metal 1 occupy the space  $z < 0$ , and metal 2  $z > 0$ , and subscripts 1 and 2 refer to these metals. We also assume  $w_{b1} < w_{b2}$ . In the energy range  $w_{b1}^2 < w^2 < w_{b2}^2$ , the general solution for equation 2.14 is:

$$g_1 = A \cos(q_1 z + \varphi) + B e^{kz} \quad (2.16.a)$$

$$g_2 = C e^{-p_2 z} + D e^{-kz} \quad (2.16.b)$$

The electrostatic potential inside the metals is derived from equation 2.15. Then applying the appropriate boundary conditions, it was found in reference [36] that the eigensolutions satisfy the relation:

$$\cos \varphi + \sin \varphi \frac{L(w, k)}{K(w, k)} = 0 \quad (2.17)$$

where

$$L(w, k) = w_1^2 q_1 (w_2^2 - w^2) (w_2^2 + w_1^2 - 2w^2) \quad (2.18.a)$$

and

$$K(w, k) = kw^2 (w_2^2 - w_1^2)^2 - p_2 w_2^2 (w^2 - w_1^2) (2w^2 - w_1^2 - w_2^2) \quad (2.18.b)$$

The condition  $K(w, k) = 0$  corresponds to an interface mode that starts at  $\left[ \frac{1}{2} (w_1^2 + w_2^2) \right]^{1/2}$ . This branch represents an exponentially decaying mode in metal 2 and a pure cosine in metal 1. This mode was first observed by Miller and

Axe

Equ

sol

four

calc

for

This

As s

the d

narrow

condi

follo

ke, t

tion.

import

(Land

Debye

Axelrod at a Bi-Mg interface, as discussed in Chapter 1. Equation 2.17 can be solved, and Figure 2.3 shows the solution for several values of  $\varphi$  in the first and fourth quadrants for the Bi-Mg system. Those curves were calculated using the simplified solution of equation 2.17 for the primary branch which has the value  $w_{1-2}$  at  $k=0$ . This solution takes the form:

$$w^2 = \frac{w_1^2 + w_2^2}{2} (1 + c_1 k + c_2 k^2) \quad (2.19.a)$$

$$c_1 = \frac{[2(w_2^2 - w_1^2)]^{1/2} \cos \varphi}{[w_2^2 \cos \varphi / B_2 + w_1^2 \sin \varphi / B_1]} \quad (2.19.b)$$

$$c_2 = \frac{(w_2^2 - 3w_1^2)c_1^2}{2(w_1^2 + w_2^2)} \quad (2.19.c)$$

As shown in Figure 2.3, the modes are clustered close to the  $\varphi=0$  solution, and each mode arises from a relatively narrow plasmon band.

Jewsbury [2.3] has provided a rough estimate of the conditions for observing an interface plasmon using the following argument. For  $k$  below the cut-off wave vector  $k_c$ , the predominant excitation is the collective excitation. Above  $k_c$ , single-particle excitations become important, and plasmons decay into electron-hole pairs (Landau damping). The other cut-off wave vector  $k_D$ , the Debye cut-off, represents the upper limit for the existence

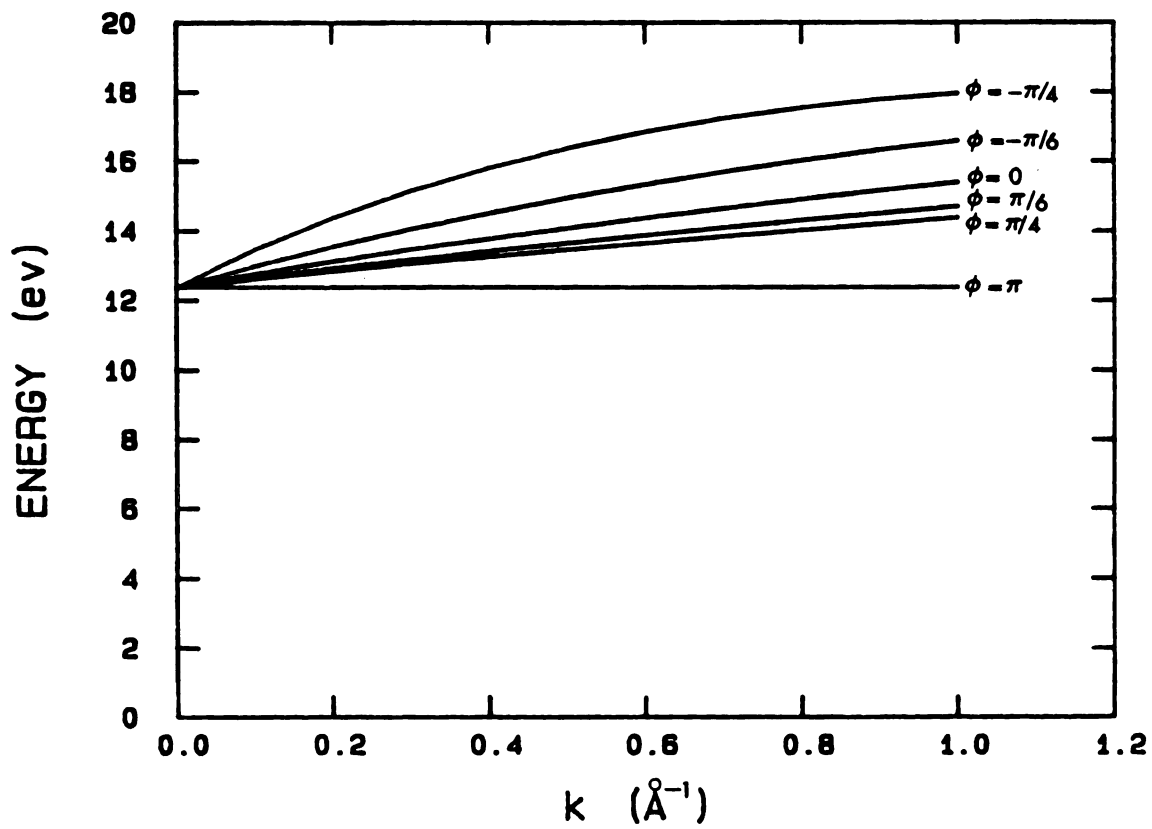


Figure 2.3 Dispersion of the Interface Plasmon at a Bi-Mg Junction



8  
x  
2

of bulk plasmons. These cut-off parameters are given by:

$$k_c = \frac{w_1}{v_{F1}} = \frac{0.9025}{r_s^{1/2}} \quad (2.20)$$

$$k_D = 1.26k_F = \frac{2.418}{r_s} \quad (2.21)$$

Using the dispersion relation of bulk plasmon in small  $k$  region given by equation 2.2, one can roughly estimate those systems where we can observe interface plasmons. The dispersion relation of the bulk plasmon combined with equation 2.20 gives:

$$w_{1-2}^2 \leq w_1^2 + 0.6w_1^2 = 1.6w_1^2 \quad (2.22)$$

This relation shows that we should observe an interface plasmon with frequency  $w_{1-2}$  anywhere between  $w_1$  (the lower plasmon of the two metals) and  $1.26 w_1$ . For higher  $w_{1-2}$ , the plasmon will suffer from Landau damping. Beyond  $k_D$ , the interface plasmons are forbidden.

In the NiV and NiMo systems, Ni has a plasmon with energy  $\sim 8$ ev, V a plasmon with energy  $\sim 11$ ev, and Mo a plasmon with energy  $\sim 10.5$ ev. Equation 2.22 shows that interface plasmons at  $\sim 9.5$ ev for both NiV and NiMo systems are in the allowed energy regime. Higher plasmons (at  $> 20$ ev) are outside the spectral region  $\epsilon_1/\epsilon_2 \leq 0$ , where interface plasmons may exist [58].

### 2.3 Collective Excitations in Metallic Superlattices

For a metallic film there are two types of plasmons: one type is the symmetric and anti-symmetric surface plasmons (Figures 2.1 and 2.2); the second type consists of bulk plasmons propagating in the plane of the film. For a superlattice, bands of the first type of plasmons can be obtained assuming a local theory. Bands of the second type require nonlocal theory ( $B \neq 0$  in equation 2.2). Nonlocal effects yield extra splittings in the interface plasmon bands obtained in the local limit.

#### 2.3.1 Collective and Surface Excitations in the Local Limit [58,61]

In this section, we make use of the local theory to investigate interface plasmon modes of metallic superlattices. In this limit, we recall that  $B$  in equation 2.2 is set equal to zero, and the dielectric function of the metals is given by equation 2.1.b. We first study the collective excitations of an infinite superlattice; second, we study the surface plasmons localized at the metal-vacuum interface of a semi-infinite superlattice.

##### 2.3.1.A Collective Excitations

We first consider an infinite superlattice illustrated in Figure 2.4. As discussed in Section 2.1, an isolated slab of metal 1 or 2 supports standing wave resonances (with frequencies for which  $\epsilon_1(\omega)$  or  $\epsilon_2(\omega)$  vanishes) which

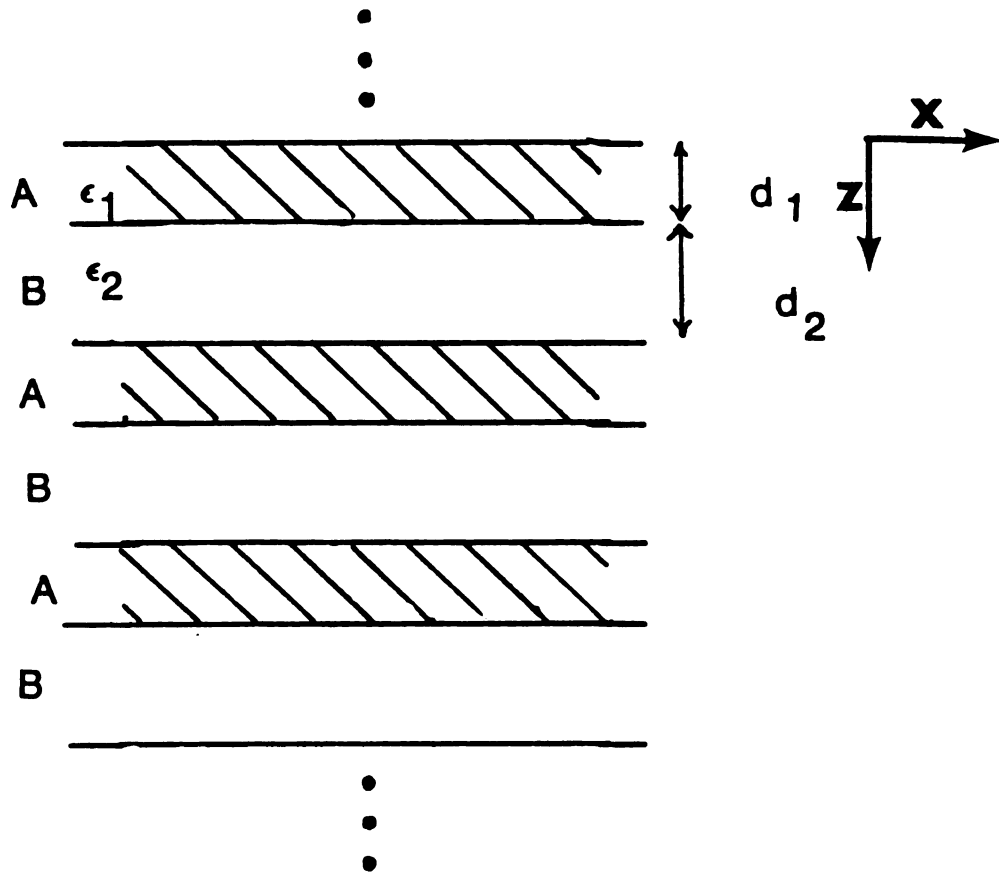


Figure 2.4 Schematic Diagram of an Infinite Superlattice

gen

Thus

slab

addi

stru

vand

ele

even

foun

Beca

satis

Hence

trans

form:

and f

Thus,

slab

So tha

f

generate a macroscopic field confined within the slab. Thus, in a superlattice such as that in Figure 2.4, each slab possesses bulk plasmons as in the isolated slab. In addition, there are collective excitations of the whole structure with frequencies  $\omega$  such that neither metal has a vanishing dielectric constant. In such a case, the electrostatic potential satisfies Laplace's equation everywhere. Combining equations 2.3.a and 2.4,  $f(z)$  is found to satisfy the differential equation:

$$\left(\frac{d^2}{dz^2} - k^2\right) f(z) = 0 \quad (2.23)$$

Because of the periodicity in the  $z$ -direction,  $f(z)$  must satisfy the proper boundary conditions at each interface. Hence the solution must form a Bloch wave, with respect to translations in the  $z$ -direction. Thus,  $f(z)$  takes the form:

$$f(z) = e^{iqz} U_q(z) \quad (2.24)$$

and for any integer  $n$ ,  $U_q(z)$  satisfies the relation:

$$U_q(z + n\Lambda) = U_q(z) \quad (2.25)$$

Thus, a general solution of equation 2.23 within the slab of metal 1 at  $n\Lambda \leq z \leq n\Lambda + d_1$  is:

$$U_q(z) = e^{-iq(z-n\Lambda)} [A_1 e^{k(z-n\Lambda)} + A_2 e^{-k(z-n\Lambda)}] \quad (2.26)$$

So that:

$$f(z) = e^{iqn\Lambda} [A_1 e^{k(z-n\Lambda)} + A_2 e^{-k(z-n\Lambda)}] \quad (2.27.a)$$

Similarly, in the slab of metal 2 at  $n\Lambda + d_1 \leq z \leq (n+1)\Lambda$  we have:

$$f(z) = e^{iqn\Lambda} [B_1 e^{k(z-n\Lambda - d_1)} + B_2 e^{-k(z-n\Lambda - d_1)}] \quad (2.27.b)$$

We then apply the proper boundary conditions to these solutions, i.e., the continuity of the electrostatic potential and the normal component of the electric displacement vector across the interface between the two metals at  $z=n\Lambda$  and  $z=n\Lambda + d_1$ . We thus obtain four equations involving the coefficients in equation 2.27. Then setting the appropriate 4x4 determinant equal to zero leads to the implicit dispersion relation:

$$\left[1 + \left(\frac{\epsilon_1}{\epsilon_2}\right)^2\right] \sinh kd_1 \sinh kd_2 + 2 \frac{\epsilon_1}{\epsilon_2} [\cosh kd_1 \cosh kd_2 - \cos q\Lambda] = 0 \quad (2.28)$$

where the explicit reference to the frequency dependence of the dielectric constant is dropped in equation 2.28 for convenience. This equation has the solution:

$$\frac{\epsilon_1}{\epsilon_2} = -c(k, q) \pm [c^2(k, q) - 1]^{1/2} \quad (2.29)$$

where:

$$c = \frac{\cosh kd_1 \cosh kd_2 - \cos q\Lambda}{\sinh kd_1 \sinh kd_2} \quad (2.30)$$

For real solution of the eigen frequencies, we must have  $c \geq 1$ . Hence, collective excitations occur in the frequency region for which  $\epsilon_1/\epsilon_2 \leq 0$ . This is the spectral region where surface plasmons may exist at the interface. The collective excitations discussed above may be viewed as a

sup

lay

str

kd,

an

and

w (

The

arou

only

down

disp

in t

rela

occu-

vacu

vicin

a so

repla

expon-

solut

superposition of surface plasmons which, for finite layer thickness, couple to form normal modes of the whole structure. Notice that in the limit  $kd_2 \gg 1$ , and a finite  $kd_1$ , equation 2.29 reduces to the dispersion relations of an isolated metal slab given in equation 2.7, as expected.

Equation 2.29 can be solved for the eigenfrequencies and hence we obtain the explicit dispersion relation:

$$\omega_{\pm}(k, q) = \left\{ \frac{\omega_1^2 + \omega_2^2}{2} \pm \frac{\omega_1^2 - \omega_2^2}{2} \left[ \frac{\cosh k(d_1 - d_2) - \cos q\Lambda}{\cosh k\Lambda - \cos q\Lambda} \right]^{1/2} \right\}^{1/2} \quad (2.31)$$

The general solution 2.31 consists of two bands with a gap around  $\omega_{1-2}$ . This gap closes when  $d_1 = d_2$ , where we have only one band with width  $(\omega_2 - \omega_1)$  at  $k\Lambda = 0$ , and narrows down to zero width for large  $k\Lambda$ . Figure 2.5 shows the dispersion relation of collective superlattice excitations in the NiV superlattice with  $d_1 = d_2$ . This dispersion relation is not affected by  $\Lambda$ .

### 2.3.1.B Surface Excitations

We now consider the semi-infinite superlattice occupying the half-space  $z > 0$ , while the half-space  $z < 0$  is vacuum. We are also interested in modes localized in the vicinity of the interface at  $z = 0$ . We obtain for such modes a solution identical to that in equation 2.27, with  $q$  replaced by  $i\beta$ , which implies that the solution decays exponentially in the superlattice. In the region  $z < 0$ , the solution has the form:

ENERGY (ev)

Figure  
a NIV

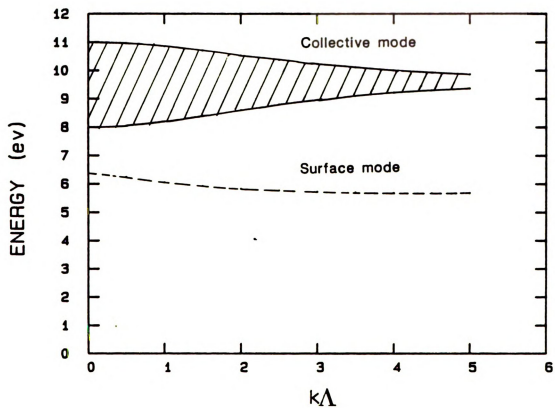


Figure 2.5 Dispersion of Interface and Surface Plasmons in a NiV Superlattice

z  
o  
p  
e  
2.  
eq  
th  
re

where

Comb  
disp

Equa  
solut  
start  
value  
vacuu  
super

$$f(z) = C \exp\{+kz\} \quad (2.32)$$

Upon applying the boundary conditions at  $z=n\Lambda$  and  $z=n\Lambda+d_1$  we obtain four equations involving the four coefficients of equation 2.27. We also apply the appropriate boundary conditions at  $z=0$  and obtain two other equations involving the coefficients in equations 2.26 and 2.32. We combine these six equations and obtain only three equations involving  $A_1$  and  $A_2$ . Those three equations are then combined to obtain the following implicit dispersion relations:

$$e^{-\beta\Lambda} = e^{-kd_2} [\cosh kd_1 + P_1 \sinh kd_1] \quad (2.33)$$

$$e^{-\beta\Lambda} = e^{+kd_2} [\cosh kd_1 + P_2 \sinh kd_1] \quad (2.34)$$

where:

$$P_1 = \frac{\epsilon_1^2 - \epsilon_2}{\epsilon_1(1-\epsilon_2)}, \quad P_2 = \frac{\epsilon_1^2 + \epsilon_2}{\epsilon_1(1+\epsilon_2)}$$

Combining equations 2.33 and 2.34 we obtain the implicit dispersion relation for the surface mode:

$$2 \cosh kd_1 \sinh kd_2 + \sinh kd_1 [P_2 e^{kd_2} - P_1 e^{-kd_2}] = 0 \quad (2.35)$$

Equation 2.35 gives two solutions for  $w$ . For  $d_1=d_2$ , one solution is constant and has the value  $w_{1-2}$ , the other starts at a frequency  $w_1 > w > w_1/2^{1/2}$ , and approaches the value of the surface mode of the metal in contact with vacuum. Figure 2.5 also shows the surface modes for a NiV superlattice with the Ni layer being in contact with the

va

in

ex

me

den

equ

the

ass

when

tion

$n(z)$

appli

coeff

relat

deter

F

super

assum

number

persio

vacuum at  $z=0$ .

### 2.3.2 Collective Excitations in the Non-local Limit

Eliasson et al. [62] used the hydrodynamic approach, including non-local effects, to investigate the collective excitations generated by coupling of bulk plasmons in metallic superlattices. The equation of motion for the density fluctuation  $n(z)$  was set up, and the differential equations obeyed by  $n(z)$  were derived in both materials of the superlattice. In the regime  $w_1 \leq w \leq w_2$  the solution was assumed to be:

$$n(z) = \begin{cases} Ae^{iqz} + Be^{-iqz} & , 0 \leq z \leq d_1 \\ Ce^{-pz} + De^{pz} & , d_1 < z < \Lambda \end{cases} \quad (2.36)$$

where  $q$  and  $p$  are given in equation 2.13. Bloch's condition (equation 2.27) was then used, and the continuity of  $n(z)$  and the current density  $j_z$  at the interfaces were applied at  $z=0$  and  $z=d_1$ ; thus, a set of equations for the coefficients  $A$ ,  $B$ ,  $C$ , and  $D$  were obtained. The dispersion relation was then obtained from the zeros of the  $4 \times 4$  determinant of the coefficients.

Figure 2.6.a shows the dispersion relation of the bulk superlattice plasmons calculated by Eliasson et al., assuming  $w_2^2 = 2w_1^2$ ,  $d_2 = 5d_1$ ,  $d_1 = 100\text{\AA}$ , and the equilibrium number density of electrons  $n_1 = 2.33 \times 10^{17} \text{cm}^{-3}$ . This dispersion relation is very nearly that for the NiV system,

1.4

$\frac{3}{4}$  1.2

1.0

0.0

Figur  
Metall

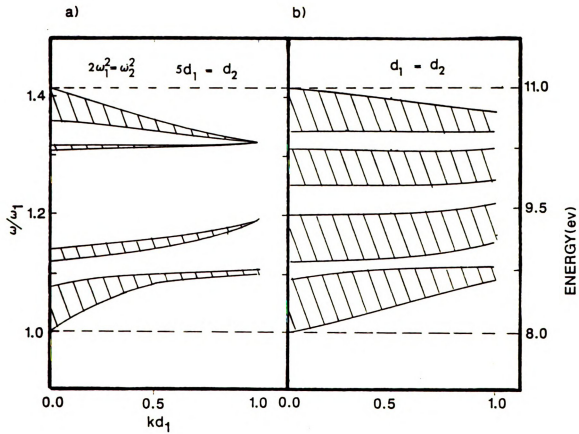


Figure 2.6 Dispersion Relation of Bulk Plasmons in Metallic Superlattices

si  
fo  
of  
la  
nan  
[6a  
san  
thi  
are  
in  
expe  
widt  
Ni a

since  $\omega_V^2 = 2\omega_{Ni}^2$ , however the assumed  $n_1$  is much smaller than for NiV. The large difference between the layer thicknesses of the two constituents results in large band gaps; as the layer thicknesses approach the same value, the band gaps narrow down. Figure 2.6.b (estimated from figure 2 in ref. [62]) shows qualitatively the dispersion relation of the same system as in Figure 2.6.a, except with equal layer thicknesses of the two constituents. The band gaps at  $k \sim 0$  are  $\sim 0.2$  eV. We would not be able to resolve such small gaps in EELS measurements with energy resolution  $\sim 0.7$  eV. Thus we expect to observe a single plasmon peak in NiV having a width of  $\sim 3$  eV, the difference between the bulk plasmons for Ni and V.

3.1

else

rat

diff

gas

is a

acce

of s

stab

sputt

preve

Mica,

contr

one b

contr

of th

film

grower

with

on the

## CHAPTER THREE

### SAMPLE PREPARATION AND CHARACTERIZATION

#### 3.1 Sample Preparation

ANL sample preparation by sputtering was described elsewhere [2,19]. Briefly, a target made of the desired material is placed in the vacuum system. The system is diffusion pumped to a base pressure of  $\sim 10^{-7}$  torr. An inert gas (Ar) is then admitted to the chamber. A high voltage is applied between the target and an anode to ionize and accelerate the ions to strike the target and produce a beam of sputtered atoms. Deposition rates are controlled by stabilizing the power input to the target.

For the preparation of superlattices, two or more sputtering guns are used. The guns are well separated to prevent overlap of the two atom beams. Substrates (such as Mica, Sapphire, NaCl, Si, etc.) are held on a temperature controlled, heated, rotating platform which moves them from one beam of atoms to the other. The layer thickness is controlled by the deposition rate and the rotational speed of the platform, and monitored by a quartz single crystal film thickness monitor.

A high degree of texture or epitaxy (i.e., coherent growth in which each deposited atomic layer is in registry with the previous layers) in the samples depends critically on the substrate temperature, the Ar pressure, the deposi-

tio

con

10-

tar

char

cryd

depo

prep

poss

insu

some

plat

and

can

can

rate.

subst

to be

targe

targe

of th

subst

epitax

tion rates, and the target-to-substrate distance. Typical conditions used for the preparation of ANL samples were: 10-15mtorr Ar pressure; 10-30Å/sec. deposition rates; 8in. target-to-substrate distance; and room temperature.

The MSU sputtering system and conditions are different than those of ANL in the following ways. The system is cryo-pumped down to  $\sim 10^{-8}$ torr, which produces a "cleaner" deposition atmosphere. Masks are used and enable the preparation of different samples with different periods and possibly different constituents (from conductors to insulators) due to the availability of four different guns, some of which are fed with an RF power supply. The platform with the substrates oscillates between the guns, and the time a substrate spends in a given beam of atoms can be controlled; thus, the layer thickness essentially can be controlled without having to change the deposition rate.

For preparing MSU samples, the Ar pressure, the substrate temperature, and the deposition rates were chosen to be similar to those used for preparing ANL samples. The target-to-substrate distance used at MSU was 4in. Longer target-to-substrate distances usually moderate the energy of the beam of atoms, so that the atoms arrive at the substrate with energy that is too low to disturb the epitaxy.

## 3.2 Structural Properties of Superlattices

### 3.2.1 $\theta/2\theta$ X-Ray Diffraction (XRD)

XRD is widely used to study the structural properties of both semiconductor [63] and metallic [64] superlattices. In reflection geometry, the momentum transfer  $q$  is perpendicular to the surface of the sample (and hence to the layers); thus, structural information perpendicular to the layers is obtained.

Since the ANL samples studied in this thesis were prepared several months, or even a year, before the time of our EELS measurements, we thought it was important to remeasure the  $\theta/2\theta$  XRD characteristics of these samples, to check that the interfacial information obtained by Schuller's group [19] was still appropriate. We later extended the structural characterization to samples prepared at MSU. To analyze the data, we adopted the simple one-dimensional diffraction model previously used [65,19] to fit the experimental data. This model assumes sharp interface boundaries and ignores effects of strains at the interfaces.

#### 3.1.1.A One-Dimensional Diffraction Theory of Superlattices

As a first approximation, we assume a perfect superlattice of constituents A and B. The separation of the atomic planes (the d-spacing) of these materials is  $d_1$  in material A and  $d_2$  in material B, as measured in the bulk.

7

e

a

an

an

an

the

po

giv

Here

dens

[66]

the

Furt

late

the

stru

and

The layer thicknesses of the two materials is assumed equal, as is the case with our samples. The number of atomic planes of the two constituents in their layers is  $N_1$  and  $N_2$ .

The period ( $\Lambda$ ) of the superlattice is then given by:

$$\Lambda = d_1 N_1 + d_2 N_2 \quad (3.1)$$

and the average d-spacing over the superlattice [19] is given by:

$$\bar{d} = \frac{\Lambda}{N_1 + N_2} \quad (3.2)$$

X-rays falling on the sample will be reflected from the planes of the two materials with planar scattering powers  $F_1$  and  $F_2$ , where the planar scattering power is given by:

$$F = f\sigma \quad (3.3)$$

Here  $f$  is the atomic form factor and  $\sigma$  is the atomic planar density.

The form factor can be obtained from tabulated results [66], and the atomic planar density can be calculated from the lattice parameter  $a$  and the structure of the lattice. Furthermore, it is known that in NiV and NiMo the BCC lattices grow in the (110) direction, and the FCC grow in the (111) direction [20]. The planar density of the BCC structure is:

$$\sigma_{\text{BCC}} = \frac{2^{1/2}}{a^2} \quad (3.4.a)$$

and that of an FCC structure is:

1  
w  
t  
e

tn

w  
the  
q-s  
3.5

give

wher

give

plan

cont

is e

Appi

$$\sigma_{\text{FCC}} = \frac{4}{3^{1/2} a^2} \quad (3.4.b)$$

An incident x-ray beam with wave vector  $\vec{k}_0$  and wave length  $\lambda$  scatters from the one-dimensional lattice with wave vector  $\vec{k}$ . In the process, it transfers momentum  $\vec{q}$  to the lattice in the z direction. Since the scattering is elastic, i.e.,  $|\vec{k}_0| = |\vec{k}|$ , we obtain:

$$q = 4\pi \frac{\sin \theta}{\lambda} \quad (3.5)$$

The position  $\theta$  of the reflection peak of order n from the lattice is given by Bragg's law:

$$2D \sin \theta = n \lambda \quad (3.6)$$

where D is a characteristic length that is determined by the periodicity of the system. Hence, the position in q-space of that reflection can be obtained from equations 3.5 and 3.6:

$$q = \frac{2 \pi n}{D} \quad (3.7)$$

The scattering amplitude [3.5] from the lattice is given by:

$$S(n) = \sum_p F_p \cdot \exp\{i \vec{x}_p \cdot \vec{q}\} \quad (3.8)$$

where  $F_p$  is the scattering power from the pth plane as given in equation 3.3, and  $\vec{x}_p$  is the position of that plane.

Since the system is periodic in the z direction, the contribution to the scattering amplitude of the pth plane is equal to the contribution of the  $(N_1 + N_2 + p)$ th plane. Applying this boundary condition to equation 3.8, and

x

s

n

th

is

the

lat

to

refl

latt

the

tice

main

fixe

is g

appli

time

Hence

keeping in mind that  $\vec{q}$  is parallel to  $\vec{x}_p$ , so that  $\vec{x}_p$  is simply the z-coordinate of the pth plane, we obtain:

$$\exp\{i(N_1 d_1 + N_2 d_2) q\} = 1 \quad (3.9)$$

From which we obtain:

$$q = \frac{2\pi n}{\Lambda} \quad (3.10)$$

Equations 3.7 and 3.10 show that the period  $\Lambda$  defines the periodicity of the system, and hence  $D$  in equation 3.7 is simply  $\Lambda$ .

The d-spacing corresponding to the nth reflection is then given by:

$$d_n = \frac{\Lambda}{n} \quad (3.11)$$

From equation 3.2 for the average d-spacing of the lattice, and equation 3.11 for the d-spacing corresponding to the nth reflection, we notice that there is always a reflection corresponding to the average d-spacing of the lattice, and that the order of that reflection is equal to the sum of the atomic planes of one period in the superlattice. In the model chosen, the position in q-space of the main line (that corresponding to the average d-spacing) is fixed, independent of the period of the superlattice, and is given by equation 3.10.

In using equation 3.8 to calculate the scattering amplitude from the crystal, we must bear in mind that the dimension of the crystal in the z direction is finite. Hence, we need to add up contributions from a finite number

W  
P  
3  
W  
S  
:

To  
trie  
[66]  
cove  
The  
the  
The  
param  
tion

of planes. The finite size of the stack of atomic planes in the z direction (the coherence length) results in broadening of the diffraction peaks. This length can be viewed as the length of the crystal in the z direction over which reflections from the atomic planes are almost in phase, and hence add up constructively. In using equation 3.8, contributions from planes in a total of  $N_T$  periods will be added; hence, the coherence length is  $N_T \Lambda$ . The scattered intensity as a function of q is then given by:

$$I(q) = \left| F_1 \frac{\sin(qd_1 N_1 / 2)}{\sin(qd_1 / 2)} + F_2 e^{iq\Lambda / 2} \frac{\sin(qd_2 N_2 / 2)}{\sin(qd_2 / 2)} \right|^2 \times \frac{\sin^2(q\Lambda N_T / 2)}{\sin^2(q\Lambda / 2)} \quad (3.12)$$

To determine the planar scattering powers  $F_1$  and  $F_2$ , we tried various alternative fits to tabulated x-ray data [66] for Ni, V, and Mo in the range  $1.5 \leq q \leq 6.5 \text{ \AA}^{-1}$ , which covers the range of q in XRD spectra of the superlattices. The best fits were obtained with an exponential function of the form:

$$F = A e^{-Bq} \quad (3.13)$$

The fitting parameters A and B were evaluated. The various parameters (other than  $\Lambda$ ) needed for the spectral calculation are given in Table 3.1.

MS  
N  
V  
M

sm  
la  
to  
we

super  
line  
peak  
exper  
spect  
the s  
spect  
evolut  
A bec  
lines,  
diffr  
of the

Table 3.1 Fitting Parameters for Structure Factor Calculations of the Superlattices

Material	d(Å)	Parameter	
		A	B(Å)
Ni	2.03	6.0	0.144
V	2.14	4.0	0.153
Mo	2.22	6.5	0.120

The value of A for Mo was found to be a little too small to fit the experimental XRD spectra for NiMo superlattices, especially for  $\Lambda > 50\text{\AA}$ . The value (8.0) was found to be much better, and the resulting spectra agree very well with the experiment.

### 3.2.1.B Experimental Results and Analysis

Figure 3.1 shows typical experimental spectra for NiMo superlattices prepared at ANL, together with the calculated lines normalized such that the intensity of the strongest peak is equal to that of the corresponding peak in the experimental spectra. The calculated and experimental spectra were superimposed for comparison. Figure 3.2 shows the spectra for ANL NiV superlattices with the calculated spectra. In both systems we observe the same pattern of evolution, which agrees with the calculation. Moreover, as  $\Lambda$  becomes smaller than  $\sim 15\text{\AA}$ , the spectrum shows no sharp lines, but rather a broad peak, reminiscent of the diffraction pattern of an amorphous structure. The width of the "amorphous" spectra indicate that the coherence

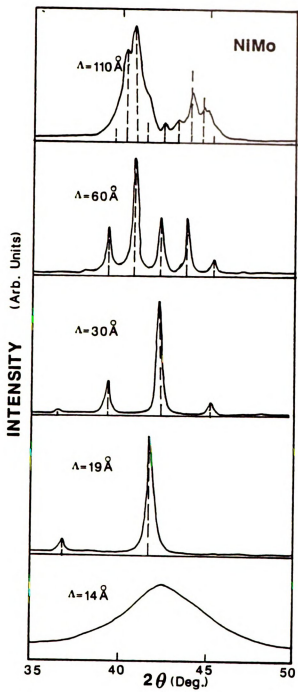


Figure 3.1 XRD Spectra and Structure Factor of ANL NiMo Superlattices

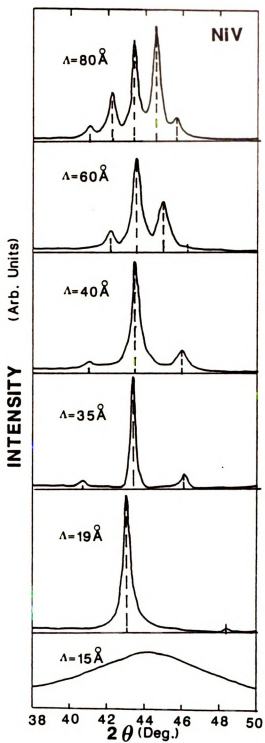


Figure 3.2 XRD Spectra and Structure Factor of ANL NiV Superlattices

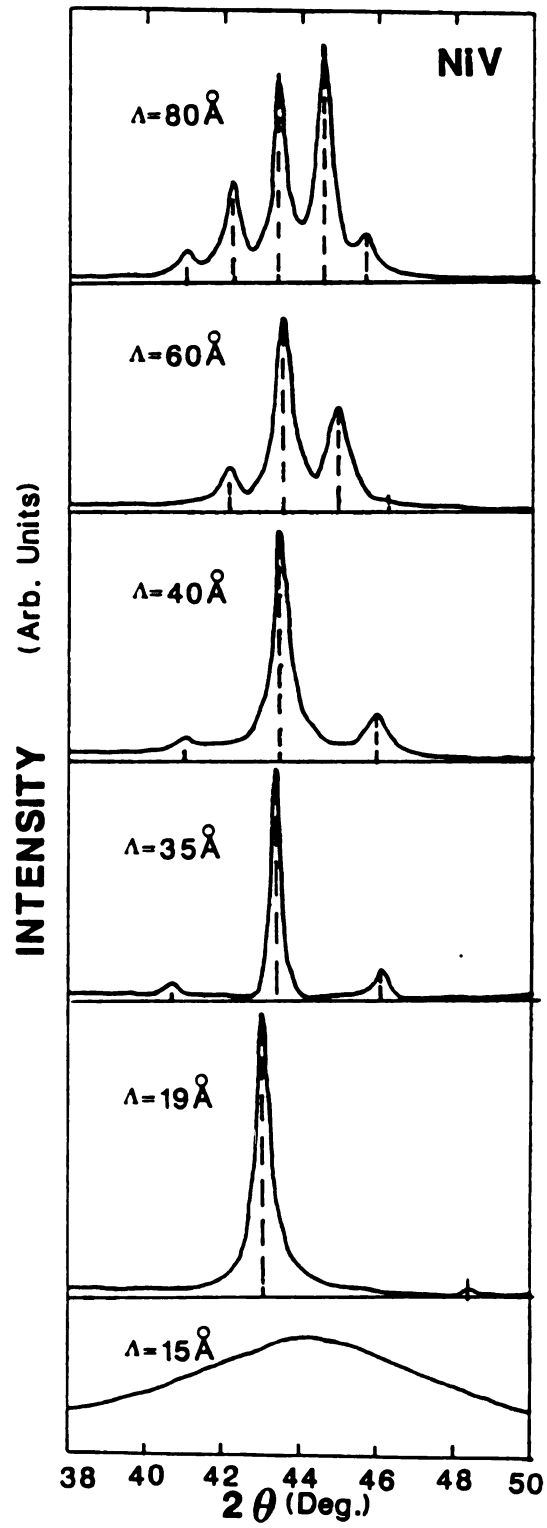


Figure 3.2 XRD Spectra and Structure Factor of ANL NiV Superlattices

length is  $\sim 20\text{\AA}$ . The transition from a layered structure to a nonlayered "amorphous" one seems to be fairly sharp (within  $\sim 1$  atomic plane).

The superlattices with  $\Lambda \sim 19\text{\AA}$  are not very uniform. X-ray spectra on different parts of the same sample show that the diffraction pattern from some places on the sample shows a single sharp peak (the main peak corresponding to the average d-spacing), on top of a broad, amorphous-like peak. This indicates the existence of disorder coexisting with layered structure in the same sample. The weak signal and the possibly diffuse interfaces in these regions of the sample do not allow the detection of any satellite around the main peak. Figure 3.3 shows the diffraction pattern from two different pieces of the same NiMo sample of period  $\sim 19\text{\AA}$ .

Furthermore, the position of the main line in the diffraction patterns was found to move down in q-space as  $\Lambda$  decreased down to  $19\text{\AA}$ . For  $\Lambda \leq 15\text{\AA}$ , the center of the broad peak moved back to approximately the position corresponding to the samples with large  $\Lambda$ . This effect had been observed previously in the NiMo system [19]. Figures 3.4 and 3.5 show the experimental values of  $(1/\bar{d})$  vs.  $\Lambda$  for NiMo and NiV superlattices, respectively. The positions of Bragg peaks from the substrates were used to calibrate the q-axis.

Figure 3.4 shows that, for large  $\Lambda$ ,  $1/\bar{d}$  reaches the

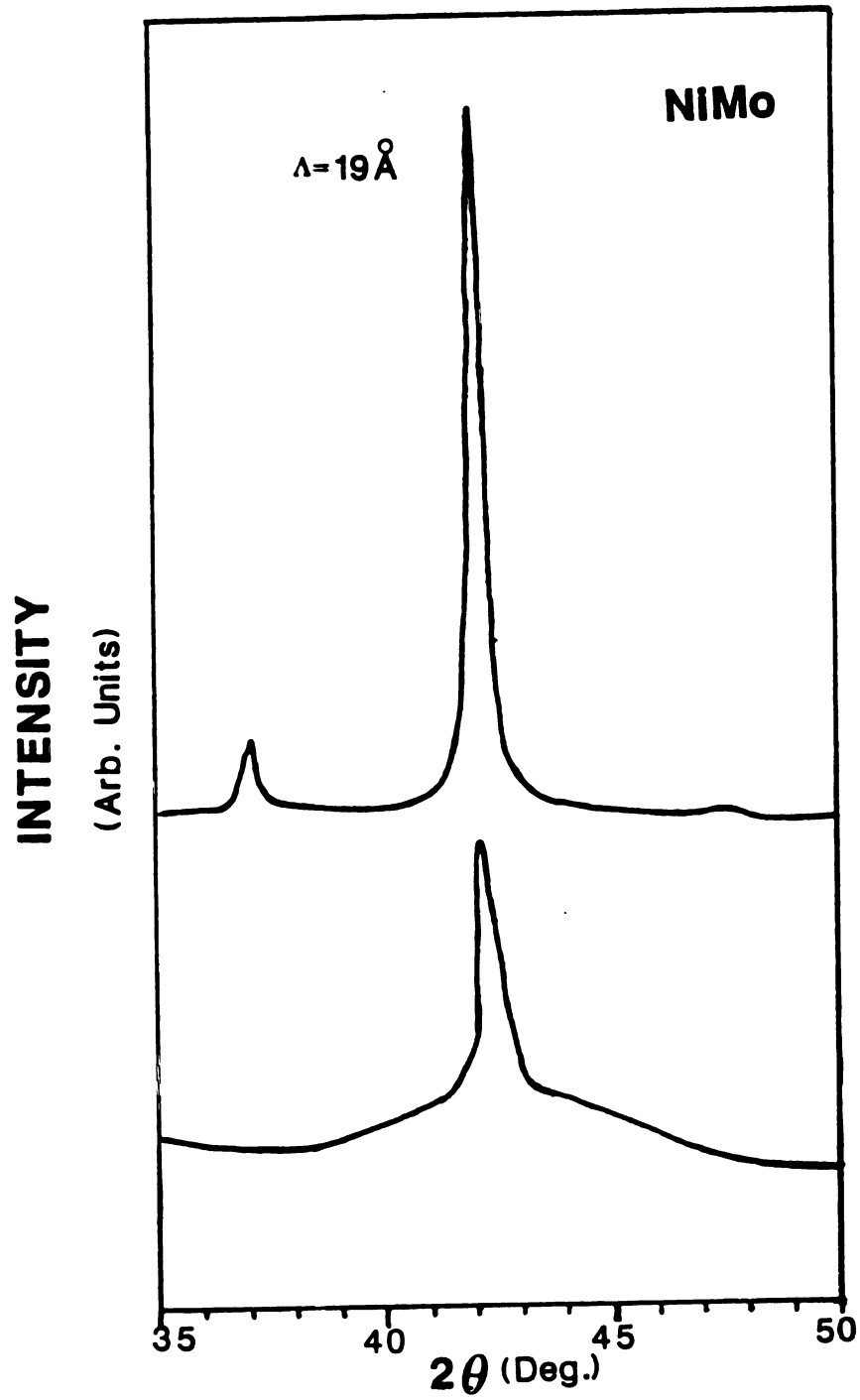


Figure 3.3 XRD Spectra in Two Different Pieces of the ANL 19Å NiMo Superlattice

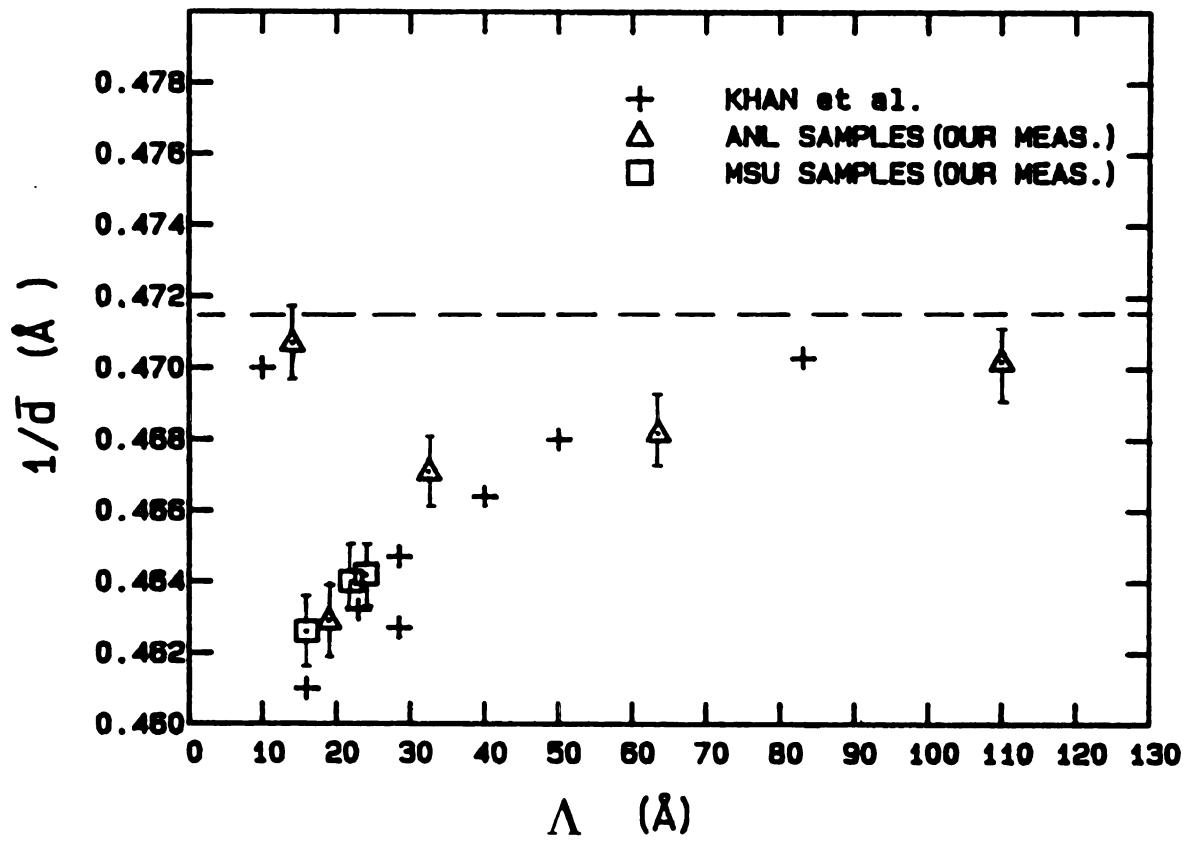


Figure 3.4 The Behavior of the Average d-spacing in NiMo Superlattices

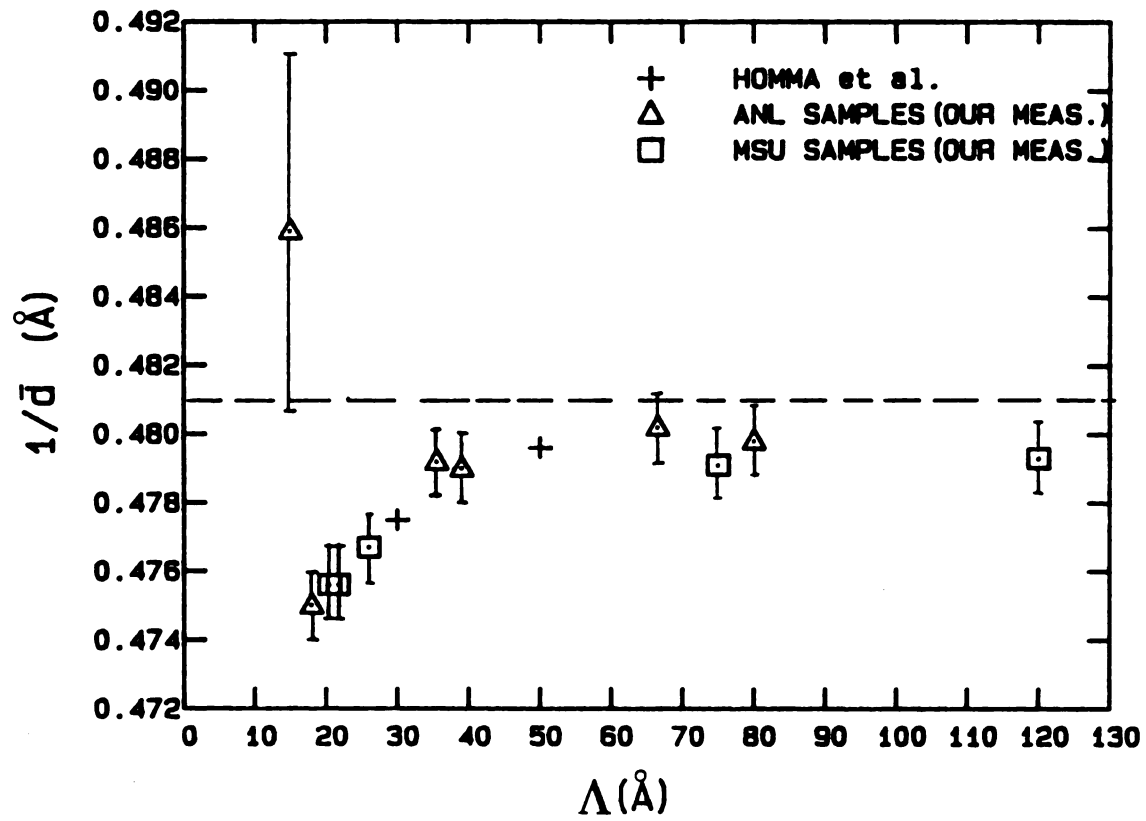


Figure 3.5 The Behavior of the Average d-spacing in NiV Superlattices

calculated value (dashed lines) using equation 3.2. As  $\Lambda$  decreases,  $1/\bar{d}$  decreases until  $\Lambda \sim 19\text{\AA}$ , when the difference between large  $\Lambda$  and small  $\Lambda$  values of  $1/\bar{d}$  reaches  $\sim 2\%$ , in agreement with the results of reference [19]. For  $\Lambda \sim 14\text{\AA}$ , the center of the broad peak moves back to approximately the calculated value.

Figure 3.5 shows that the NiV system exhibits a similar behavior. The change in  $1/\bar{d}$ , however, is  $\sim 1\%$ , half of the effect observed in the NiMo system. For  $\Lambda = 15\text{\AA}$ , the peak is broad and the uncertainty in locating its center is large.

These experimentally observed expansions in the average d-spacings for NiMo and NiV as  $\Lambda$  decreases have no analogue in the calculation. In addition to this expansion perpendicular to the layers, a slight expansion in the Ni spacing and a comparable contraction in the Mo spacing parallel to the planes have been reported [19].

The coherence lengths of these systems were crudely estimated from the experimental line widths of the central Bragg peaks of the superlattices. The instrumental width was estimated to be equal to the width of a sharp Mica line. The line shapes of both the Bragg peaks and the instrumental width were assumed to be Lorentzian; thus, in correcting for the instrumental width, we simply subtracted the instrumental width from the width of the central Bragg peak of the superlattices. This procedure gave a coherence

length of  $\sim 300\text{\AA}$  for both the NiV and NiMo systems prepared at ANL. This result is in qualitative agreement with the coherence lengths of  $\sim 100\text{\AA}$  for NiMo system obtained by Khan et al. [19], and of  $\sim 700\text{\AA}$  for NiV system obtained by Homma et al. [20]. MSU-prepared samples that showed superlattice lines had a coherence length of 100-200 $\text{\AA}$ .

### 3.2.2 Electron Diffraction (ED)

The structure of materials can be divided into two broad categories: amorphous and crystalline, according to the degree of long-range order of the atoms in the material. A material with no ordered structure is considered amorphous, while a material in which the same structure repeats over the entire macroscopic sample is said to be a single crystal. Between the two extremes we find the polycrystalline materials in which the atoms are arranged in small crystallites that are usually randomly oriented in the bulk of the sample [18].

A portion of the electrons passing through thin films of matter are scattered elastically by the atoms. As in the case of x-rays, crystal planes diffract these electrons in well-defined directions [68] governed by Bragg's Law, giving strong, narrow peaks, while amorphous materials scatter the electrons in a wide range of angles, giving a weak, broad peak.

The wave length of 100 Kev electrons is  $\sim 0.037\text{\AA}$ , which

gives an angular diffraction of the electron beam from a typical crystal plane of  $\sim 10\text{mrad}$  ( $0.5^\circ$ ) for  $d \sim 2\text{\AA}$ . This deflection angle is about two orders of magnitude smaller than in the case of XRD, which accounts for the poorer resolution of ED. In ED experiments, we observe more reflections than in the case of XRD, since the Ewald sphere for electrons has a larger radius, and intersects more points in the reciprocal space of the sample [69].

### 3.2.2.A The Electron Diffraction Camera and Bragg Reflection

A parallel electron beam falling on a crystal at an angle  $\theta$  with lattice planes separated by a distance  $d$  diffracts through an angle  $2\theta$  from the undeviated beam. If a detector is located a distance  $L$  from the sample, a diffraction spot corresponding to the lattice spacing  $d$  will be detected at a distance  $R=L\tan 2\theta$  from the central spot of the undeviated beam. Using Bragg's Law, along with the fact that, for electron scattering, the angle  $\theta$  is small ( $\sin\theta=\tan\theta=\theta$ ), we obtain a formula for the  $d$ -spacing of the lattice planes:

$$d = \frac{\lambda L}{R} \quad (3.14)$$

$L$  is the camera length, and  $\lambda$  is the wave length of the electron beam.

If the beam falls on a region of the sample that contains more than one set of lattice planes with different

d-spacings, a diffraction pattern (DP) of several spots will be observed. If the region of the sample contains very small crystallites that are randomly oriented, rings with different radii  $R$  will be observed. Each ring with a radius  $R$  corresponds to reflection from a set of planes with a d-spacing that is related to  $R$  through equation 3.14. The widths of the rings are determined by the sizes of the crystallites. Crystallites as small as  $\sim 10\text{\AA}$  still give fairly sharp rings. Amorphous materials, in contrast, give a broad, diffuse ring associated with the closest distance of approach of the atoms [69]; a weak second-order ring associated with the second nearest neighbor correlation might also be observed. For accurate measurements of the radii of the rings, it is best to use a microdensitometer, or the line scan facility available in the FE-STEM. The line scan facility provides a horizontal scan of the beam across the diffraction pattern, and gives peaks corresponding to the rings. The radii of the diffraction rings are then measured to within  $<2\%$ . Knowledge of the camera length  $L$  as well as of the radius of the diffraction ring allows the calculation of the d-spacing of the set of planes giving rise to the diffraction ring under consideration.

The combination of the electron gun, the sample holder, and the detector constitutes the electron diffraction camera.  $\lambda L$  is called the camera constant. The

camera length in the FE-STEM can be varied from 10 to 5000cm.

### 3.2.2.B Selected Area Diffraction (SAD) and Microdiffraction (MD)

In the selected area diffraction (SAD) mode, a parallel beam of electrons falls on the sample, and a diffraction pattern (DP) from a certain area of the sample is viewed on the CRT screen. The investigated area of the sample can be controlled by means of the SAD aperture. An area as small as  $\sim 1\mu^2$  can be measured by choosing a  $25\mu$  aperture. The resolution of the DP is controlled by the size of the collector aperture (CA). A  $150\mu$  or  $50\mu$  collector aperture gives a reasonably high resolution DP with momentum resolution  $\sim 0.1\text{\AA}^{-1}$ . Figure 3.6 shows the DP of a  $300\text{\AA}$  thick FCC polycrystalline Ni film prepared at MSU, and of an amorphous FeZr film prepared at ANL. Both films were sputtered on NaCl substrates. Table 3.2 shows the Miller indices of the Ni planes responsible for the observed diffraction rings. The camera constant of  $2.145\text{\AA cm}$  was obtained by matching the calculated and the observed d-spacings of the (111) and (200) Ni lattice planes.

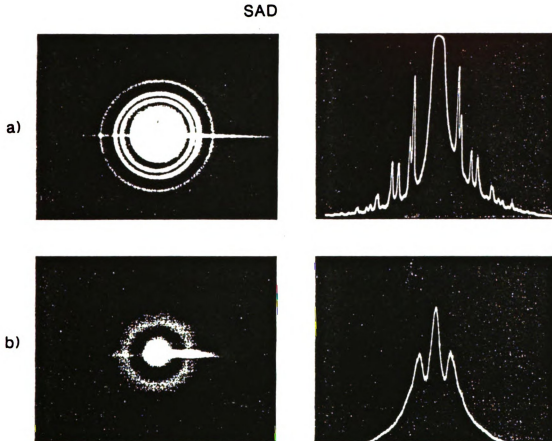


Figure 3.6 SAD of (a) Crystalline Ni, and (b) Amorphous FeZr Films

Table 3.2 The d-spacing and the Miller Indices of the Ni Planes Responsible for the observed Reflections

<u># of Reflections</u>	<u>d<sub>exp.</sub> (Å)</u>	<u>hkl</u>	<u>d<sub>calc.</sub> (Å)</u>
1	2.043 $\pm$ 0.024	111	2.032
2	1.751 $\pm$ 0.018	200	1.760
3	1.243 $\pm$ 0.009	220	1.245
4	1.059 $\pm$ 0.007	311	1.061
5	0.867 $\pm$ 0.015	400	0.880
6	0.794 $\pm$ 0.010	331	0.808
		420	0.787
7	0.715 $\pm$ 0.006	422	0.719
8	0.670 $\pm$ 0.007	511	0.677
		333	0.677
9	0.617 $\pm$ 0.006	440	0.622
10	0.584 $\pm$ 0.005	531	0.595
		442	0.587
		600	0.587

In the Microdiffraction (MD) mode, a convergent beam of small spot size ( $\sim 10\text{Å}$ ) falls on the sample, and gives a DP from very small regions of the sample. The resolution of the MD pattern can be controlled by the sizes of the objective aperture (OA) and CA. Because the beam converges at the spot under investigation, a range of incident angles exist simultaneously, which leads to broader diffraction spots and hence to poorer angular resolution than in the case of SAD. Figure 3.7 shows a microdiffraction pattern on a region of the Ni film. An estimate of the crystallite size of the Ni was obtained by moving the beam across the sample until the MD pattern changed. The estimate of  $\sim 100\text{Å}$  was in qualitative agreement with the crystallite size of  $\sim 50\text{Å}$  estimated from the width of the first diffraction peak in the SAD pattern.

In the MD mode, a double-tilt goniometer specimen

MD

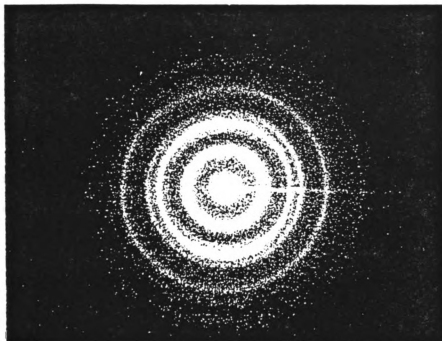


Figure 3.7 MD of a Crystalline Ni Film

stage is used to obtain a recognizable diffraction pattern of the portion of the sample under investigation. Tilting the sample moves the portion of the sample of interest away from the beam. This problem can be solved by tilting the sample while in imaging mode, where we can shift the beam back to the point of interest. This procedure, however, is lengthy, especially if the microcrystallites are  $<30\text{\AA}$  in size. An additional difficulty in using MD to study the structure of such microcrystallites is that the drift per minute of the beam can be larger than the size of the crystallites. In this section we will be mainly concerned with using SAD to study the in-plane structure of NiV superlattices of total thickness  $<1000\text{\AA}$ . The NiMo samples were not characterized by ED since these samples were thick ( $\sim 1\mu$ ).

To investigate local variations in structure, we measured pieces of the  $19\text{\AA}$  sample grown on NaCl substrate at ANL with total thickness  $\sim 1000\text{\AA}$ . The DP differed from one place in the sample to another. In some places, we obtained a DP with several sharp and well resolved rings. Figure 3.8 shows the diffraction pattern that is typical for such regions in the film. The d-spacings were calculated from the peaks in the line scan. Those d-spacings are shown in Table 3.3, together with the indices and calculated d-spacings for those lattice planes of pure Ni and V that are within 2% of the experimental d-spacings.

Diffraction pattern



Line scan

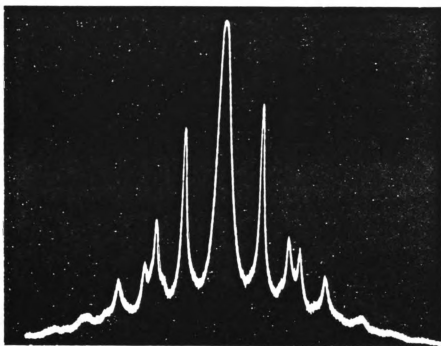


Figure 3.8 SAD of ANL 19Å NiV Superlattice

Table 3.3 The Experimental d-spacings of the NiV Superlattice with  $\Lambda = 19\text{\AA}$ , Along with the Indices and Calculated d-spacings of NiV Lattice Planes that are within 2% of the Observed Ones

<u># of Reflection</u>	<u>d<sub>exp.</sub> (Å)</u>	<u>metal(hkl)</u>	<u>d<sub>calc.</sub> (Å)</u>
1	2.145 $\pm$ 0.027	V(110)	2.135
2	1.262 $\pm$ 0.018	Ni(220)	1.245
3	1.073 $\pm$ 0.013	Ni(311)	1.061
		V(220)	1.068
4	0.802 $\pm$ 0.007	Ni(331)	0.808
		Ni(420)	0.787
		V(312)	0.807
5	0.715 $\pm$ 0.006	Ni(422)	0.719
		V(330)	0.712
6	0.613 $\pm$ 0.588	Ni(440)	0.622
		V(422)	0.616
		V(510,4)	0.592
		Ni(531)	0.595
		Ni(600,4)	0.587

The diffraction ring corresponding to the Ni (220) reflection shows an azimuthal nonuniformity of the intensity, which means that in-plane crystal orientation is preferred in certain directions. The sixth peak in Figure 3.8 is broad, apparently due to the combination of several Ni and V peaks. From the widths of the peaks we estimated the crystallite size to be  $\sim 40\text{\AA}$ . Figure 3.8 also shows several other weak reflections which were not presented in Table 3.3. The shoulder between the first and second peaks corresponds to the V (200) reflection, and the hint of a peak between the third and fourth peaks corresponds to the weak Ni (400) reflection. The tail of the pattern shows a very broad, weak peak corresponding to a combination of higher order Ni and V reflections. Those reflections are not presented in Table 3.3 because they were weak and

dominated by the tails of other peaks, and hence their positions have uncertainty  $>2\%$ .

Figure 3.9 shows the diffraction patterns of three other regions of the sample. We notice that the diffraction peaks are broader, indicating smaller crystallites. The crystallite size in cases c and d was estimated to be  $\sim 10\text{\AA}$ . The DP in case a shows a structure that is between that of crystalline and amorphous, with an apparent crystallite size of  $\sim 7\text{\AA}$ . DPs b and c in Figure 3.9 show additional examples of crystal orientation preference (e.g., in b the intensity of the Ni (220) reflection is comparable to that of the V (110) in the direction of the line scan). The intensities of the Ni (311) and V (220) reflections are very small, which means that there are very few crystallites with those planes oriented in the direction of the line scan. The above results show large variations in the structure and the in-plane grain sizes in different regions of the sample.

The  $\Lambda=60\text{\AA}$  sample showed a more nearly uniform structure with in-plane grain size  $\sim 20\text{\AA}$ . The rings still showed anisotropic intensity distribution which indicated preferential crystal orientation in certain directions. Figure 3.10 shows the DP in three different regions of the sample. The peaks correspond to the reflections given in Table 3.3 for the  $19\text{\AA}$  sample. The  $\sim 0.6\%$  expansion in Ni spacing for the thinnest samples observed by Khan et al.

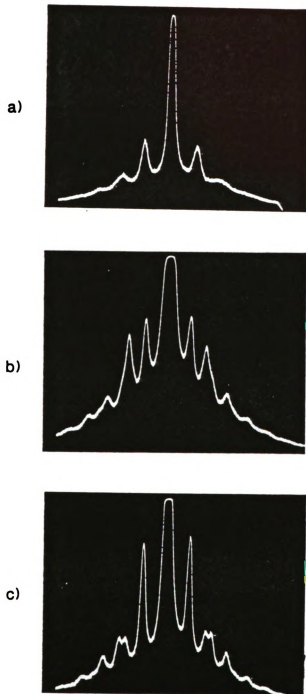


Figure 3.9 SAD in Three Different Regions of ANL  $19\text{\AA}$  NiV Superlattice

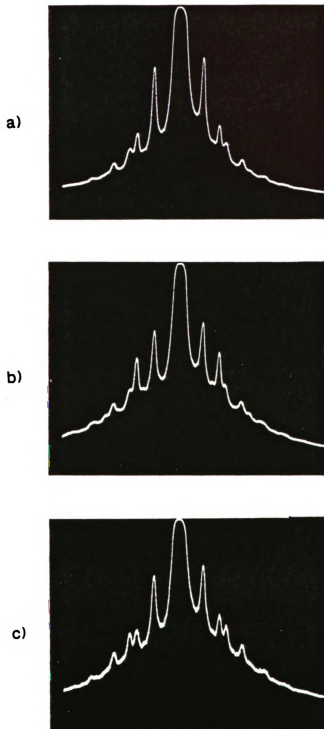


Figure 3.10 SAD in Three Different Regions of ANL  $60\text{\AA}$  NiV Superlattice

[19] was not resolved in our ED experiments and hence, to within the experimental uncertainty of  $<2\%$ , the d-spacings for large and small  $\Lambda$  samples are the same.

We also studied the structure of samples prepared at MSU. The  $\Lambda = 27\text{\AA}$  sample showed large structural variations. Most of the regions showed broad diffraction peaks, from which we estimated the grain size to be  $<10\text{\AA}$ . The DP in some regions indicated an amorphous structure. In one region, the diffraction peaks were sharp, indicating a grain size of  $\sim 30\text{\AA}$ . Figure 3.11 compares the structure in three different regions of the film. Figure 3.11.c shows a stronger peak corresponding to the V (200) reflection than in any other sample. This pattern was isotropic, indicating that there was no preferential in-plane orientation of the crystallites.

At different spots, the  $\Lambda = 15\text{\AA}$  sample prepared at MSU showed either an amorphous structure or wide diffraction peaks indicative of crystallite sizes  $\sim 10\text{\AA}$ . MD in crystalline and amorphous regions was obtained; the regions where the SAD looked amorphous gave an amorphous MD structure (a wide diffuse ring), while the crystalline regions gave a MD pattern that was a superposition of amorphous and crystalline structure, as indicated by hints of spots superimposed on the diffuse ring. Figure 3.12 shows typical SAD and microdiffraction patterns on two different regions of the film.

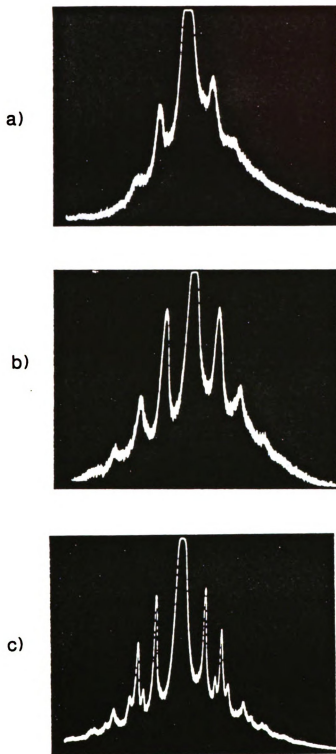


Figure 3.11 SAD in Three different Regions of MSU  $27\text{\AA}$  NiV Superlattice

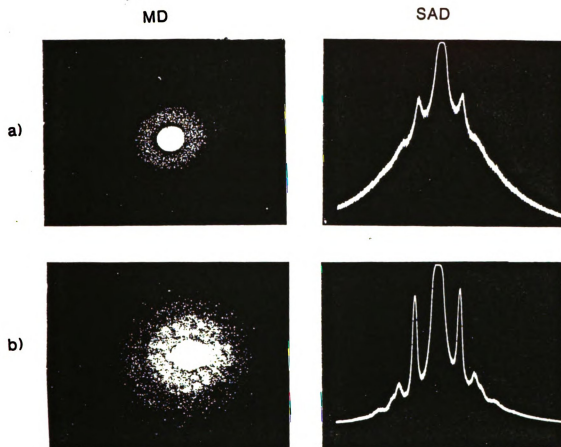


Figure 3.12 SAD and MD in Two Different Regions of MSU 15Å NIV Sample

The above results indicate that samples with large  $\Lambda$  seem to have a relatively uniform structure with in-plane grain size of  $\sim 20\text{\AA}$ . The reflections observed in such samples correspond, within experimental uncertainty, to reflections obtained from pure materials. For the  $19\text{\AA}$  sample, we observed variations in the grain sizes from  $\sim 40\text{\AA}$  down to  $\sim 7\text{\AA}$ . The in-plane structure in most of the regions of the  $27\text{\AA}$  MSU sample did not show crystallite sizes as large as those of ANL. The MSU- $15\text{\AA}$  sample showed small grain sizes and amorphous structures in various regions. Microdiffraction at different spots of the sample confirmed the amorphous nature of certain regions of the film. These results suggest that different sample preparation conditions (such as the target-to-substance distance) used in preparing ANL and MSU samples affect the crystallinity of the samples.

### 3.3 Energy-Dispersive X-Ray (EDX) Microanalysis

The development and improvement of the FE-STEM electron microscope system, with high accelerating voltages ( $\geq 100\text{Kev}$ ), and high probe current densities ( $\sim 10^9\text{Amp./cm}^2$ ) together with small probe size ( $\sim 5\text{\AA}$ ) made it possible to use EDX microanalysis to study the composition of local regions ( $\sim 50\text{\AA}$ ) of thin film samples. A thin film is required to minimize effects such as beam-broadening in the sample, absorption or fluorescence [70]. For NiV and NiMo

samples we found that samples with thicknesses  $<1000\text{\AA}$  obey the thin-film criterion originally adopted by Tixier and Philibert:

$$\mu/\rho)_{\text{Spec.}}^A \csc(a) \rho t < 0.1 \quad (3.15)$$

where  $\mu/\rho)_{\text{Spec.}}^A$  is the mass absorption coefficient of the characteristic x-ray line of material A in the specimen,  $a$  is the angle between the plane of the sample and the axis of the detector,  $\rho$  is the density of the sample, and  $t$  is the thickness of the sample.

When a small volume of the sample is irradiated with an electron beam, electrons are knocked out of deep core levels. In relaxing, the atom emits the characteristic x-ray lines having energies equal to the transitions of electrons from the conduction band to the core levels. An EDX detector (e.g., Lithium-drifted silicon,  $\sim 3\text{-}5\text{mm}$  thick and with area  $\sim 10\text{-}30\text{mm}^2$ ) placed just beneath the sample collects the radiation and converts it into pulses of current proportional to the energies of the incident x-ray photons. These pulses are amplified, digitized and fed into a multichannel analyzer and/or a computer memory. Thus the EDX spectrometer simultaneously displays an entire spectrum in a chosen energy range from 0 to 10, 20, 40 or 80Kev. Figure 3.13 shows an example of such a spectrum.

The energy range 1-10Kev is particularly useful for microanalysis, since it contains  $K_{\alpha}$  lines of elements with atomic number  $Z$  from 11 to 32,  $L_{\alpha}$  lines of  $Z$  from 30 to 80,

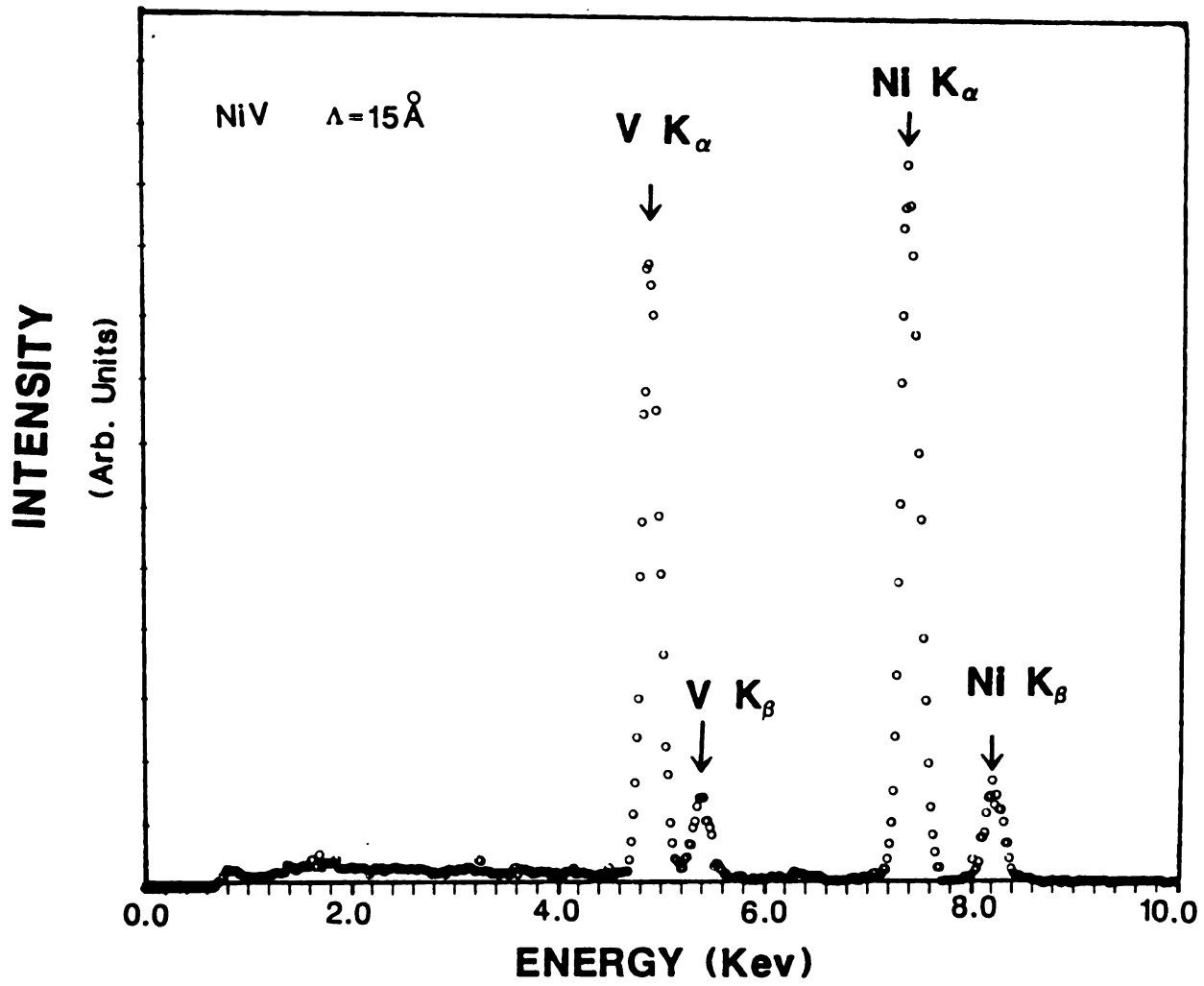


Figure 3.13 EDX Spectrum in a Region of MSU  $15\text{\AA}$  NiV Sample

and M lines of  $Z \geq 62$ .

The x-ray detector is inserted through a side port (using bellows) into the specimen chamber. The detecting crystal and its pre-amplifier should be cooled to liquid Nitrogen temperature to maintain optimum resolution and signal-to-noise ratio. An exposed end of this cooled crystal would quickly become coated with ice and other condensed vapors from the environment; thus a ( $\sim 7.5\mu$ ) beryllium "window" is used to protect this exposed end. The protecting window absorbs x-rays with energy  $< 1$  Kev, so that characteristic x-ray emission lines of materials lighter than Na [71] cannot be detected by such Si (Li) detectors.

### 3.3.1 Theoretical Background [70]

The characteristic x-ray lines of materials in a sample can be obtained in a single scan. The intensity ratio  $I_A/I_B$  of x-ray lines of material A and B can be calculated after subtracting the background contribution to the peaks. The ratio of the mass concentration of the two materials is then given by:

$$\frac{C_A}{C_B} = K_{AB} \frac{I_A}{I_B} \quad (3.16)$$

and

$$K_{AB} = \frac{\epsilon_B K_B}{\epsilon_A K_A} \quad (3.17)$$

where  $K_A$  is the x-ray generation constant of the characteristic x-ray line of material A, and  $\epsilon_A$  is the detector efficiency to that line.

Equation 3.16 is applied to a multilayer structure as follows. The shape of the beam in the film is approximated as cylindrical with a cross sectional area S. The mass of metal A in the irradiated volume is:

$$m_A = t_A S \rho_A \quad (3.18)$$

where  $t_A$  is the total thickness of metal A in the superlattice. Hence, the concentration ratio of metals A and B in the superlattice (which is equal to the mass ratio for our samples with equal layer thicknesses of the two materials) is given by:

$$\frac{C_A}{C_B} = \frac{t_A \rho_A}{t_B \rho_B} \quad (3.19)$$

Combining equations 3.16 and 3.19 gives the thickness ratio of metals A and B as:

$$\frac{t_A}{t_B} = \left[ K_{AB} \frac{\rho_B}{\rho_A} \right] \frac{I_A}{I_B} \quad (3.20)$$

Equation 3.20 shows that the ratio of the thicknesses of the two metals in the superlattice can be determined once the ratio of the integrated intensities of the appropriate characteristic x-ray lines of the two metals is determined. The multiplicative constants are tabulated in reference [70], and the densities of the materials are tabulated in any standard Solid State text [72]. Equation 3.20 can be

reduced to a simple form for Ni/V samples, which relates the thickness ratio of Ni/V to the integrated intensity ratio of their  $K_{\alpha}$  lines:

$$\frac{t_{Ni}}{t_V} = 0.85 \frac{I_{Ni}}{I_V} \quad (3.21)$$

To avoid x-ray absorption in the grid bars, especially when a Cu-folded grid was used, and to maximize the characteristic peak-to-background ratio (e.g., see Zaluzec in ref. [70]), the double-tilt goniometer was used to tilt the sample relative to the detector axis. Since the V line is absorbed more than the Ni line in Cu grid bars, the sample was tilted and measured at intervals of  $<5^{\circ}$  tilt until the maximum ratio of the V line to the Ni line was obtained. The absorption effect in the grid bars was less significant when a one-sided grid was used, so that most measurements were taken at tilt angles  $(-20^{\circ}, +20^{\circ})$  to face the detector. A check was made, however, by measuring around this tilt angle, just to be sure that there were no absorption artifacts. In some cases, we found that the region of the sample under investigation should be tilted  $(-40^{\circ}, +40^{\circ})$  to avoid absorption effects.

Since each piece of a sample of  $\sim 1\text{mm}^2$  area contains  $\sim 10^6 \mu^2$ , it is impractical to measure the composition of the sample at regions separated by  $\sim 1\mu$ . So a measurement was made at the center of each block between the grid bars. Other spots in the same block were measured if any evidence

of unusual behavior was found in that region. Measurements in AREA mode, where a region of the sample  $\sim 5\mu$  across is measured, and measurements using SPOT mode ( $<50\text{\AA}$ ), showed no difference except in a very few regions where different compositions were found.

Figure 3.14 shows the Ni/V thickness ratio obtained from two different pieces (B8 and B9) of the NiV sample with  $\Lambda = 19\text{\AA}$  and total thickness  $\sim 1000\text{\AA}$  grown on rock salt. The horizontal axis represents the index of the block, from which the measurement(s) was (were) obtained. Figure 3.15 shows the topology of piece B9, together with the indices of the measured block. Figure 3.14 shows that, except for few places in the sample, the layer thickness ratio of Ni to V was essentially constant. The average over 25 places on the sample B9 was  $1.14 \pm 0.11$ . Two places in the same block (#1) showed different thickness ratios. One gave a thickness ratio of  $1.5 \pm 0.1$  (i.e., Ni-rich region), and the other of  $1.23 \pm 0.1$ . Measurements as a function of tilt angle indicated that the difference in the thickness ratio in the two measured places was not an artifact of absorption. In the next block (#2), the thickness ratio dropped to  $1.0 \pm 0.1$ .

The piece of the sample in the block labelled (7-21) in Figure 3.15 was measured at five different places. The composition analysis at four different spots showed a thickness ratio of 1.16, consistent with the average across

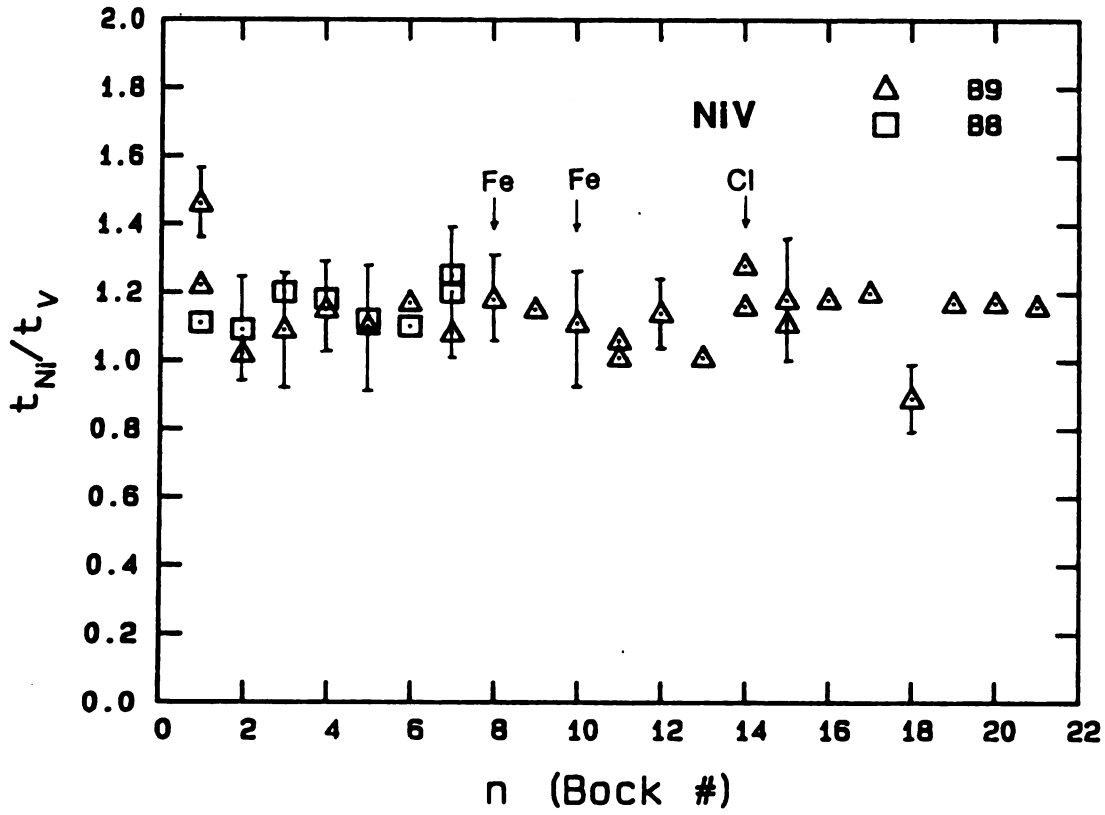


Figure 3.14 Ni-to-V Thickness Ratio in ANL 19Å NiV Superlattice

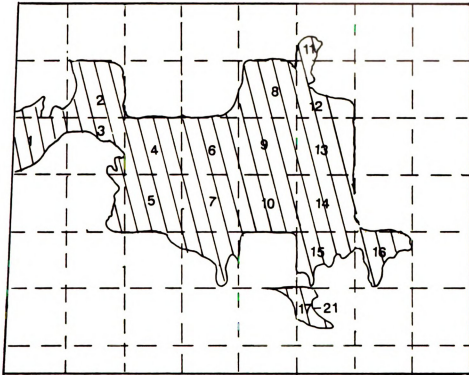


Figure 3.15 Topology of a Measured Piece (B9) of ANL 19Å NiV Superlattice

the sample. At the fifth spot (a dark inclusion), the thickness ratio was 0.9 (i.e., V-rich). More than 50 measurements in that region showed a lower thickness ratio in that inclusion than anywhere else in that region.

Certain regions of the sample contained contaminants such as Fe and Cl. These contaminants can be detected by EDX. Other contaminants, such as O and C, cannot be detected by this technique. Energy Loss Spectroscopy is a useful technique for detecting such low-Z contaminants, as will be discussed later. The Fe contamination found in some regions, such as block #10 was barely detectable. The Cl contamination found in other places was due to undissolved pieces of the NaCl substrate.

Figure 3.14 also shows the thickness ratio for piece B8 of the  $19\text{\AA}$  sample with a total thickness of  $1000\text{\AA}$ . The thickness ratio in seven different regions of the sample showed an essentially uniform composition with an average ratio of  $1.15 \pm 0.1$ , consistent with most measurements in piece B9.

To study the local variations in the composition of samples prepared at MSU, we measured a piece of the  $500\text{\AA}$ -thick,  $27\text{\AA}$  NiV sample (Figure 3.16). Except in one region where the thickness of the film was highly nonuniform, the composition was essentially uniform with an average of  $1.27 \pm 0.06$ . The nonuniform region gave a large variation in the composition at different places. Two

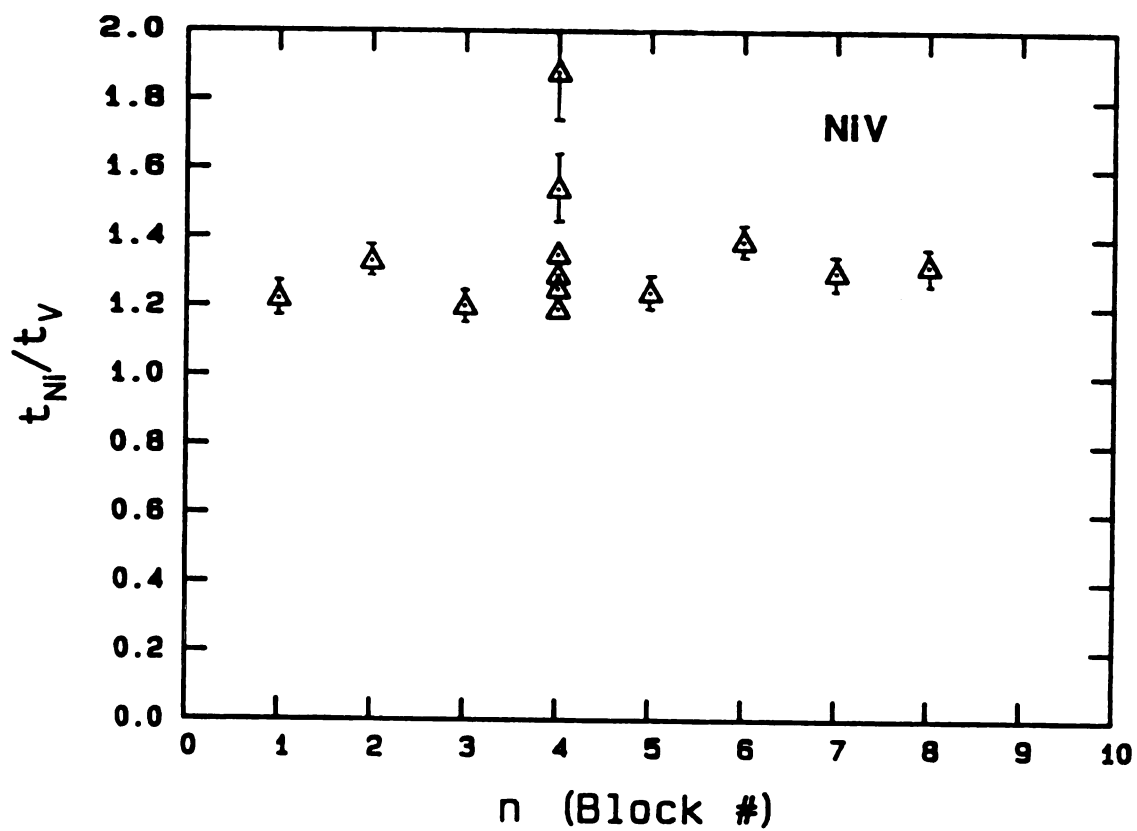


Figure 3.16 Ni-to-V Thickness Ratio in MSU 27Å NiV Superlattice

thick places ( $>500\text{\AA}$ ) gave a Ni/V thickness ratio of  $1.25\pm 0.06$  and  $1.35\pm 0.04$ . Two thin places ( $<500\text{\AA}$ ) gave a thickness ratio of  $1.88\pm 0.13$  and  $1.54\pm 0.09$ . The uniform region of the film in the same block gave a thickness ratio of  $1.19\pm 0.04$ . Absorption effects in the grid bars cannot be responsible for these variations, since we used a Be grid (which is transparent to Ni and V x-ray lines), and a tilt angle of  $(-20^\circ, +20^\circ)$ .

We also measured a  $\sim 1000\text{\AA}$ -thick,  $22\text{\AA}$  NiMo sample prepared at MSU on NaCl. The multiplicative factor for the Mo/Ni thickness ratio in equation 3.21 is 3.3. The composition in 26 different places was  $1.11\pm 0.05$  (Figure 3.17). This sample did not show the large composition variations observed in the MSU NiV sample or in piece B9 of the ANL samples.

Other pieces of other samples, such as the ANL  $15\text{\AA}$  NiV sample of total thickness  $\sim 1\mu$  grown on Mica were studied using x-ray microanalysis. In such samples, however, thin regions along the edge of the sample were studied, so that there is no information about the composition of the interior region of these samples. Besides, the x-ray spectra on such samples were detected using a fixed tilt angle  $(-20^\circ, +20^\circ)$ . The Ni-to-V thickness ratio in the  $15\text{\AA}$  sample was found to oscillate between 0.86 and 1.00 in 16 different places.

For most of the remaining samples, emission EDX was

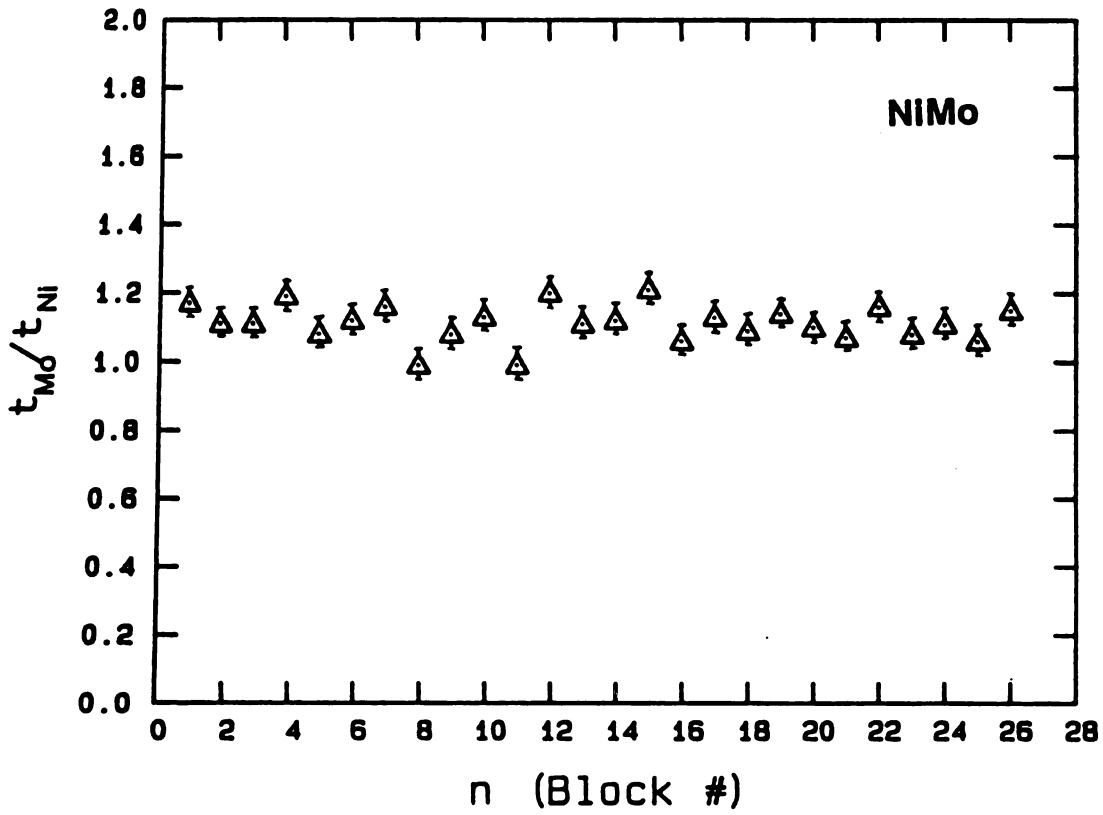


Figure 3.17 Mo-to-Ni Thickness Ratio in MSU 22Å NiMo Superlattice

not used for quantitative purposes, but rather for occasional checking for contaminants or to identify the sample and the regions to be studied by other techniques, such as EELS.

CHAPTER FOUR  
EXPERIMENTAL RESULTS AND ANALYSIS

4.1 Introduction

In this chapter, we first present the characteristic Electron Energy Loss Spectra (EELS) for the pure metals Al, V, Ni and Mo, and compare our data with optical and other EELS data to check the reliability of our measuring techniques and the calibration of the system. Second, we present EELS data on NiV superlattices in the energy range  $<100\text{ev}$ , and then in the higher energy range ( $>500\text{ev}$ ) in the vicinity of both Ni and V  $L_{2,3}$  ( $2p \rightarrow 3d$ ) transitions. We examine how the spectra vary with superlattice period  $\Lambda$ , and compare the intensities of the various lines with those for a NiV "pseudo-alloy" consisting of a superposition of appropriately weighted Ni and V spectra. This study will be presented for samples prepared at ANL. Then we discuss data for NiV superlattices prepared at MSU, and intercompare the data for the two sets of superlattices. Third, we present data in the energy region  $<100\text{ev}$  for NiMo superlattices prepared at ANL, discuss the results, and then compare them with results for NiMo samples prepared at MSU. In NiMo, the Ni  $L_{2,3}$  lines were too weak to be used for quantitative analysis. The Mo  $L_{2,3}$  lines start at  $2520\text{ev}$ , which is above the effective range ( $<2000\text{ev}$ ) of our electron spectrometer.

#### 4.2 EELS of Pure Metals and Oxides

As mentioned in Section 1.1.2, several metals have been found to exhibit plasmons at energies given by the classical free electron plasma energy  $w_p$ . The dielectric function of such metals is given by the classical, free electron model [13]:

$$\epsilon = 1 - \frac{w_p^2}{w(w + ig_0)} \quad (4.1)$$

where  $w_p$  is the free electron plasma energy given by equation 1.1 and  $g_0$  is the damping constant for the plasma oscillation.

Equation 4.1 shows that, for small damping ( $g_0 \ll w_p$ ), the real and imaginary parts of the dielectric function are given by:

$$\epsilon_1(w) = 1 - \frac{w_p^2}{w^2} \quad (4.2.a)$$

$$\epsilon_2(w) = \frac{w_p^2 g_0}{w^3} \quad (4.2.b)$$

This result shows that both  $\epsilon_1$  and  $\epsilon_2$  are smooth functions of  $w$ .  $\epsilon_1$  intersects the  $w$ -axis at  $w_p$ , and  $\epsilon_2$  is very small at  $w_p$ .

The bulk loss function  $\text{Im}\left(\frac{-1}{\epsilon}\right)$  measured in EELS [15] exhibits a peak at  $w_p$ , which has the value  $\frac{w_p}{g_0}$ .  $\text{Im}\left(\frac{-1}{\epsilon+1}\right)$  exhibits a peak at  $\frac{w_p}{2^{1/2}}$ . This is a surface plasmon as predicted by Ritchie [59].

Figure 4.1 shows the optically determined values of

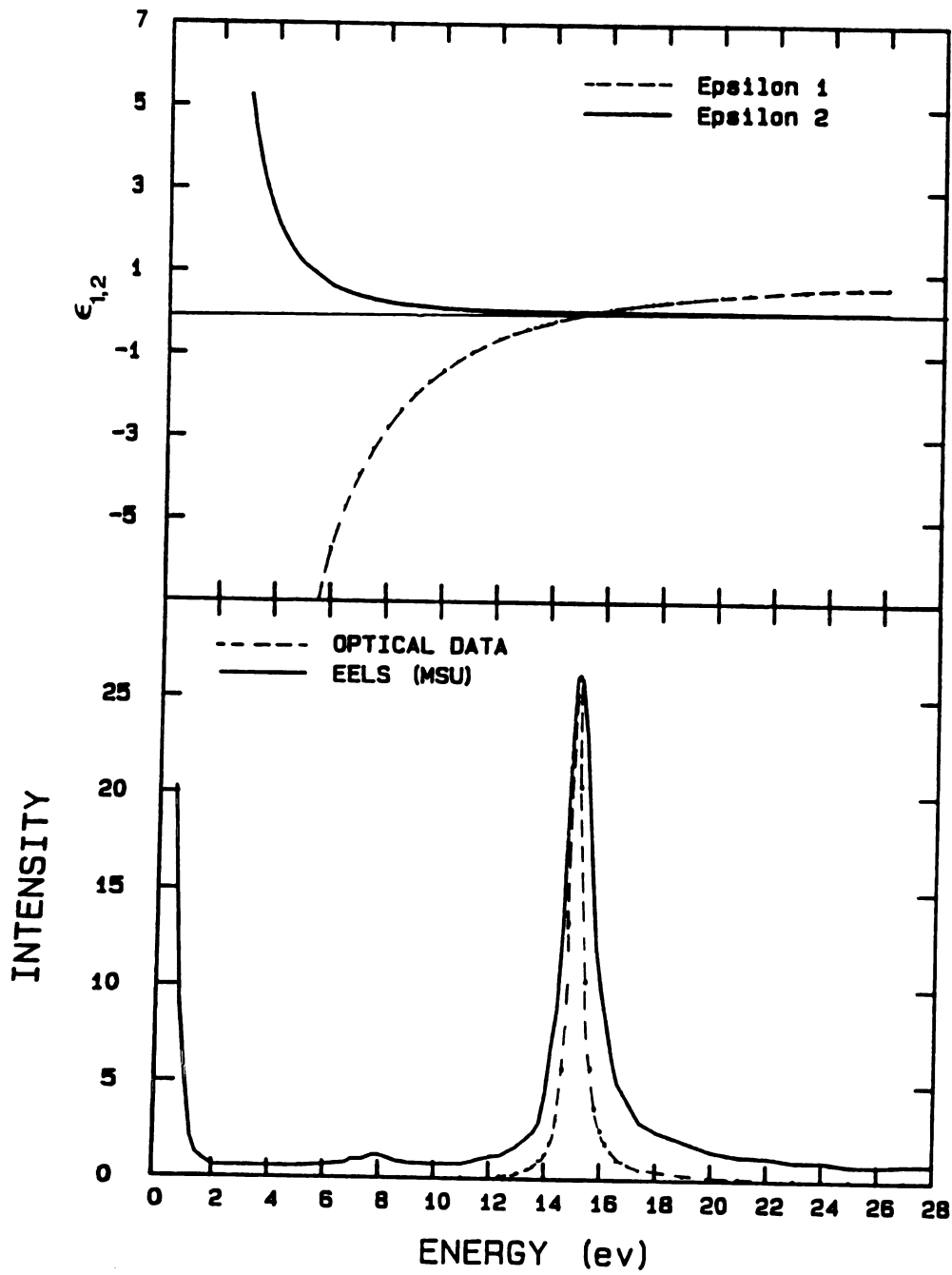


Figure 4.1 Dielectric Function, Loss Function, and EELS of Al

$\epsilon_1$ ,  $\epsilon_2$  and  $\text{Im}(\frac{-1}{\epsilon})$  for Al [73]. These functions are nicely consistent with the free electron dielectric model for Al. Figure 4.1 also shows our EELS measurements for a 400Å-thick Al film, normalized and superimposed on the optical loss function. The Al film was sputtered on a freshly-cleaved NaCl substrate. Our EELS data were not corrected for the energy distribution of the beam (the half width of the electron beam was <1ev). Thus, we notice that the plasmon at ~15.2ev obtained by EELS is somewhat wider than that obtained from the optical measurements. Deconvoluting the primary beam width from our measured spectrum, assuming a Lorentzian line shape for both the plasmon and the primary beam, results in good agreement with the optical measurements. The peak at ~7ev is the surface plasmon of Al, shifted downward due to an oxide layer at the surface [74].

Transition metal EELS spectra are more complicated than many other metals, because of different types of collective excitations that can occur in these metals [44], and because of the onset of interband transitions at low energies. Ksendzov [47] calculated the dielectric function of the 3d metals, taking into consideration the field acting on the core electrons, and obtained a formula for the effective plasma frequency. He suggested that electrons in the 3d transition metal series can be hybridized into bands as follows. In the case of Sc and Ti,

there is one band, giving rise to one plasmon in these metals. In V, Cr, and Mn, there are two bands, the conduction and the first 3d valence bands, giving two plasmons in the loss spectra, one corresponding to the conduction electrons (3 electrons/atom), and the other corresponding to the conduction and valence electrons together. In Fe, Co, Ni and Cu, there are three bands, the conduction band with one electron/atom, and two 3d bands; thus these metals exhibit three different plasmons. The first plasmon corresponds to the conduction electrons (one electron/atom), the second corresponds to the electrons in both the conduction and the second (unfilled) d-band, and the third corresponds to all (4s+3d) electrons in the three bands. Ksendzov compared the results of this analysis with the existing EELS data of the transition metals, and found good agreement. With some reservations, the same argument could be applied to the 4d transition metals, due to the chemical and structural similarities of the 3d and 4d transition metals.

Figure 4.2 shows the optical constants [14] of Mo.  $\epsilon_2$  can be viewed as a monotonically decreasing function, complicated by interband transitions which start below 1ev. Our EELS measurements at regions of the Mo sample with thicknesses  $<500\text{\AA}$  are also shown in Figure 4.2 on the same energy scale as the optical constants. The Mo sample was prepared by jet thinning a 3mm diameter disc, cut from a

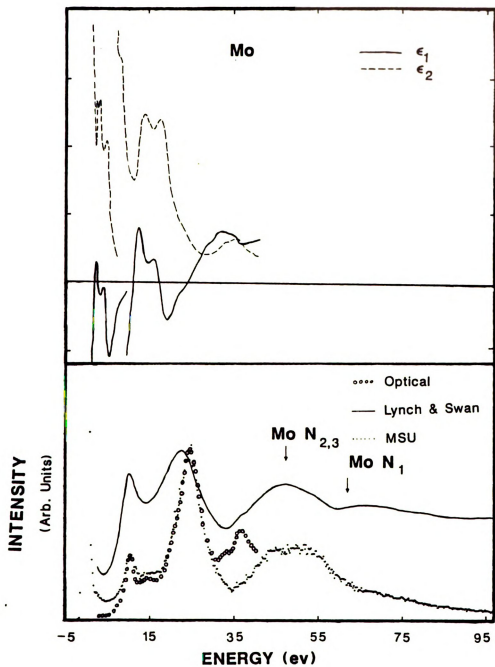


Figure 4.2 Dielectric Function, Loss Function, and EELS of Mo

25 $\mu$ -thick, high purity Mo foil. For jet thinning, we used a solution of 20% H<sub>2</sub>SO<sub>4</sub> and 80% Methanol at 0°C. The loss function, as calculated from the optical constants, and the reflection EELS of Lynch and Swan [40] are also shown in Figure 4.2 for comparison. Our data agree very well with the optical data below 30ev, in both the locations and widths of the loss peaks. The prominent loss in Lynch and Swan's data, however, is about 1.5ev lower. This is probably due to the existence of a surface loss at  $\sim$ 20ev that is comparable in intensity to the prominent loss at  $\sim$ 24.5ev and unresolved from it. The peak at  $\sim$ 10ev in the latter study is higher in intensity than the peak in the optical or our measurements. This can also be explained as due to the higher probability of exciting the surface plasmon [38] at 9.4ev [37] when using reflection EELS. The broad peak centered at 48ev in our data is the 4p (N<sub>2,3</sub>) transition. This peak consists of a large number of multiplets which are unresolved due to solid state band widths and to finite transition lifetime [75]. The peak at  $\sim$ 36ev in the optical data is more pronounced due to a stronger coupling constant in the optical than in the EELS measurements, which results in a stronger multiplet intensity at this energy.

Figure 4.3 shows our EELS data at thin (<500Å) regions around the cracked edges of a pure V film. The film was prepared by sputtering on a Mica substrate, and had a total

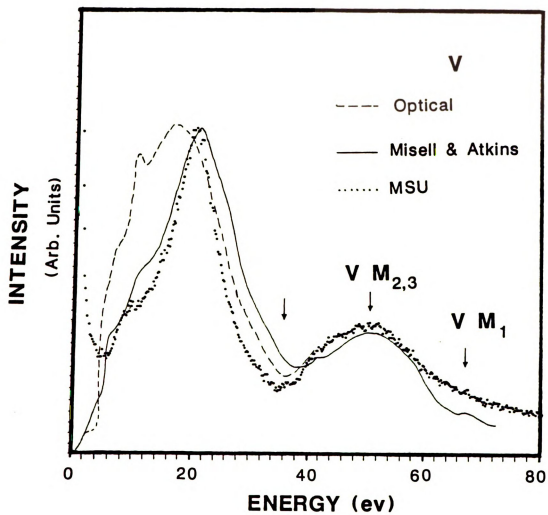


Figure 4.3 Loss Function and EELS of V

thickness of  $\sim 1\mu$ . Figure 4.3 also shows the 60Kev transmission EELS of Misell and Atkins (their films were 250-700 $\text{\AA}$  thick, prepared by evaporation on Mica substrates), and the optical data from reference [14]. Our data agree well with those of Misell and Atkins, so far as the positions of the various peaks are concerned. Our data, however, show a sharper prominent loss and a deeper shoulder at the position of the  $\sim 10\text{ev}$  plasmon. Presumably, the differences are due to differences in the beam energy (60 vs. 100Kev), contamination, and instrumental resolution. The optical measurements do not agree with either measurement, and may have suffered from surface contamination of the sample, as suggested by the authors of ref. [37]. The broad peak centered at  $\sim 48\text{ev}$  is due to the  $3p$  ( $M_{2,3}$ ) transitions. The arrow at  $\sim 37\text{ev}$  in Figure 4.3 marks the threshold of the  $M_{2,3}$  transitions. The arrow at  $\sim 66\text{ev}$  marks the position of the  $3s$  ( $M_1$ ) transition. The  $M_1$  edge was not observed in our measurements, but was observed by Misell and Atkins. This might suggest that they used a larger collector aperture in their measurements, since the nondipolar transitions cannot be observed in transmission with zero momentum transfer. The use of a large collector aperture results in poorer resolution, which might also explain their wider plasmon peaks.

To study the effect of contamination, small pieces of the V film were taken off the substrate and exposed to air

for several days before the time of measurement. The surface contamination of the cracked edges to be studied was thus uncontrolled. A few pieces were introduced into the microscope in a folded Cu-grid. EELS on some places show characteristic spectra that are different from the uncontaminated V spectra below 35ev. The spectra of contaminated V exhibited a peak at  $\sim 12$ ev with intensity comparable to that of the prominent peak at  $\sim 26$ ev peak. High energy EELS scans ( $>500$ ev) showed an oxide core structure at  $\sim 530$ ev in places where the EELS structure differed from that for uncontaminated places on the sample. Our EELS data on contaminated pieces of V film differ considerably from the optical data of Weaver et al [37] in both the shape and positions of the peaks below 35ev. This suggests that the nature of contamination in the two experiments is different. This is not surprising, since the contamination of both samples was uncontrolled and V has several oxides [76]. Figure 4.4 compares EELS spectra on uncontaminated and contaminated regions of the V film.

Figure 4.5 shows our measurements on a  $300\text{\AA}$  Ni film, prepared by sputtering onto a Mica substrate, along with the measurements of Misell and Atkins, and optical measurements from reference [14]. The agreement between our measurements and the others is fairly good below 35ev. The optical data, however, show a sharp peak at  $\sim 10$ ev, which is observed as a shoulder or a slope change in transmission

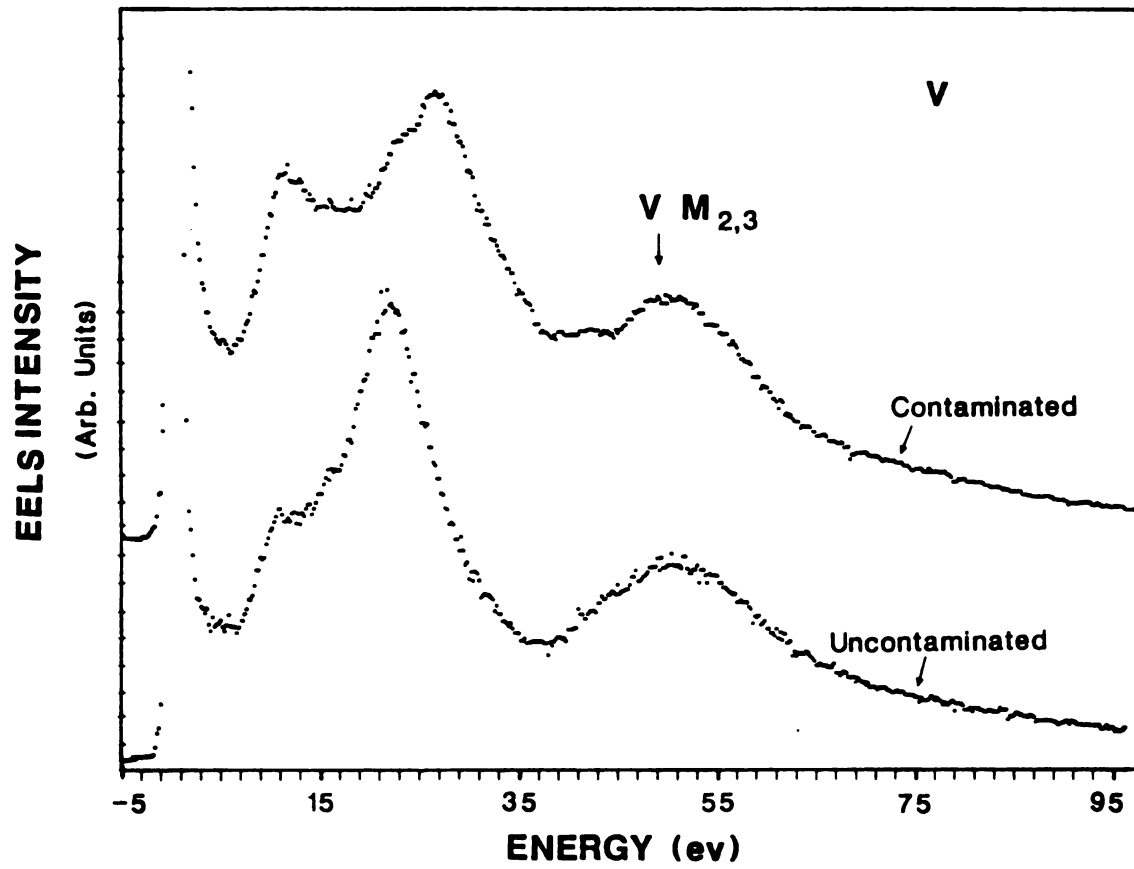


Figure 4.4 Contaminated and Uncontaminated V EELS Spectra

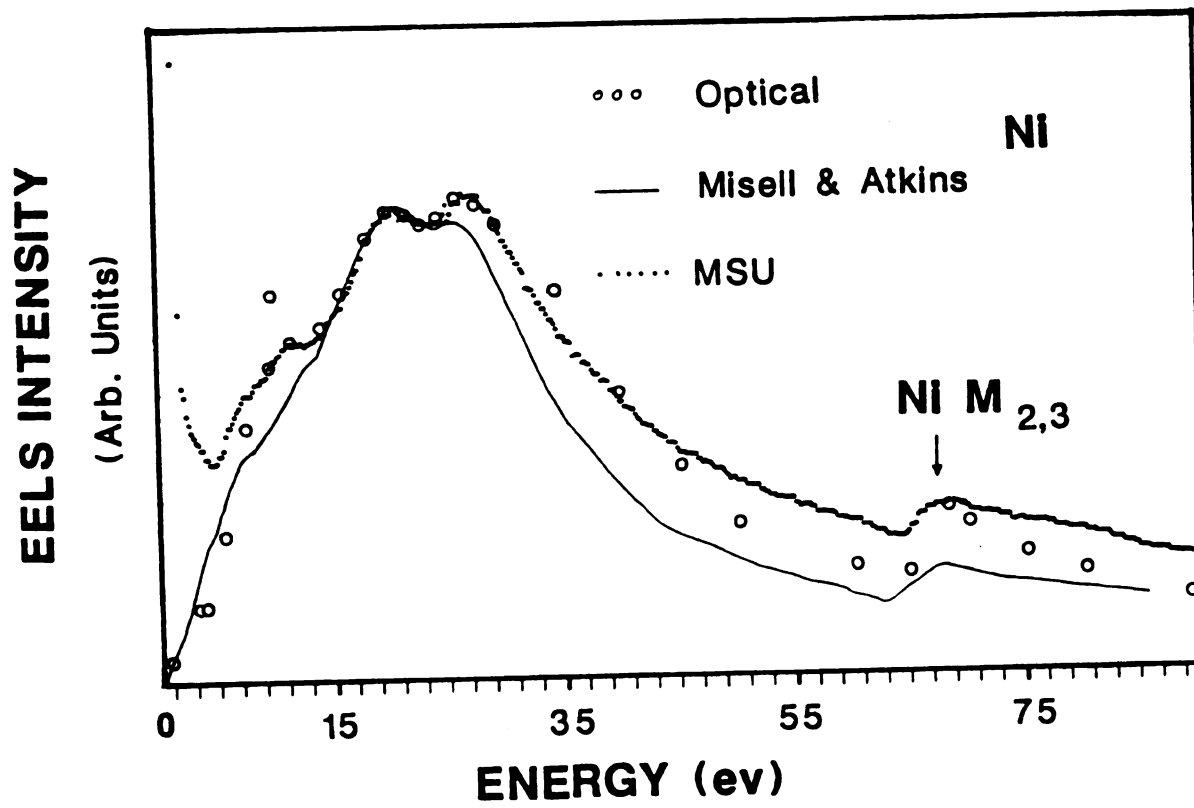


Figure 4.5 Loss Function and EELS of Ni

EELS measurements. The reason for the higher intensity of this feature in the optical data is not clear. The step at  $\sim 67\text{eV}$  is the  $3p (M_{2,3})$  transition.

### 4.3 EELS of NiV Superlattices

EELS measurements were performed in two different energy regions. In the energy region  $< 100\text{eV}$ , the spectra show single particle interband transitions, volume, surface, and, perhaps, interface collective excitations, as well as transitions from  $3p$  shells. In the energy range  $> 200\text{eV}$ , we find the  $L_{2,3}$  transitions of Ni and V, as well as occasional evidence of K-edges of oxygen, carbon, and other contaminants.

#### 4.3.1 The Energy Range $< 100\text{eV}$

In this energy range, several features of interest appear. Volume and surface plasmons, as well as possible interface plasmons, occur at energies  $< 25\text{eV}$ . Interband transitions also occur in this energy range, introducing additional complications to the spectra. Low-lying  $M_{2,3}$  core excitations occur at energies between 35 and 70eV.

The spectra in the core edge region are insensitive to the atomic environment, and hence should be just a simple superposition of the individual metal spectra [77]. In the energy range  $< 35\text{eV}$ , however, we found that the spectra deviated significantly from simple superposition, as will

be discussed in detail later in this chapter.

Several samples prepared in ANL on different substrates were studied. Those samples are listed in Table 4.1.

Table 4.1 NiV Samples Prepared at ANL

Sample #	$\Lambda(\text{\AA})$	Substrate	Total thickness(D)
I	15	Mica	1 $\mu$
II	19	Mica	1 $\mu$
III	19	Mica	1 $\mu$
IV	19	NaCl	1000 $\text{\AA}$
V	19	Mica	1000 $\text{\AA}$
VI	35	Glass	1 $\mu$
VII	40	NaCl	700 $\text{\AA}$
VIII	60	NaCl	750 $\text{\AA}$
IX	80	NaCl	680 $\text{\AA}$
X	80	Mica	1 $\mu$

Our first reliable spectra on NiV superlattices were obtained on a piece of the 19 $\text{\AA}$  sample #IV, which we studied at 13 different places. Ten of these spectra exhibited a peak at  $\sim$ 10-11ev, and three showed only a shoulder or a slope change at  $\sim$ 11-12ev. In eleven of these spectra, the prominent peak position was at  $24.0 \pm 0.4$ ev. Two of the spectra had the prominent loss at 21.6ev, with a peak at 10ev.

One piece of sample #II (a) and two pieces of sample #III (b and c) were studied to check the effect of substrate and total sample thickness on the spectra. Most of the spectra exhibited a peak at  $\sim$ 10-11ev; however, in piece (c) it appeared at  $\sim$ 11.5ev. In piece (a), the position of the prominent loss fluctuated between 21.5 and 23.5ev. In

piece (b), the position of this peak was at  $\sim 24.0 \pm 0.4$  eV. In piece (c), four places were studied. Three of the spectra showed the prominent loss at  $24.0 \pm 0.2$  eV, while the fourth showed the prominent peak at 22.0 eV, and a slope change at  $\sim 11$  eV. A different piece of sample #IV was studied in seven different places. In six places, the spectra exhibited a peak at  $23.5 \pm 0.5$  eV, and a peak at  $10.6 \pm 0.4$  eV. At one place, the spectrum showed a shoulder at  $\sim 11$  eV, and a prominent peak at 23.8 eV. Still a third piece of sample #IV was studied at five different places to further check the results and test for reproducibility. The prominent peak was found to be at  $23.8 \pm 0.6$  eV in all spectra. Four of these five spectra exhibited a peak at  $11.4 \pm 0.4$  eV, while the fifth spectrum showed only a shoulder at 11.6 eV.

The above results from six different pieces of three different samples with period  $19\text{\AA}$  showed that most of the spectra exhibited a peak at  $11.0 \pm 0.8$  eV. The prominent peak in the spectra of five of the six pieces studied was at  $24 \pm 1$  eV. In one piece, however, it seemed questionable whether a simple average usefully defines the position of the prominent peak, since the position did not seem to be centered at any given energy in the range 21.5-23.5 eV. As illustrated in Figure 4.6, the dominant spectra of the  $19\text{\AA}$  NiV superlattices, consisting of 11 and 24 eV peaks, cannot be obtained by a simple superposition of pure Ni and V

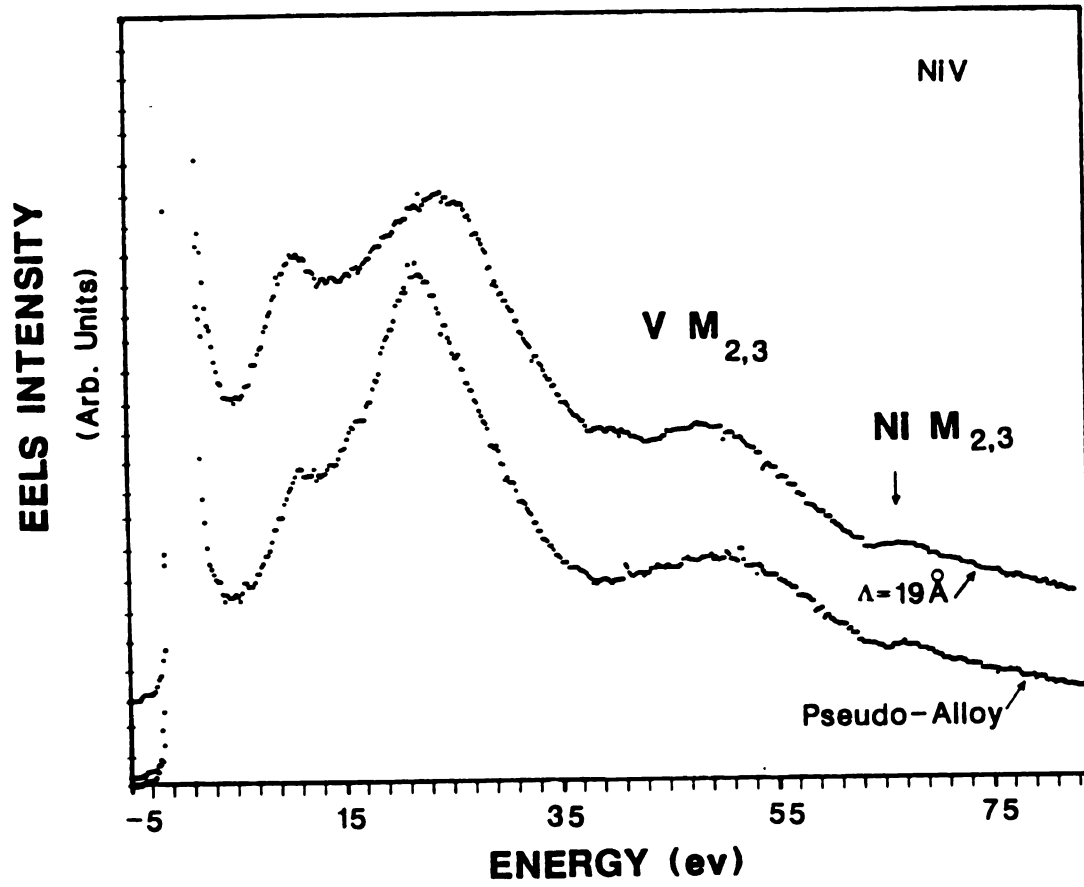


Figure 4.6 EELS of ANL 19Å NiV Superlattice and NiV pseudo-alloy

spectra to form a "pseudo-alloy." The pseudo-alloy spectrum shown in Figure 4.6 was constructed by adding a pure V spectrum to a pure Ni spectrum with intensity at the peak position of half that of the V spectrum. The factor (1/2) was obtained from comparing the values of the loss functions for Ni and V at the peak positions, as evaluated from transmission EELS measurements [46].

Comparison between the characteristic EELS of the 19Å sample and the pseudo-alloy spectrum shown in Figure 4.6 suggests that the growth of the low energy peak and the upward shift of the prominent peak in the 19Å sample might be due to interfaces and/or interactions between the layers. In order to investigate these possibilities further, we studied several other samples with different periods. Figure 4.7 shows typical spectra for all the measured samples from ANL, which we now discuss in more detail.

We started with the 80Å-period sample, which, because of its large  $\Lambda$ , we expected to be most like the pseudo-alloy. Indeed, in a piece of sample #X the loss spectra exhibited a shoulder or a slope change at 11-12eV, and a prominent loss at  $20.5 \pm 1.0$  eV, with a hint of an additional shoulder at ~25-26eV. The loss peak at ~11eV in this sample was considerably lower in intensity than the peak in most of the measurements on the 19Å sample, and much closer to the pseudo-alloy spectrum. The main peak was

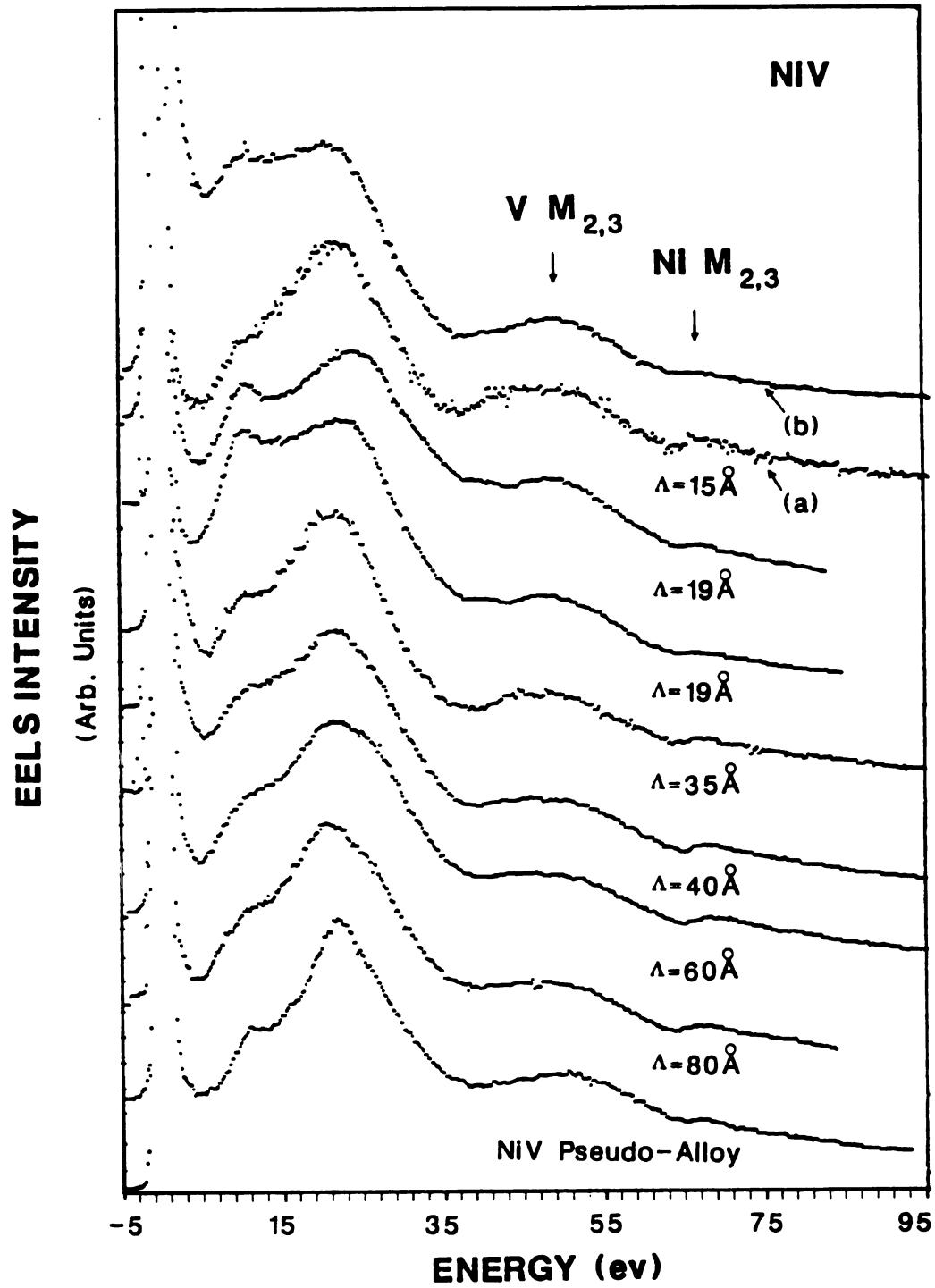


Figure 4.7 EELS of ANL NiV Samples

also at  $\sim 21$ ev like the pseudo-alloy. The shoulder at  $\sim 26$ ev is probably the remnant of the pure Ni 26ev peak which is also noticed in the pseudo-alloy spectrum.

We next investigated a piece of the  $35\text{\AA}$ -period sample #VI, which was taken off the glass substrate. The spectra exhibited a shoulder or a small peak at about  $10.0 \pm 1.0$ ev and a prominent peak at  $\sim 22$ ev. The peak at  $\sim 10$ ev was weaker than that of the  $19\text{\AA}$  sample, but seemed to be stronger than the  $80\text{\AA}$  sample, as indicated in Figure 4.7 by the deeper shoulder of the feature in the  $35\text{\AA}$  sample. To cross-check, another piece of the  $80\text{\AA}$  sample #X was measured, and the results were consistent with the measurements on the first piece.

So far it seemed that the 11ev peak grew in intensity as  $\Lambda$  decreased down to  $19\text{\AA}$ . It seemed a natural step to next measure samples with periods  $< 19\text{\AA}$ . Studying such samples is essential for the interpretation of the observed evolution of the  $\sim 11$ ev peak, and the shift in energy of the prominent peak since, as noted in Section 3.2.1.B, the  $15\text{\AA}$  sample looked amorphous when examined by XRD both by Khan et al. [19] and later by us. Thus, if the observed growth of the  $\sim 10$ ev peak was not due to interfaces, we would expect this peak to be stronger in the  $15\text{\AA}$  sample than in the  $19\text{\AA}$  sample. We would also expect the upward shift in the prominent peak position to increase in the  $15\text{\AA}$  sample if this shift was not related to the structure of the

samples. So, we cracked a small piece of sample #I with  $15\text{\AA}$  period and transferred it to the microscope in a folded Cu grid. EELS data showed a slope change at  $\sim 11-12\text{ev}$  and the prominent peak at  $22.0 \pm 1.0\text{ev}$ . We went back and studied another piece of the  $19\text{\AA}$  sample #IV. The spectra still showed a peak at  $\sim 10.5\text{ev}$ , comparable in intensity to the prominent peak at  $\sim 22.5\text{ev}$ . Then, a different piece of the  $15\text{\AA}$  sample was measured. The spectra were consistent with the previous measurements. At one place, however, out of the 15 places measured in the two pieces, the spectrum showed a peak at  $\sim 11\text{ev}$ , comparable in intensity to the prominent peak at  $21\text{ev}$ . We again went back and studied a different piece of the  $19\text{\AA}$  sample (#III) to make sure that there were no measuring artifacts or other unknown effects. Measurements at four different places on this sample gave a strong peak at  $10.4$  and a prominent loss at  $24\text{ev}$ , consistent with the previous measurements on this sample. No significant contamination effects were observed in any of the above measurements. Thus the evolution of the peak at  $11\text{ev}$  was tentatively attributed to interface plasmons. The interpretation seemed reasonable, since for large  $\Lambda$  samples, the number of interfaces per unit volume is small, so that we expect to find a smaller interface peak relative to the prominent bulk loss peak at  $\sim 21\text{ev}$ . As the period decreases down to  $19\text{\AA}$ , the number of interfaces per unit volume increases, and we expect to have a stronger

interface peak.

The structural properties of the 15Å NiV samples are not yet completely clear. Khan et al. [19] suggested that at such small periods there might be agglomeration in the Ni layers or alloying in the samples. The typical EELS data seem to be consistent with this suggestion, since, in either case, layering of the two metals would not occur, and the EELS data would not be expected to show interface effects. The one spectrum that showed a peak at ~11ev in this sample could then be interpreted as having been acquired from a local region which had reasonable layering.

We later repeated measurements on other pieces of the various ANL samples, and, with an exception noted below, found results consistent with those described above. The largest variations in the data were observed in the 19Å samples. These variations might be attributed to the fact that the sharp transition to an "amorphous" structure occurs just below 19Å, and since this transition occurs within a layer thickness change of about one atomic layer, one would expect to find large local variations in 19Å samples. These variations would "average out" as a coherent structure in the x-ray measurements due to the large beam size, but would appear in local measurements with the small (<50Å) electron beam size used for EELS.

We subsequently measured thin samples (<1000Å) with a wide range of periods that were newly prepared at ANL so as

to provide larger thin areas for EELS measurements. The new samples were #V, VII, VIII, and IX (see Table 4.1). The measurements on these samples gave results consistent with the previous results. The 19Å sample gave a peak at  $10.9 \pm 0.9$  eV and a peak at  $24 \pm 1.1$  eV; the 40Å sample gave a shoulder at  $11.1 \pm 0.3$  eV and a peak at  $22.1 \pm 0.3$  eV; and the 60Å sample gave a shoulder at  $11.4 \pm 0.4$  eV and a peak at  $22.0 \pm 0.6$  eV. Figure 4.7 shows that the intensity of the  $\sim 11$  eV peak grew from a shoulder for large period samples, to a peak comparable in intensity to the prominent peak for 19Å samples. It also shows that the prominent loss peak shifted up to  $\sim 23$ - $24$  eV in the 19Å sample, and back to  $\sim 22.5$  eV for the 15Å sample. The spectrum at one place of the 15Å sample that showed a strong peak at  $\sim 11$  eV had a prominent loss peak at 21 eV.

As noted above, these results suggest that the peak at  $\sim 11$  eV is due to interface plasmons. The source of the shift of the prominent peak is less clear. We initially tentatively attributed this shift to charge transfer between the two metals. To check this possibility, we carried out measurements in the Ni and V  $L_{2,3}$  core regions ( $500 < E < 1000$  eV). In the next section, we will discuss the results in this energy range, and investigate their connections with the data in the low energy range ( $< 100$  eV).

To see how general was the behavior found in ANL NiV samples, we then prepared several samples at MSU. In the

first run, we prepared four samples. The sputtering conditions were set to obtain samples with periods varying from 15 to 30 Å. All of these samples were prepared on freshly-cleaved NaCl substrates, and had a total thickness of about 500 Å. X-ray structural analysis indicated that none of these samples exhibited the long range structural coherence seen in ANL samples having  $\Lambda \geq 19 \text{ Å}$ . All EELS measurements on these samples showed similar characteristic spectra, with a shoulder or a slope change at  $\sim 11-12 \text{ eV}$ , and a prominent peak at  $\sim 22-23 \text{ eV}$ . In the second run, we prepared 500 Å-thick samples on NaCl substrates with periods 20 and 26 Å. X-ray structural analysis of these samples showed long range structural coherence perpendicular to the layers, and the x-ray determined periods were  $\sim 22$  and  $27 \text{ Å}$ , respectively. The characteristic EELS on these samples were indistinguishable from those of the previously measured MSU samples, and of the  $15 \text{ Å}$  sample prepared in ANL, with a shoulder at  $\sim 11 \text{ eV}$ , and a prominent peak at  $\sim 22-23 \text{ eV}$ . In the  $27 \text{ Å}$  sample we observed one  $2 \mu$  size, nonuniform region, as shown in Figure 4.8. EDX analysis at various spots of this region indicated a nonuniform composition across the region. The thin region (the light region in the bright field image) showed a Ni to V ratio of  $\sim 1.9$  (Ni-rich region). EELS data in the energy range  $< 100 \text{ eV}$  in this thin region showed a slope change at  $\sim 11.5 \text{ eV}$  and a prominent peak at  $\sim 24 \text{ eV}$ . Core edge measurements at



Figure 4.8 BF Image of a Nonuniform Region of MSU  $27\text{\AA}$  NiV Superlattice

$\sim 500$ ev showed a clear indication of oxidation of the sample. This last result again shows the lack of correlation between the strength of the peak at about 11ev and oxidation of NiV superlattice samples, since this was the strongest case of oxidation of any sample, and yet we did not observe a strong peak at  $\sim 11$ ev. Further characterization of this thin region of the film using electron diffraction to study the structure parallel to the layers indicated that the region was "amorphous" (as discussed in a previous chapter). Figure 4.9 shows EELS data on various samples prepared at MSU, together with the data of the  $15\text{\AA}$  sample prepared at ANL. These results show clearly that all the spectra have almost identical shape and positions of the loss peaks. The fact that EELS measurements on all the MSU samples were nearly identical suggests that those samples do not support an interface plasmon, maybe due to blurring of the interfaces (as suggested by Miller and Axelrod according to their results on Al-Bi bilayer films).

In view of the differences between the spectra for the samples prepared at MSU and those from ANL, we measured another piece of the  $19\text{\AA}$  sample (#III) at 8 different places to check the variability of the data on different pieces of the sample, and at different times. This time, five of the measured places showed a peak at  $\sim 9$ ev, and the prominent peak at  $\sim 21.5$ ev, and three showed a shoulder at  $\sim 10$ ev and a prominent loss at  $\sim 22$ ev. None showed the peaks

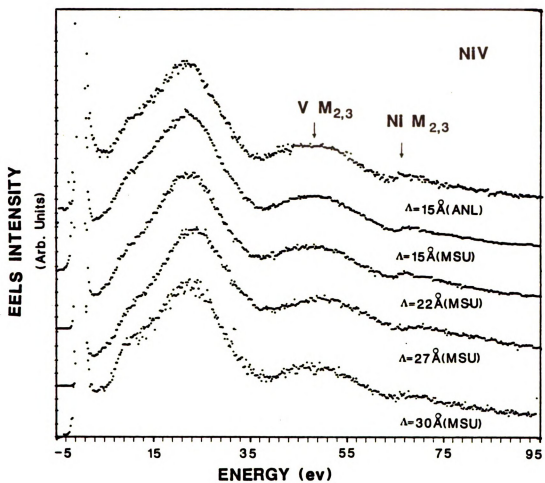


Figure 4.9 EELS of MSU NiV Samples

at 11 and 24ev seen in all previous studies of ANL 19Å samples. Again, there was no correlation between these variations and the contamination or variations in the composition of the sample in the different measured places. The variations in the previously measured 19Å samples could not be correlated to contamination or to composition variations either. All the spectra on the last piece of the 19Å sample showed a shoulder at ~5-6ev that might be assigned to a surface plasmon. This feature was not observed in previous measurements.

To summarize, the dominant behavior of EELS data of NiV superlattices as  $\Lambda$  decreased down to 19Å showed an increase in intensity of the 11ev peak and a shift of the 21ev peak up to 24ev. The 11ev peak was attributed to interface plasmons. The shift of the 21ev peak is not understood. The EELS of "amorphous" samples showed spectra similar to those of the pseudo-alloy. MSU samples showed spectra similar to those of the "amorphous" samples, which suggests that the interfaces are not as sharp as in ANL samples; hence, interface effects do not exist in such samples.

#### 4.3.2 The Energy Range >500ev

In this energy range, long acquisition times are required for a strong signal. Large, thin areas are thus preferred in these measurements, so that most of the

measurements were made on thin ( $<1000\text{\AA}$ ) NiV samples.

In this energy range, EELS has the general form of a smoothly falling "background" which has been found experimentally to satisfy the relation:

$$I(E) = A.E^{-r} \quad (4.3)$$

where  $I(E)$  is the EELS intensity at energy loss  $E$ , and  $A$  and  $r$  are fitting parameters [70]. This background comes from different kinds of excitations, such as valence electron excitations to the vacuum, multiple plasmon losses, and tails of features at lower energies. On this background is superimposed the inner shell transitions. These transitions are used to identify the elements in the sample, since each core edge transition is a unique property of the excited atom. This identification of materials is important, especially in the case of low  $Z$  materials ( $Z < 11$ ) to which regular EDX is insensitive. In addition, study of the edges reveals information about the electronic structure of the materials under investigation [78]. For quantitative analysis of a core edge, it is important to strip the rapidly falling background. Thus, we wrote a program that uses the least-squares method to fit  $\sim 100\text{eV}$  of the pre-edge background, evaluate the parameters  $A$  and  $r$ , and then subtract the intensity given by equation 4.3 from the experimental spectrum. The core edges of transition metals show two sharp lines, called white lines (WL), near the transition threshold [49].

Those lines arise from transitions from  $3P_{3/2}$  ( $L_3$ ) and from  $3P_{1/2}$  ( $L_2$ ) states to the unoccupied part of the 3d or 4d band. The two lines are separated in energy by the spin-orbit splitting of the 2p states which is  $\sim 7\text{ev}$  for V and  $\sim 17\text{ev}$  for Ni. The WLs are superimposed on steps that correspond to transitions from 2p states to the s-band. Thus, the  $L_{2,3}$  transition in Cu, which has a filled d band, is simply a double step as shown in reference [49]. According to the  $(2j+1)$  degeneracy of the initial 2p states, we deduce that the ratio of the  $L_3$  to  $L_2$  transitions should be 2:1, because of the statistical weights of 4 and 2 that the  $P_{3/2}$  and  $P_{1/2}$  states have [55]. This statistical ratio is observed in the case of Cu, but large deviations from this ratio are found in transition metals [49].

To isolate the d-hole contribution to the edge structure, we extrapolated each step back to the peak of the WL, and drew a line perpendicular to the horizontal axis. This procedure is possible in the case of Ni, since the two steps of Ni are observable in the experimental spectrum. For V, we adopted an alternative procedure described just below. The WL intensities as well as the height of the step used in our analysis are shown in Figure 4.10. This analysis procedure was used for simplicity, since comparison between the results obtained in this fashion and results obtained by the more rigorous procedure

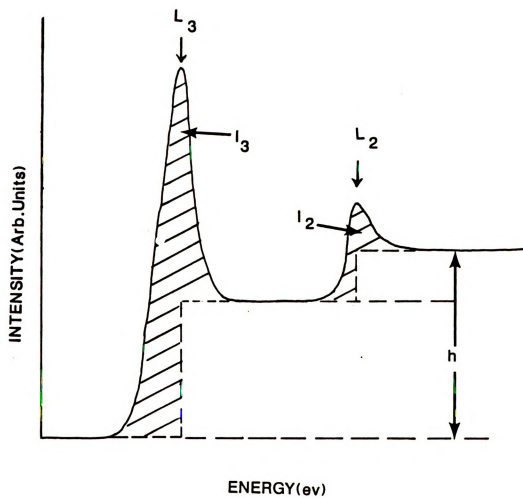


Figure 4.10 Schematic Diagram of  $L_{2,3}$  Core Excitations in a Transition Metal

of assuming an arctangent line shape [79] for the 2p transition to the vacuum showed no significant difference in the intensity analysis of the WLs. The threshold for the transitions to the vacuum (i.e., the step or the inflection point of the arctangent) were aligned with the WL maxima because the Fermi energy position is nearly coincident with the WL peaks [80,81]. For the V spectra, where the two WLs overlap, we estimated the height of the first step by measuring the total height after the WLs, and assuming the statistical ratio 2:1 for the heights of the steps. This assumption is not perfectly accurate, but should be sufficient for our current purposes, since we use the same criterion for analyzing all the V core spectra, and we are interested primarily in differences in the spectra as a function of  $\Lambda$ . The WL intensities were measured relative to the step height after the WLs, as will be briefly discussed in the next section.

We first discuss the V core edge in pure V and NiV superlattices, and then the Ni core edge in pure Ni and NiV superlattices.

#### 4.3.2.A V Core Edge at 513eV

Several spectra were collected for pieces torn off a pure V film of total thickness  $\sim 1\mu$  grown on a Mica substrate. The pieces of the film were transferred into the microscope in a Cu-folded grid within  $\sim 10$  minutes after

tearing, so as to minimize the effect of oxidation at the freshly torn edges to be used for EELS. We also studied pieces of V film that were left at room temperature for several days in order to study the effect of oxidation on the spectra. Then we proceeded to study the superlattices.

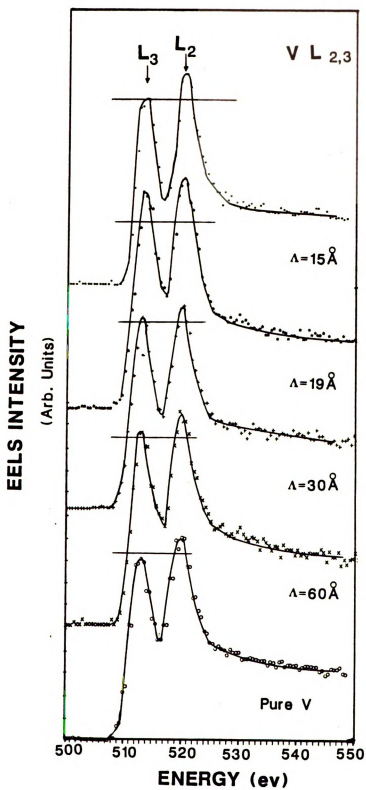
The areas under the WLs were measured using a planimeter. The height (counts/ev) of the step after the WLs (at  $\sim 540$ ev) was used as a standard for the intensities of the WLs. The WL intensity relative to the step height was calculated. The ratio of the intensities of the WLs was found almost constant ( $\sim 1$ ) for all V and NiV samples; hence, in our analysis below, we used the sum of the integrated intensities ( $I_{2,3}=I_2+I_3$ ) of the two WLs normalized to the step height.

For pure, uncontaminated V, the intensity of the WLs was  $13.3 \pm 3.1$ , and the ratio  $I_3/I_2$  was  $1.06 \pm 0.12$ . For contaminated V, the WL intensity was  $14.5 \pm 1.0$  and the ratio was  $1.06 \pm 0.10$ . These results showed that oxidation has little effect ( $\sim 10\%$ ) on the WL intensities, and their ratio. We compared our results with those (intensity of  $11.7 \pm 0.5$ , and ratio of  $1.18 \pm 0.04$ ) obtained from the EELS Atlas [82], and found fair agreement. The data of Fink et al. [53] show a lower intensity ( $9.4 \pm 0.4$ ) and a higher ratio ( $1.37 \pm 0.05$ ) than either our data or that of the atlas. The data of Fink et al. stops at  $< 535$ ev, in which case the measured height of the step might be a little too

high due to the tail of the  $L_2$  WL, which results in a lower intensity and a higher ratio.

To compare the results for a large  $\Lambda$  with those for pure V, we first measured a  $60\text{\AA}$  NiV sample with total thickness  $\sim 700\text{\AA}$ , prepared at ANL. This sample showed a WL intensity of  $17.4 \pm 1.6$ , somewhat larger than for pure V, and a ratio of  $1.01 \pm 0.07$ , in good agreement with pure V. One of the spectra showed a hint of oxygen K-edge structure, and had a WL intensity of  $15.1 \pm 0.8$  and a ratio of  $1.11 \pm 0.04$ , both consistent with the data for contaminated V. New pieces of the ANL  $1000\text{\AA}$ -thick ANL  $19\text{\AA}$  sample grown on NaCl substrate (#IV) were then measured to check for any systematic change with  $\Lambda$ . The core spectra in uncontaminated regions showed a WL intensity of  $21.7 \pm 1.4$  and a ratio of  $0.99 \pm 0.05$ . This suggests a strong dependence of the WL intensities on  $\Lambda$ . In the regions where we found evidence of oxidation, the WL intensity was  $18.1 \pm 2.1$ , and the ratio was  $1.13 \pm 0.16$ . Thus, oxidation cannot be responsible for the increase of the WL intensity from  $\sim 13$  for pure V up to  $\sim 21$  for the  $19\text{\AA}$  sample. As shown in Figures 4.11 and 4.12, the ANL samples show an increase in intensity of the WLs as we decrease the superlattice period down to  $19\text{\AA}$ . The horizontal lines in Figure 4.11 represent a standard peak height to compare the intensities of the different spectra.

Initially two possible effects were considered to

Figure 4.11 L<sub>2,3</sub> Excitations of V

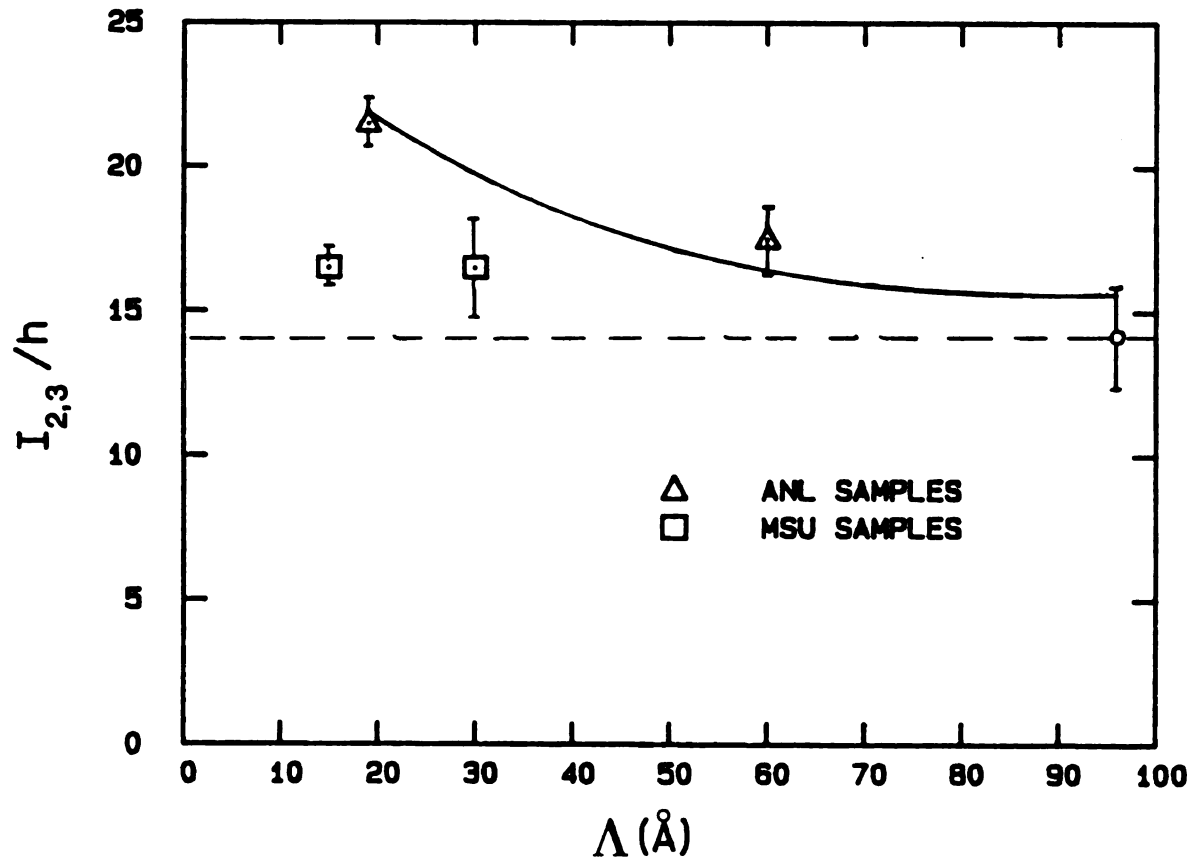


Figure 4.12 Intensities of the V WLs in NiV Samples

interpret the results: (1) interface effects, in which case we expect a smaller WL intensity for the "amorphous" sample with  $\Lambda = 15\text{\AA}$ , and the effect on the Ni WLs is unclear; and (2) charge transfer, in which case we expect a bigger WL intensity for  $\Lambda = 15\text{\AA}$  and also a reduction in the WL intensity of the Ni WLs--which we did not observe, as will be discussed in the next subsection. To see how the WL intensity changed as we crossed the superlattice-"amorphous" boundary, we measured pieces of the 15 and 30 $\text{\AA}$  samples prepared at MSU, neither of which exhibited long range coherence in the x-ray structural analysis. The 15 $\text{\AA}$  sample gave a WL intensity of  $16.4 \pm 1.0$  and a ratio of  $1.14 \pm 0.1$ . The 30 $\text{\AA}$  sample gave an intensity of  $16.2 \pm 2.7$  and a ratio of  $1.09 \pm 0.07$ . The data did not show any clear indication of sample contamination.

To see if the WL behavior of thin 19 $\text{\AA}$  ANL NiV samples was reproduced in thicker samples, we measured several pieces of the  $\sim 1\mu$  thick 19 $\text{\AA}$  sample #III. The data showed an intensity of  $15.4 \pm 2.5$  and a ratio of  $1.04 \pm 0.12$  in the uncontaminated regions, and an intensity of  $17.0 \pm 2.3$  and a ratio of  $0.99 \pm 0.05$  in the contaminated regions. These results show a lower intensity than what we would have expected from the 1000 $\text{\AA}$ -thick, 19 $\text{\AA}$  sample. The data also exhibited large variations in the intensity of the WLs, which extended from that for pure V up to that for the 1000 $\text{\AA}$ -thick, 19 $\text{\AA}$  sample, which might be correlated with

structural nonuniformity of the sample. The pieces of sample #III studied here were also studied in the energy range  $<100\text{ev}$ , and showed a considerably lower peak position than in sample #IV, as discussed in the previous section. So, there seemed to be a correlation between the prominent peak position in the plasmon excitation energy region, and the WL intensity. To investigate this possibility, we went back and analyzed three spectra taken at three different regions of a different piece of sample #III. In the first region, we found a prominent peak at  $22.2\text{ev}$  and a WL intensity of  $14.6\pm 1.0$ , in the second,  $23\text{ev}$  and  $17.3\pm 1.0$ , and in the third,  $24.2\text{ev}$  and  $20.0\pm 1.0$ . In the regions of the  $1000\text{\AA}$ -thick,  $19\text{\AA}$  sample #IV where we obtained spectra for both  $E<100\text{ev}$  and  $E>500\text{ev}$ , we found that most of the measured spectra showed a prominent main loss  $\geq 23.5\text{ev}$ , and a WL intensity  $\sim 20$ . This apparent correlation between the prominent loss position and the WL intensity was only discovered near the end of our studies, and thus was not studied in detail for all measured samples.

To compare the above results with those for samples with long range coherence prepared at MSU, the  $500\text{\AA}$ -thick,  $22\text{\AA}$  and  $27\text{\AA}$  samples were measured. The  $22\text{\AA}$  sample had a WL intensity of  $12.9\pm 1.0$  and a ratio of  $1.13\pm 0.07$ . The  $27\text{\AA}$  sample had a WL intensity of  $12.5\pm 1.0$  and a ratio of  $1.19\pm 0.08$ . The WL intensities of those two samples were similar to those for pure V. The prominent peak positions

of the low loss spectra of those samples were  $\sim 22.5$  eV. These results support the previously noted correlation between the prominent peak position and the intensity of the WLs.

In summary, the intensity of the V WLs increased as  $\Lambda$  decreased down to  $19\text{\AA}$ , and a correlation between the upward shift of the dominant plasmon peak and the WL intensity was observed. MSU samples showed WL intensities close to that for bulk V. These results suggest that the intensity increase of the WLs is an interface effect rather than a charge transfer effect.

#### 4.3.2.B Ni Core Edge at $\sim 850$ eV

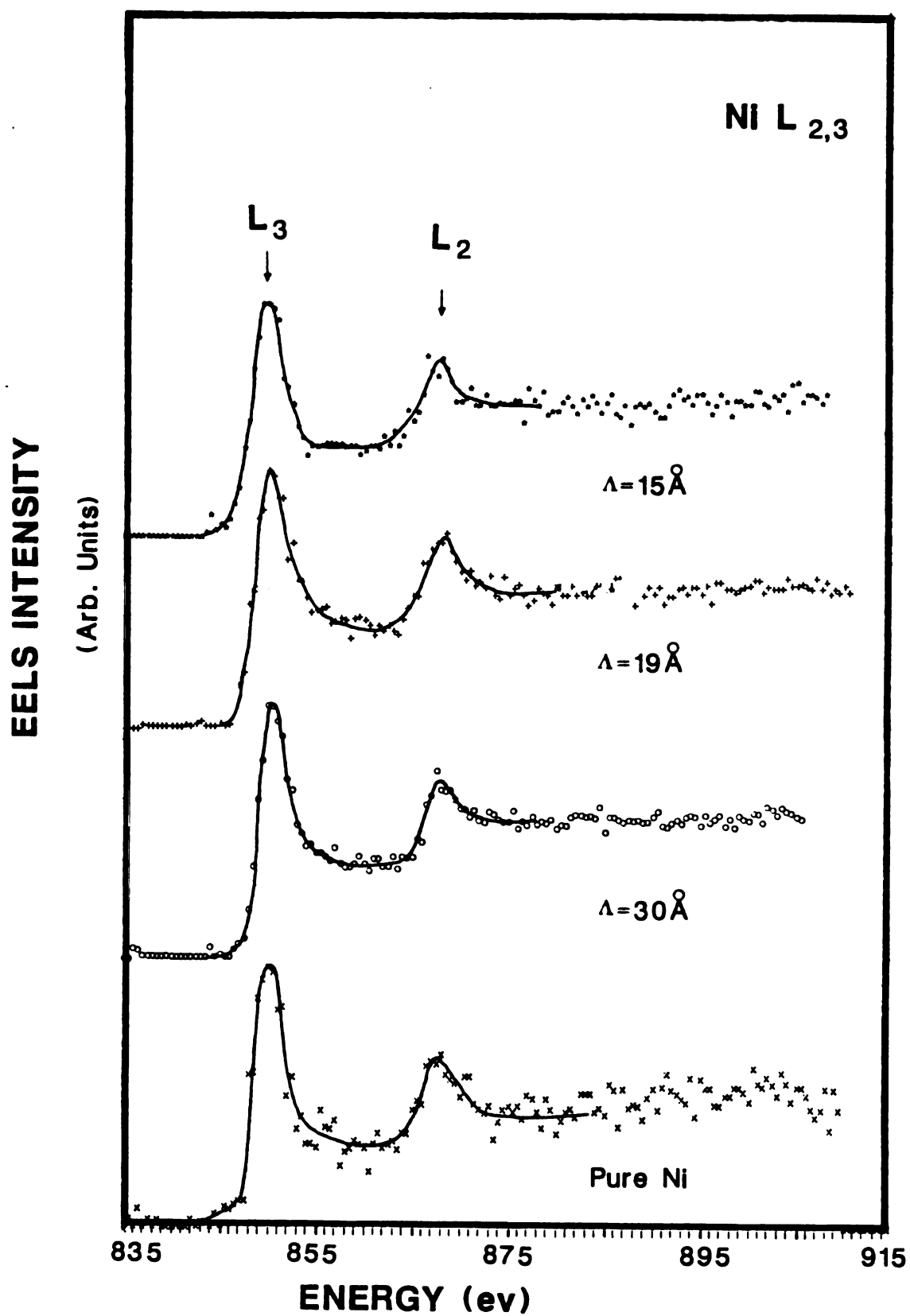
Ni core-edge spectra are weak and require long acquisition times ( $\sim 20$  minutes) to obtain a signal with fairly low noise level. This acquisition time was often unavailable because the electron beam was unstable over such periods of time. Alternative techniques were also employed, such as repeatedly acquiring spectra using shorter acquisition times, and adding them to give a stronger signal. This procedure, however, takes more than an hour to acquire one spectrum with a fairly low noise level, which limits the amount of data that can be acquired in a given working period of time.

Measurements on a pure Ni,  $300\text{\AA}$ -thick film prepared on a NaCl substrate at MSU, and on the cracked edges of a

pure Ni,  $\sim 1\mu$ -thick film grown on Mica at ANL, showed a WL intensity of  $6.5 \pm 0.7$  and a WL ratio of  $3.5 \pm 0.7$ . The data of Fink et al. [53], as analyzed by us, showed an intensity of  $6.0 \pm 0.3$  and a ratio of  $3.9 \pm 0.3$ . We also analyzed the data of Leapman et al. [49] and found an intensity of  $8.4 \pm 0.4$  and a ratio of  $3.6 \pm 0.2$ . These results show that our data agree well with Fink et al., and with the ratio of Leapman et al. The higher WL intensity of Leapman et al. might be due to surface oxidation, since their film was only  $\sim 90\text{\AA}$  thick, and hence, even a thin ( $\sim 10\text{\AA}$ ) oxide layer on the surfaces of the film can have a significant effect on the intensity of the WLs. In contrast, the samples of Fink et al. were  $600\text{-}1000\text{\AA}$  thick, and were prepared under a better vacuum.

We measured superlattices with periods  $19\text{\AA}$  (samples #III and #IV prepared at ANL) and the  $30\text{\AA}$  and  $15\text{\AA}$  samples prepared at MSU. All of these superlattices showed a WL intensity between 6.5 and 8.0, and a ratio  $\sim 3.0$ . Although there were differences in the intensities or ratios from one sample to another, they fell within the uncertainty of the data. Figure 4.13 shows typical Ni spectra of various samples.

If charge transfer occurs from V to Ni layers, the Ni empty d-states would be expected to fill up and hence reduce the WL intensity considerably. No such reduction in the intensity was observed. These results leave the charge

Figure 4.13 L<sub>2,3</sub> Excitations of Ni

transfer model unable to explain all of our experimental results.

#### 4.4 EELS of NiMo Superlattices in the Energy Range <100ev

Since Ni and Mo have essentially the same Pauling electronegativity ( $\sim 1.8$ ) [57], this system was chosen to investigate the relation between the upward shift in energy of the prominent peak in NiV system and the difference in electronegativity (i.e., possible charge transfer) between Ni and V (the electronegativity of V is  $\sim 1.6$ ). Thus, if the shift of the prominent peak was related to charge transfer, we expected no such shift to occur in NiMo system. On the other hand, if the growth of the low loss peak was due to interfaces, we expected such growth in NiMo samples that showed layering in XRD studies.

Several NiMo superlattices were prepared on Mica at ANL. The total thickness of each sample was  $\sim 1\mu$ . The periods of the different samples ranged from  $\Lambda = 14$  to  $110\text{\AA}$ . They thus crossed the superlattice-"amorphous" boundary which occurs somewhere between  $19$  and  $14\text{\AA}$ .

A small piece ( $\sim 1\text{mm}$ ) from the middle of the large  $\Lambda$  ( $110\text{\AA}$ ) sample was measured first. EELS spectra were obtained at twelve different spots around the cracked edges of the sample. The data showed a small peak at  $\sim 10.3 \pm 0.3$  ev, and a prominent peak at  $\sim 24.4 \pm 0.2$  ev (Figure 4.14). The broad Mo  $N_{2,3}$  peak is centered at  $\sim 46$  ev, and the Ni  $M_{2,3}$

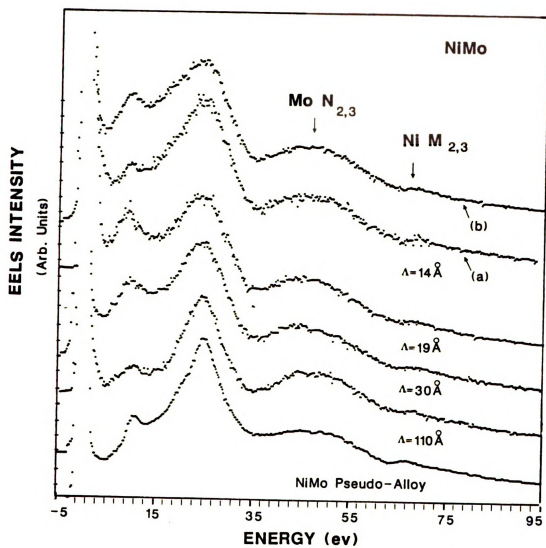


Figure 4.14 EELS of ANL NiMo Samples

step is at  $\sim 66.5$  eV. Figure 4.14 shows that the positions of the peaks as well as the strength of the low energy peak are similar to those of a NiMo pseudo-alloy constructed in a manner similar to that for the NiV pseudo-alloy.

A piece of the  $\Lambda = 19\text{\AA}$  sample was then measured at 9 different places around its edges. The spectra showed a peak at  $9.1 \pm 0.4$  eV which was stronger than the corresponding peak in the pseudo-alloy spectrum, and a prominent peak at  $24.3 \pm 0.1$  eV (Figure 4.14). The position of the prominent peak in the  $19\text{\AA}$  sample was the same as for both the pseudo-alloy and the  $110\text{\AA}$  sample, but the low energy peak was shifted down by  $\sim 1$  eV.

To check an intermediate value of  $\Lambda$ , we measured a piece of the  $\Lambda = 30\text{\AA}$  sample. The data at nine different places around the edges of this piece exhibited a peak at  $9.5 \pm 0.6$  eV and a prominent peak at  $24.3 \pm 0.2$  eV. As shown in Figure 4.14, the relative intensity of the low energy peak for the  $30\text{\AA}$  sample was between those for the  $19$  and  $110\text{\AA}$  samples. A piece of the sample with  $14\text{\AA}$  period, which showed an "amorphous" structure in XRD measurements, was then measured at 17 different places around the edges. At 15 different places we observed a weak shoulder in the EELS spectra at  $9.8 \pm 0.4$  eV and a prominent peak at  $24.4 \pm 0.2$  eV. At two other places, the spectra showed a larger peak at  $9.1 \pm 0.1$  eV, with the prominent peak still at  $24.4 \pm 0.2$  eV. Figure 4.14 contains one spectrum (a) representative of the

15 spectra with only a weak peak or shoulder at 9.8ev, and one (b) of the two spectra that showed a stronger peak at  $\sim 9.1$ ev.

To test the reproducibility of the data, we studied a different piece of the 19Å sample at 25 different places. At 17 of these places, the spectra exhibited a strong peak at  $9.2 \pm 0.7$ ev, and a prominent loss peak at  $24.3 \pm 0.2$ ev. Those two peaks were of comparable heights. The spectra at four places showed a shoulder at  $10.4 \pm 0.4$ ev and a prominent peak at  $24.4 \pm 0.2$ ev. At the remaining four places, the spectra showed a strong peak at  $9.1 \pm 0.3$ ev and a prominent loss at  $23.2 \pm 0.3$ ev. Thus, 84% of the measured spectra showed a peak at about 9.2ev, in excellent agreement with the previous measurements on the first piece of this sample. The downward shift in energy of  $\sim 1$ ev of the prominent peak in 16% of the new measurements had not been observed anywhere in the previously measured samples with the various periods. The appearance of a shoulder at 10.4ev rather than a strong peak in 16% of these measurements was also not observed in the previous measurements on the first piece of this sample. These last spectra are essentially the same as the spectra of the 14Å sample, and are tentatively attributed to intermixing of the two metals in the sample at these places. The statistics, however, show that the majority of the spectra agree very well with previous measurements.

A different piece of the 110Å sample was then measured to cross check the previous results. Measurements on 15 different places showed a small peak at  $10.5 \pm 0.3$  eV and a prominent peak at  $24.5 \pm 0.1$  eV. Those results were in excellent agreement with the previous measurements on this sample.

The above results show the following for the ANL samples:

1) The prominent peak stayed fixed at  $24.4 \pm 0.2$  eV for all superlattices regardless of their periods, except in ~10% of the measurements on the 19Å sample where we observed a ~1 eV downward shift.

2) The low energy peak generally grew in intensity as the period decreased down to 19Å, below which it went back down to an intensity equal to that of the large period sample.

3) The position of the low energy peak shifted from 10.3 eV for the large period sample down to 9.1 eV for the 19Å sample. The position of this peak was ~9.8 eV in those 14Å sample spectra that showed only a small peak or a shoulder, but was 9.1 eV for those spectra that showed a stronger peak.

Although the prominent peak positions in NiV and NiMo systems are consistent with the interpretation of the upward shift in NiV system as due to charge transfer, this model does not explain the fact that in the 15Å NiV sample

the prominent peak went back to the position of that for large period samples.

The growth of the  $\sim 10\text{eV}$  peak as  $\Lambda$  decreased from  $110\text{\AA}$  down to  $19\text{\AA}$  is consistent with this peak being due to interface plasmons, as discussed in conjunction with the NiV data. When we went further down to  $14\text{\AA}$  period, most of the sample regions were not layered, as indicated by the XRD data on this sample. Thus, we did not expect to observe the strong peak at  $\sim 9\text{eV}$ , which we observed in most of the spectra of the  $19\text{\AA}$  sample. The two places on the sample where we observed a stronger peak at  $9.1\text{eV}$  can be thought of as local places where well-defined layers give rise to a stronger low energy peak.

The shift in the low energy peak from  $10.3$  down to  $9.1\text{eV}$  might be due to interface coupling. It could also be, however, that this shift is an artifact of the superposition of the  $\sim 9\text{eV}$  and the  $\sim 24\text{eV}$  peaks. Upon superposition, the tail of the prominent peak pulls the apparent position of the  $9\text{eV}$  peak to higher energies; the stronger is the  $9\text{eV}$  peak is, the smaller is the upward shift in its position.

Since there was a sharp transition in both the EELS and the XRD data in going from  $19\text{\AA}$  to  $14\text{\AA}$  periods, we prepared at MSU samples with periods  $\sim 20\text{\AA}$  and samples with periods  $\sim 14\text{\AA}$  on Mica and NaCl substrates. Each sample had a total thickness of  $\sim 1000\text{\AA}$ . Structural x-ray analysis of

the nominally 20Å samples indicated that they actually had periods of 24Å (for the sample on Mica), and 22Å (for the sample on NaCl). The two samples which were intended to have a period of ~14Å showed an amorphous XRD pattern, as anticipated.

A piece of the 24Å sample on Mica was taken off the substrate and transferred to the microscope in a Cu folded grid. Thin regions (<1000Å thick) around the edges were measured at 10 different places. EELS spectra at six of these places showed a shoulder at  $11.8 \pm 0.2$  eV and a prominent peak at  $24.3 \pm 0.2$  eV. At four places, the spectra showed a strong peak at  $10.8 \pm 0.7$  eV, and a prominent loss at  $24.3 \pm 0.1$  eV. The peak at 10.8 eV was not as strong as those of the 19Å sample prepared in ANL.

We floated a piece of the 22Å sample on water and picked it up on a Ti grid. The sample was measured at six different places. At two of these places we observed a strong peak at  $10.7 \pm 0.2$  eV and a prominent peak at  $24.2 \pm 0.3$  eV. The other four spectra exhibited a small peak or a shoulder at  $11.1 \pm 0.2$  eV and a prominent peak at  $24.8 \pm 0.5$  eV.

From the measurements on pieces of both samples prepared at MSU, we see that the position of the prominent peak is in excellent agreement with the data of the samples prepared in ANL. The position of the low energy peak is, however, considerably higher than that of the previous

measurements.

The results on these two MSU samples showed the following: The position of the low-energy peak in those spectra that showed a strong peak was the same in both samples, while in those spectra that showed a small peak or a shoulder, it was lower in the sample prepared on NaCl than in the sample prepared on Mica. As in the previous measurements, the shoulder (or small peak) positions are higher than those of stronger peaks.

The above data show that all samples prepared at ANL and at MSU exhibited a prominent peak at  $\sim 24$  eV, which suggests that the position of this peak is not affected by the structural properties of the sample. The growth of the low energy peak is strongly correlated with  $\Lambda$  and with the structural coherence of the samples. The shift in the position of the low energy peak is also correlated with the strength of the peak (peaks with higher intensity are lower in energy). The low energy peaks for MSU samples are higher in energy ( $\sim 1$  eV) than those for ANL samples, which means that the downward shift of this peak is sample and structure dependent.

CHAPTER FIVE  
SUMMARY AND CONCLUSION

This thesis consists of characterization of NiMo and NiV superlattices and measurements of their EELS. To characterize the samples, we used three different techniques:

a) EDX to study the local composition of the samples at different places.

b) XRD to study the structural characteristics of the samples perpendicular to the layers.

c) SAD and MD to study the in-plane structural characteristics of the samples.

EELS measurements were carried out in two energy regions:  $<100\text{eV}$  to study bulk, surface, and interface plasmons, and  $>500\text{eV}$  to study core-level excitations.

We studied NiV samples with periods ranging from 15 to  $80\text{\AA}$  prepared at ANL and with periods from 15 to  $30\text{\AA}$  prepared at MSU. We also measured NiMo samples with periods from 14 to  $110\text{\AA}$  prepared at ANL and with periods of  $\sim 20\text{\AA}$  prepared at MSU. In both systems, the samples crossed the superlattice-to-"amorphous" boundary below  $19\text{\AA}$ .

a) EDX generally showed a uniform Ni-to-V or Ni-to-Mo ratio, although occasionally we found variations in the ratio of the two constituents.

b) In agreement with previous work, XRD data showed a

slight expansion in the average d-spacing perpendicular to the layers as  $\Lambda$  decreased down to  $\sim 19\text{\AA}$ , and a sudden contraction for the "amorphous" samples back to the expected bulk value.

c) SAD and MD showed local variations, especially in samples with  $\Lambda$  near the superlattice-"amorphous" boundary.

XRD and electron diffraction measurements on MSU samples showed smaller coherence lengths perpendicular to the layers and smaller crystallite sizes parallel to the planes than for the ANL samples.

EELS data on ANL samples with large  $\Lambda$  were similar to those for a NiV pseudo-alloy, corresponding to an appropriately-weighted sum of spectra for pure Ni and pure V. As  $\Lambda$  decreased to  $\sim 19\text{\AA}$ , three effects were observed in the typical data on ANL samples:

a) An 11ev shoulder in the spectra for large  $\Lambda$  samples developed into a peak which grew with decreasing  $\Lambda$  until it was comparable in height to the main peak located at  $\sim 24\text{ev}$ .

b) The main peak shifted upward from  $\sim 21$  to  $\sim 24\text{ev}$ .

c) The normalized V White Line (WL) intensity increased by about 50%.

The EELS of the  $19\text{\AA}$  samples showed substantial local variations; in some places, instead of the behavior defined above, both the low energy peaks and the WL intensity were similar to those for the pseudo-alloy. EELS

data on the 15Å "amorphous" samples were generally similar to those of the pseudo-alloy; however, in one place the spectra showed a strong peak at ~11ev, just as in the 19Å sample. When both low energy peaks and WLs were measured, a correlation was observed between the upward shift of the position of the prominent plasmon peak and the increase in the V WL intensity. The Ni WL intensity did not show a significant change with  $\Lambda$ .

All the MSU NiV samples had EELS spectra similar to those for the pseudo-alloy, regardless of  $\Lambda$  or whether the sample showed superlattice or "amorphous" x-ray structure.

As in the case of NiV, ANL NiMo samples with large  $\Lambda$  had EELS spectra similar to those of a NiMo pseudo-alloy, with a small peak at ~10ev and a main peak at ~24ev. As  $\Lambda$  decreased down to 19Å, the ~10ev peak typically grew in height and shifted downward to ~9ev. The prominent peak remained fixed at ~24ev. Typical spectra of the 14Å sample were similar to those of the pseudo-alloy. Again, some variations in spectra were observed; at some places in the 19A sample the spectra were similar to the pseudo-alloy, and at a few places in the 14Å sample the spectra were like typical spectra for the 19Å sample.

EELS measurements on MSU NiMo samples of nominal period ~20Å showed no consistent behavior; rather, the spectra were distributed between typical spectra of the ANL 19 and 14Å samples.

In both NiMo and NiV systems, the growth of the  $\sim 10$  eV peak is attributed to excitations of interface plasmons. Although charge transfer provides a potential explanation for the increase in intensity of the V WLs as  $\Lambda$  decreases, and possibly also for the upward shift of the ( $\sim 21$  eV) plasmon peak, it explains neither the fact that the intensity of the Ni WLs did not decrease nor the fact that the prominent peak shifts down when we cross the superlattice-"amorphous" boundary. The downward shift of the  $\sim 10$  eV peak in ANL NiMo samples is attributed to a strong interface plasmon at  $\sim 9$  eV which dominates the original weak plasmon peak in the pseudo-alloy spectrum.

In summary, in going from superlattice to "amorphous", the ANL samples typically show unusual behavior, both in structure and in EELS measurements. The samples with  $\Lambda$  near the superlattice-"amorphous" border show strong local variations from the typical behavior. Those variations are not observed on a macroscopic scale in XRD studies, but are observed in the local studies available in the FE-STEM. Thus we conclude that, on a microscopic scale, the samples with  $\Lambda \sim 20 \text{ \AA}$  are not uniform. The FE-STEM is a powerful tool to probe local variations and nonuniformities in such samples.

NiV samples prepared at MSU did not support interface plasmons, since the spectra of all samples were similar to those of the amorphous ANL sample. Thus, the interfaces of

MSU NiV samples are apparently not as sharp as those from ANL. MSU NiMo samples, on the other hand, showed at different places behavior similar to both the crystalline and amorphous ANL samples, which suggests that MSU NiMo samples have local regions with reasonably sharp interfaces.

APPENDIX

## Appendix A

### The FE-STEM

The Field Emission Scanning Transmission Electron Microscope is an instrument dedicated for near-atomic resolution. In 1971, A.V. Crewe and his collaborators [83] first realized the concept, and later constructed the ultra high vacuum (UHV) instrument, in addition to the electron source. The first instrument was the size of a small suitcase, and was easily evacuated to UHV. To change the sample, however, required that the instrument be taken apart, and hence the instrument was impractical for the study of several samples within a period of a day. The principle of Crewe's microscope is illustrated in Figure A.1.

#### A.1 The VG HB501 FE-STEM [84]

UHV FE-STEMs are now commercially available. The optical column of the Vacuum Generators (VG) model HB501 FE-STEM instrument used in the present work is shown in Figure A.2. This instrument consists of two basic units; (a) the electron optical column; and (b) the electronics console. In this section these two basic units are briefly reviewed; for more details, the reader is referred to the VG Operation manual.

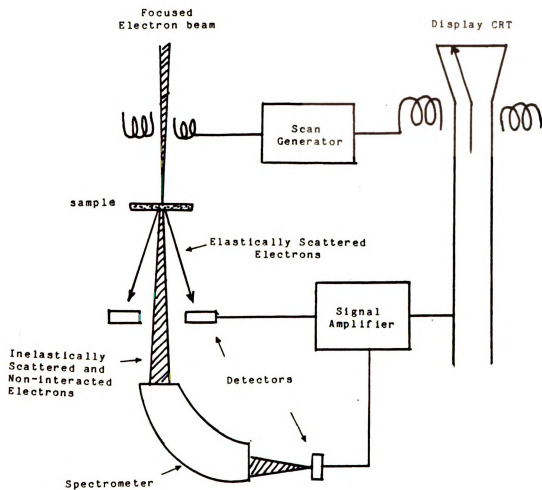


Figure A.1 The Principle of the FE-STEM

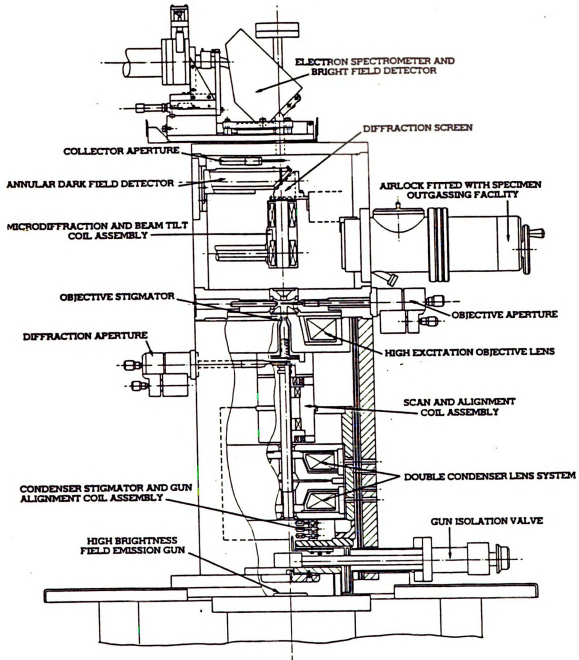


Figure A.2 Schematic Diagram of the Electron Optical Column in the FE-STEM

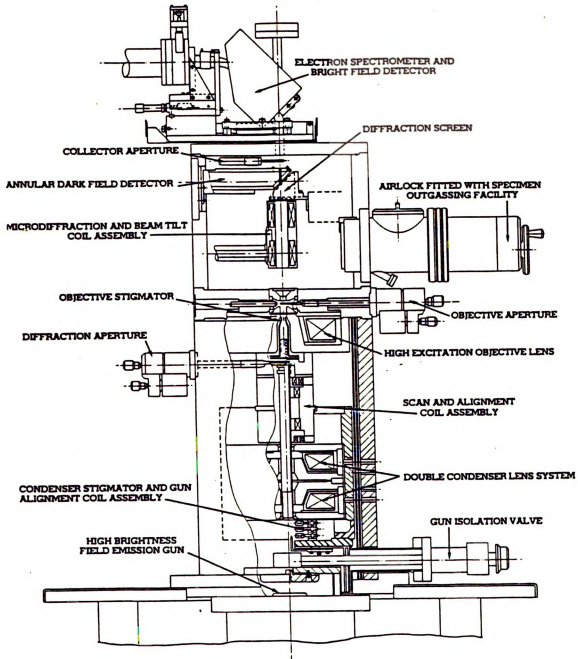


Figure A.2 Schematic Diagram of the Electron Optical Column in the FE-STEM

a. The Electron Optical Column: This contains the electron gun at the bottom, and the apertures, detectors, etc. above it, as shown in Figure A.2. The UHV column consists of two vacuum sections that are pumped using different mechanisms, and can be isolated from each other by means of the gun isolation valve. Those two vacuum sections are (1) the gun chamber, maintained at pressure  $P \sim 10^{-11}$  mbar, and pumped by an ion pump/Ti sublimation pump, and (2) the specimen chamber, maintained at  $P < 10^{-9}$  mbar, and pumped by a diffusion pump/Ti sublimation pump. During operation the Ti sublimation pump is turned off. The diffusion pump is backed by a mechanical pump, and cooled by a liquid Nitrogen trap that also works as a cryopump.

The electron gun consists of a single crystal Tungsten wire sharpened to a tip of curvature  $\sim 1000\text{\AA}$  [18]. It is mounted on a support wire that can be used for occasional cleaning of the tip by passing a short-duration current through it. The field emission current of the tip can be monitored by applying an appropriate voltage between the tip and the first "extraction" anode. This voltage is typically  $< 4.5\text{KV}$ , and can give a source brightness up to  $10^9 \text{Amp./cm}^2$  steradian. A second anode accelerates the electrons. The voltage between the tip and the second anode can be varied either continuously from 5-30KV, or from 20-100KV in steps of 20KV. Since the real emitting

region of the tip is  $\sim 100\text{\AA}$ , this gun assembly can produce an electron beam of  $250\text{\AA}$  in diameter.

The beam size can be further reduced to  $<5\text{\AA}$  using the double condenser lens system,  $C_1$  and  $C_2$ . Those two electromagnetic lenses are external to the vacuum, and are water-cooled. In selected area diffraction mode, they are used to focus the diffraction pattern. In the low magnification mode, they are used to focus the beam on the sample.

The third lens is a high excitation objective lens. It is partially inside the vacuum, and is water-cooled. It is used to focus the beam on the sample in the normal imaging mode.

The imperfect axial symmetry of the magnetic lenses give rise to astigmatism [70]. Hence, stigmators are needed for high resolution imaging. In the FE-STEM there are two octopole stigmators. The gun stigmator is an 8-pole electromagnetic stigmator used for stigmating the gun/condenser system. This stigmator is important in low magnification and in selected area diffraction mode. The objective stigmator is an 8-pole electrostatic stigmator used to correct astigmatism in the objective lens region. This is important for high resolution imaging.

The electron beam can be scanned before it strikes the sample. The scanning assembly coils produce a double deflection of the electron beam that permits the scanned beam to be rocked about the objective aperture in the

imaging mode, or about the selected area diffraction (SAD) aperture in the SAD mode. These coils are situated between the objective and the condenser lenses, and are external to the vacuum. The beam can also be scanned after it leaves the sample, using the microdiffraction (Grigson) scan coils situated above the sample stage. This coil assembly consists of two sets of double deflection coils. One is used to produce the microdiffraction pattern, and the other to align the bright field image. The coil assembly is bellowssealed, and must be taken out during specimen changing.

Four different sets of apertures are fitted to the column. Each aperture mechanism is a bellows-sealed mechanism with micrometer adjustment for fine control of the aperture position in the horizontal plane. The positions of three of these mechanisms are shown in Figure A.2. The diffraction aperture is used to define an area on the sample from which a Selected Area Diffraction (SAD) pattern is obtained. The smallest area that can be measured is  $\sim 0.3\mu$ , achieved with a  $10\mu$  aperture. Larger areas can be measured using 50, 100, or  $250\mu$  apertures. The objective aperture defines the convergence angle of the beam onto the specimen in normal imaging, or in the microdiffraction mode. A combination of sizes of this aperture and the detector (collector) aperture defines the resolution in these two modes. The smallest size of the

objective aperture ( $\sim 10\mu$ ) is needed to obtain a high resolution microdiffraction pattern. In the normal imaging mode, the  $100\mu$  objective aperture is used. When collecting energy loss spectra in the core region ( $E \geq 500\text{ev}$ ), the signal is weak, and a high intensity signal is needed. In this case, a large ( $>100\mu$ ) objective aperture is required, in addition to a large ( $>1\text{mm}$ ) collector aperture. This choice, however, results in loss of energy resolution in the energy loss spectra.

The collector aperture defines the acceptance angle of the electron spectrometer. Small apertures are used for high resolution signals.

The virtual objective aperture (VOA) is optically conjugate to the objective aperture, and is situated between the electron gun and the double condenser lens system. Together with the SAD aperture, it is used instead of the real objective aperture for x-ray microanalysis. This eliminates the huge Cu x-ray line coming from the OA blade after being illuminated by stray electrons. On top of the column a  $90^\circ$  magnetic sector electron spectrometer is fitted. This is suitable for the study of energy losses up to  $2\text{Kev}$ . The exit slit width is adjustable by means of a bellows-sealed micrometer drive. The spectrometer entrance angle is defined by the collector aperture size. The spectrometer output is detected by the bright field detector. The energy resolution is defined by

the collector aperture and the slit width.

The bright field detector consists of a scintillator/photomultiplier/pre-amplifier assembly situated just after the exit slit of the spectrometer. It collects the electrons after being analyzed by the spectrometer, and hence provides the video signal for the bright field image, energy loss spectra, selected area, and microdiffraction.

The annular dark field detector consists of a scintillator and a light guide inside the vacuum, and a photomultiplier/preamplifier assembly external to the vacuum. It has a hole in it so that the forward scattered beam with scattering angle  $<40\text{mrad}$ . will pass through. The annular dark field detector collects electrons suffering large angle elastic scattering (i.e., Bragg reflection from crystal planes).

An energy dispersive x-ray (EDX) spectrometer is fitted for microanalysis. The detector is Lithium-drifted Silicon (SiLi). It is continuously maintained at liquid Nitrogen temperature, since appreciable periods of warm-up result in changing the detector characteristics [85].

Specimens are loaded into the top entry stage by means of an air lock, which can be isolated from the specimen chamber and pumped using the roughing and then the diffusion pump. A cold stage is fitted to pass cold Nitrogen gas to the specimen area, lowering the specimen temperature to about 150K. This is essential to minimize the migration

of surface contaminants to the spot being measured.

b. The Electronics Console: This console is modular in design, and in many cases can be controlled externally by computer. It contains the necessary control and display modules. Mechanical shift and tilt controls are located in the desk top attached to the console. These controls are necessary for moving from one region to another on the sample while measuring, and also for diffraction studies. There are three monitors in the console. Two are normally used for bright-field and dark-field emission, and the third is used with a polaroid camera to take pictures of images or diffraction patterns or energy loss spectra from the monitor screen directly. In the remaining part of this section, some functions in the electronics console are discussed. For further details, the reader is referred to the VG Microscope operation manual [84].

1. The Time Base Module: This unit generates smooth line and frame scan wave forms. It controls both the electron beam in the column and the displays. Line and frame speeds are controlled by front panel switches. TV rate scanning may be selected by a pushbutton control. The following modes are controlled by this module:

LOCATE: This facility provides a square spot marker on all three monitors. Its position in AREA mode determines the position of the beam in the SPOT and SPECTRUM modes, and the Y-position of a line scan in LINE mode. The LOCATE

is selected by means of a push-button, and the position of the marker is varied using front panel X and Y dials.

AREA scan: At all available speeds, this is used in imaging and diffraction modes.

LINE scan: A single horizontal line is scanned with the video signal producing a vertical deflection on the displays in a manner similar to the function of a micro-densitometer. The speed of the line scan is determined by the frame speed, and the position by the Y-position of the LOCATE marker. This feature is important for electron diffraction analysis in cases where the crystallites are small and the diffraction rings (in polycrystalline materials) are not very sharp. Thus, locating the LOCATE marker at the central spot and going to LINE scan mode using the push-button control produces a set of peaks surrounding an intense central peak (as will be discussed later).

SPECTRUM: The beam is static on the specimen, but a line scan drives the displays. This line scan is usually used to scan the output of the bright field detector, and the resulting video signal is used to produce a vertical deflection of the line on the display. This mode is used to optimize the control settings for energy loss measurements, and thus, an energy loss spectrum from the region of the sample marked by the LOCATE spot is displayed on the monitor screen being used for bright field signal

det

pos

mea

bea

the

sig

the

to

the

ic

ext

cor

cor

pus

cor

by

pu

co

fo

th

ob

pi

detection.

SPOT: The beam is static on the specimen at the position of the LOCATE marker. This mode is used for measuring regions of the sample as small as the size of the beam.

REDUCED AREA: This reduces the area scanned on both the sample and the displays. This mode gives an improved signal/noise ratio. It is also used to measure parts of the sample displayed on the monitor.

RECORD: The two (left and right) RECORD push-buttons to the left of the monitor screens select which image on the monitors is simultaneously displayed on the photographic monitor. The display and beam scans can be driven by external analog or digital scan wave forms.

2. Magnification-Diffraction Module: This module contains two identical and independent magnification controls for normal imaging. Those may be selected by the push-buttons  $M_1$  and  $M_2$ . The push-button SA selects the condenser lenses for SAD. The camera length [18] is varied by switched and continuous fine controls. The MICRO push-button selects the microdiffraction mode. The condenser lenses settings in this mode are similar to those for normal imaging. The ROTATION dial continuously rotates the scan on the sample through  $360^\circ$ ; this allows the observation of image at any angle. It also allows the pick-up of asymmetry in the ring diffraction pattern when

the

two

ana

si

co

en

er

ra

s

c

e

<

the visually more clear line scan is used.

3. Alignment and Shift Module: This module contains two basic units; viz., the alignment controls and the analog spectrometer controls.

Alignment: This unit drives the alignment coils situated in the scan coil assembly. They are used for co-aligning the optical axes of the gun and objective lens.

Energy analyzer: This unit controls the current in the energy loss spectrometer.

SCAN WIDTH Switch: It controls the energy range of the energy loss spectrum. A push-button allows the OFFSET facility, which enables one to acquire a spectrum that starts at a certain energy that can be chosen using dial controls. This feature is essential for acquiring core edge spectra with reasonable resolution where a scan width  $<250\text{ev}$  is selected in the core edge region.

4. Lens Stabilizer Module: This unit provides front panel controls for the three lenses and the two stigmators. Pushbutton controls are used to switch the lenses and stigmators on and off. Dial controls are used to obtain high accuracy settings for the lenses and the stigmators. Fine tuning of these dial controls is the determining factor in obtaining high resolution images and diffraction patterns.

a

1

v

i

c

.

.

.

.

.

.

.

.

.

.

.

.

.

.

.

.

.

.

## REFERENCES

- [1] K. Behrndt in Techniques of Materials Preparation and Handling, R. Bunshah, ed., (Interscience, New York, 1968).
- [2] I. Schuller, and C. Falco in VLSI Electronics, vol. 4, in Einsbruch, ed., (Academic Press, New York, 1982).
- [3] Molecular Beam Epitaxy and Heterostructures, L. Chang and K. Ploog, eds., (Martinus Nijhoff, Dordrecht, 1985).
- [4] J. Kwo, M. Gyorgy, D. McWhan, M. Hong, F. Di Salvo, C. Vettier, and J. Bower, Phys. Rev. Lett., 55, 1402, (1985).
- [5] I. Schuller, and M. Grimsditch, J. Appl. Phys., 55, 2491 (1984).
- [6] E. Gyorgy, J. Dillon, D. McWhan, L. Rupp, Jr., L. Testardi, and P. Flanders, Phys. Rev. Lett., 45, 57 (1980).
- [7] C. Chun, G. Zheng, J. Vicent, and I. Schuller, Phys. Rev. B, 29, 4915 (1984).
- [8] E. Spiller, App. Opt., 15, 2333 (1976).
- [9] T. Barbee, in Low Energy X-Ray Diagnosis, D. Attwood, and B. Henke, eds., 57, 131, (AIP, New York, 1981).
- [10] A. Saxena, and B. Schoenborn, Acta Cryst., A33, 805 (1977).

Con

dev

Rev

Me

da

Op

Tr

60

7

M

[11] S. Ruggiero, Proceedings of the International Conference on Superlattices, Microstructures, and Micro-devices, Champaign, IL (1984), and refs. therein.

[12] H. Ehrenreich, H. Philipp and D. Olechna, Phys. Rev., 131, 2469 (1963).

[13] Optical Properties and Electronic Structure of Metals and Alloys, F. Abeles, ed., (North-Holland, Amsterdam, 1966).

[14] J. Weaver, C. Krafka, D. Lynch, and E. Koch, Optical Properties of Metals, part I (1981).

[15] H. Raether, Excitation of Plasmons and Interband Transitions by Electrons, (Springer-Verlag, Berlin, 1980).

[16] T. Chen, E. Wolf, A. Giorgi, Phys. Rev. B, 29, 6036 (1984).

[17] J. Weaver, D. Lynch, and C. Olson, Phys. Rev. B, 7, 4311 (1973).

[18] I. Watt, The Principles and Practice of Electron Microscopy, (Cambridge Univ. Press, Cambridge, 1985).

[19] M. Khan, C. Chun, G. Felcher, M. Grimsditch, A. Kueny, C. Falco, and I. Schuller, Phys. Rev. B, 27, 7186 (1982).

[20] H. Homma, Y. Lepetre, J. Murduck, I. Schuller, and C. Majkrzak, SPIE Proc., 563, 150 (1985).

[21] D. Pines, and D. Bohm, Phys. Rev., 85, 625 (1951).

(19

Pr

Ph

B

(

3

- [22] D. Pines, and D. Bohm, Phys. Rev., 85, 338 (1952).
- [23] D. Pines, in Solid State Physics, (Academic Press, Inc., New York, 1955).
- [24] R. Ferrell, Phys. Rev., 101, 554 (1956).
- [25] D. Gabor, Phil. Mag., 1, 1 (1956).
- [26] V. Ageev, L. Belabanova, and M. Bredov, Sov. Phys.-Sol. St., 2, 2578 (1961), and refs. therein.
- [27] J. Swan, Phys. Rev., 135, A1467 (1964).
- [28] O. Sueoka, J. Phys. Soc. Japan, 20, 2203 (1965).
- [29] D. Pines, Elementary Excitations in Solids, (W. Benjamin, Inc., New York, 1964).
- [30] E. Stern, and R. Ferrell, Phys. Rev., 120, 130 (1960).
- [31] W. Miller, Jr., and N. Axelrod, Sol. St. Comm., 3, 133 (1965).
- [32] G. Kovacs, and G. Scott, Phys. Rev. B, 16, 1297 (1977).
- [33] L. Brillson, Phys. Rev. Lett., 38, 245 (1977).
- [34] T. Lopez-Rios, F. Abeles, and G. Vuye, J. Physique, 39, 645 (1978).
- [35] P. Jewsbury, and P. Summerside, J. Phys. F: Met. Phys., 10, 645 (1980).
- [36] P. Summerside, J. Phys. F: Met. Phys., 9, 1643 (1979).

(

R

(

(

1

1

1

1

1

1

1

1

- [37] J. Weaver, D. Lynch, and C. Olson, Phys. Rev. B, 10, 501 (1974).
- [38] R. Vehse, and E. Arakawa, Phys. Rev., 180, 695 (1969).
- [39] L. Feldkamp, M. Stearns, and S. Shinozaki, Phys. Rev. B, 20, 1310 (1979), and refs. therein.
- [40] M. Lynch, and J. Swan, Aust. J. Phys., 21, 811 (1968).
- [41] D. Misell, and A. Atkins, Phil. Mag., 27, 95 (1973).
- [42] W. Simmons, and E. Scheidner, J. Appl. Phys., 43, 693 (1972).
- [43] H. Kolodziej, J. Wesolowski, and B. Rozenfeld, Acta Physica Polonica, A47, 751 (1975).
- [44] M. Krsunskii, Ya. Genkin, and V. Zavodinskii, Sov. Phys.-Sol. St., 12, 2463 (1971).
- [45] H. Kolodziej, J. Olesik, and U. Madalkiewicz, Acta Physica Polonica, A59, 443 (1981).
- [46] C. Wehenkel, and B. Gauthe, Phys. Stat. Sol. (b), 64, 515 (1974).
- [47] Ya. Ksendzov, Phys. Stat. Sol. (b), 93, 415 (1979).
- [48] A. Bearden, and A. Burr, Rev. Mod. Phys., 39, 125 (1967).
- [49] R. Leapman, L. Grunes, and P. Fejes, Phys. Rev. B, 26, 614 (1981).

B

S

S

.

- [50] R. Kleber, Z. Physik, 264, 301 (1973).
- [51] R. Kleber, Z. Physik, 264, 309 (1973).
- [52] B. Cordts, D. Pease, and L. Azaroff, Phys. Rev. B, 22, 4692 (1979).
- [53] J. Fink, Th. Muller-Heinzerling, B. Scheerer, W. Speier, F. Hellebrecht, J. Fuggell, J. Zaanen, and G. Sawatzky, Phys. Rev. B, 32, 4899 (1985).
- [54] J. Zaanen, A. Sawatzky, J. Fink, W. Speier, and J. Fuggell, Phys. Rev. B, 32, 4905 (1985).
- [55] Herzberg, Atomic Spectra and Atomic Structure, 160 (Prentice-Hall, Inc., New York, 1937).
- [56] L. Pauling, The Nature of the Chemical Bond, 3rd ed., (Cornell Univ. Press, Ithaca, 1960).
- [57] M.P. Das, and N. Nafari, Sol. St. Comm., 58, 29 (1986).
- [58] R. Camley, and D. Mills, Phys. Rev. B, 29, 1695 (1984).
- [59] R. Ritchie, Phys. Rev., 106, 874 (1957).
- [60] P. Jewsbury, J. Phys. F: Met. Phys., 12, 2377 (1982).
- [61] G. Giuliani, J. Quinn, and R. Wallis, J. de Physique, Colloque 45, C5-285 (1984).
- [62] G. Eliasson, G. Giuliani, J. Quinn, and R. Wallis, Phys. Rev. B, 33, 1405 (1986).
- [63] A. Segmuller, and A.E. Blakeslee, J. Appl. Cryst., 6, 19 (1973).

Wa

(1

R

5

w

(

[64] D.B. McWhan, M. Gurvitch, J.M. Rowell, and L.R. Walker, *J. Appl. Phys.*, 54 (7), 3886 (1983).

[65] I.K. Schuller, *Phys. Rev. Lett.*, 44, 1597 (1980).

[66] B. Warren, X-Ray Diffraction, (Addison-Wesley, Reading, Mass., 1969).

[67] C. Kittel, Introduction to Solid State Physics, 5th ed., 58 (John Wiley and Sons, Inc., New York, 1976).

[68] R.W. James, X-Ray Crystallography, 59 (John Wiley and Sons, Inc., New York, 1953).

[69] A. Guinier, X-Ray Diffraction, (W.H. Freeman and Co., San Francisco, 1963).

[70] Introduction to Analytical Electron Microscopy, J. Hren, J. Goldstein, and D. Joy, eds., (Plenum Press, New York, 1979).

[71] G. Thomas, and M. Goringe, Transmission Electron Microscopy of Materials, (John Wiley and Sons, Inc., New York, 1979).

[72] N. Ashcroft, and N. Mermin, Solid State Physics, (Saunders College HRW, Philadelphia, 1976).

[73] E. Shiles, T. Sasaki, M. Inokuti, and D. Smith, *Phys. Rev. B.*, 22, 1612 (1980).

[74] P. Schmuser, *Sol. St. Comm.*, 2, 41 (1964).

[75] L. Davis, and L. Feldkamp, *Sol. St. Comm.*, 19, 413 (1976).

0

5

4

2

1

[76] See the oxidation states of V in, e.g., Handbook of Chemistry and Physics, (CRC Press, Inc., Boca Raton, Florida).

[77] W. Gudat, and C. Kunz, Phys. Stat. Sol. (b), 52, 433 (1972).

[78] G. Rossi, R. Jaeger, J. Stohr, T. Kendelewicz, and I. Lindau, Phys. Rev. B, 27, 5154 (1983), and refs. therein.

[79] F. Lytle, J. Catal., 43, 376 (1976).

[80] D. Pease, and L. Azaroff, J. Appl. Phys., 50, 6605 (1979).

[81] F. Szmulowicz, and D. Pease, Phys. Rev. B, 17, 3341 (1978).

[82] C. Ahn, and O. Krivanek, EELS Atlas, (Gatan, Inc., Warrendale, PA, 1983).

[83] A.V. Crewe, Phil. Trans. R. Soc. Ser. B, 261, 61 (1971).

[84] V.G. Microscope Operating Manual

[85] R.W. Fink, in Proceedings of a Workshop on Energy Dispersive X-Ray Spectrometry, K.F. Heinrich, D.E. Newbury, R.L. Myklebust, and C.E. Fiori, eds., NBS SP604 (Government Printing Office, Washington, 1981).